

分 类 号 _____

学号 _____ D201277241 _____

学校代码 10487

密级 _____

华中科技大学
博士 学位 论文

太阳能光热梯级发电系统建模
及其特性研究

学位申请人： 张成

学科专业： 热能工程

指导教师： 高伟 教授

Inmaculada Arauzo 教授

张燕平 副教授

答辩日期： 2018 年 1 月 20 日

A Thesis Submitted in Partial Fulfillment of the
Requirements for the Ph.D

Cascade solar thermal power system modeling and
research of the key features

Student : Cheng Zhang

Major : Thermal Engineering

Supervisor : Prof. Wei Gao

Prof. Inmaculada Arauzo

Associate Prof. Yanping Zhang

Huazhong University of Science & Technology

Wuhan 430074, P. R. China

January 20, 2018

独创性声明

本人声明所呈交的学位论文是我个人在导师的指导下进行的研究工作及取得的研究成果。尽我所知,除文中已标明引用的内容外,本论文不包含任何其他人或集体已经发表或撰写过的研究成果。对本文的研究做出贡献的个人和集体,均已在文中以明确方式标明。本人完全意识到本声明的法律结果由本人承担。

学位论文作者签名:

日期: 年 月 日

学位论文版权使用授权书

本学位论文作者完全了解学校有关保留、使用学位论文的规定,即:学校有权保留并向国家有关部门或机构送交论文的复印件和电子版,允许论文被查阅和借阅。本人授权华中科技大学可以将本学位论文的全部或部分内容编入有关数据库进行检索,可以采用影印、缩印或扫描等复制手段保存和汇编本学位论文。

本论文属于 保密口,在 ____ 年解密后适用本授权书。
 不保密口。
(请在以上方框内打“√”)

学位论文作者签名:

日期: 年 月 日

指导教师签名:

日期: 年 月 日

摘要

随着化石能源消耗和环境污染问题的凸显,太阳能被广泛认为是未来最有潜力替代传统化石能源的清洁能源。本文以国家国际合作项目专项“太阳能梯级集热发电系统关键技术合作研究”为背景,目标是研究太阳能光热发电装置,利用各种传统型式的太阳能光热发电系统的优缺点以及热力特性,提出并组建、优化太阳能梯级集热发电系统,为探索出大规模低成本高效率利用太阳能的光热发电技术提供新的方案。主要研究内容包括:

提出了多种采用梯级集热和梯级发电的太阳能光热梯级发电系统。在梯级系统中,采用了多种型式的集热器,实现能量的梯级收集,采用多种形式的热力循环,实现能量的梯级利用。经过系统评估、参数选取、初步计算、方案比较,确定了两种具有代表性的梯级系统方案。

采用 EES、MATLAB 等工具,建立了梯级系统中各部件的机理模型,进而组建了梯级系统。采用面向对象的方法,充分利用了继承、多态等特性,保证了各部件之间既具有独立性又具有关联性。其中,斯特林机的建模过程中,考虑了多种不可逆过程及多类损失,建立了较为完善的斯特林机机理模型,并进行了模型验证分析。结果表明,所建立的斯特林机模型的精度要高于传统的经典斯特林机模型。

研究了太阳能光热梯级发电系统中斯特林机组不同排布方式对系统效率的影响。通过分析斯特林机组的各种不同的排布方式,发现串联连接是最佳的连接型式,斯特林机组具有最佳健壮性和最大的发电效率,梯级发电系统也具有最大的光热发电效率。

提出了分阶段加热的方法,有效降低了蒸汽发生系统中的烟损。在传统蒸汽发生系统的换热过程中,加热流体无相变,被加热流体有相变,两者存在较大的换热温差,换热过程有较大的烟损。本文提出分阶段加热的方法,通过改变加热流体的流量,减小换热温差,降低换热过程的烟损。

提出了太阳能光热梯级发电系统与传统型式太阳能光热发电系统的对比方法。本文针对新型梯级发电系统提出了其与传统型式太阳能光热发电独立系统的对比方法。梯级系统在一定的参数条件下,相比其对应的独立系统,具有更高的总体光电转换效率。

建立了太阳能集热发电试验平台,并开展了相关的试验工作。在相关试验条件下,槽式集热器的热效率在 60.1% 到 62.8% 之间,槽式集热器的热效率在 39.7% 到 63.3% 之间。试验还验证了建立的槽式集热器和碟式集热器模型。

关键词： 槽式集热器, 碟式集热器, 朗肯循环, 斯特林循环, 斯特林机组, 梯级发电

Abstract

With the increasing awareness of the problem of fossil energy consumption and environmental pollution, solar energy is regarded as the best potential alternative of fossil energy. This research is based on the national cooperation project “Collaborative research on key technologies to produce electricity by cascade utilization solar thermal energy”. The objective of this project is to conduct research on the equipment of solar thermal power generation system, to propose, develop and optimize a solar thermal cascade system depending on the advantages and disadvantages of the solar thermal power generation technologies, and to explore a new feasible technology for large-scale solar thermal power generation. The main contents and conclusions of this thesis are as follows:

Multiple topological structures with cascade collection and cascade utilization of the cascade systems were proposed. In these systems, different types of collectors were used for cascade collection and different types of thermodynamic cycles were used for cascade utilization. After system evaluation, parameter selection, preliminary calculation and scheme comparison, two representative typical schemes were selected.

Mechanism models were established for the components of solar thermal power generation system by using EES and MATLAB. The modeling process uses an object-oriented approach, taking full advantage of inheritance, polymorphism and other characteristics, to ensure each component has both independence and relevance. Among them, the Stirling machine modeling process, considering various irreversibilities and losses, established a more accurate Stirling mechanism model with verification analysis. The results show that the accuracy of the established Stirling model is higher than that of the classical classical Stirling engine models.

The effect of different arrangements of Stirling engines on the efficiency of the cascade system was studied. Through the analysis of different arrangements of Stirling engines, it was found that series connection is the best connection type for the best robustness and maximum efficiency of the Stirling engines, and the largest solar-to-electric efficiency of the cascade system.

A method of multistage heating was proposed, which can effectively reduce the exergy loss of steam generating system. During the entire heat exchange process of a conventional steam generating system, there is no phase change in the heating fluid and there is a phase

change in the heated fluid. There exist large heat transfer temperature differences between the two fluids in the heat exchangers, which makes large entropy production during the heat exchange process. In this thesis, a method of heating in stages is proposed, in which the flow rates of the heating fluid in different heat exchangers are controlled to reduce the heat transfer temperature difference and the exergy losses.

A comparison method of cascade system and traditional solar thermal power generation systems is proposed. In this thesis, corresponding independent systems of the cascade system was proposed for comparison. It is found that the cascade system has a higher overall solar-to-electric conversion efficiency under certain parameters compared to its corresponding independent systems.

A solar thermal power generation test platform was established, and the relevant experimental work was carried out. Under the relevant test conditions, the thermal efficiency of trough collectors is between 60.1% and 62.8%, and that of dish collectors is between 39.7% and 63.3%. The experiment also validated the established trough collector and dish collector models.

Key words: parabolic trough collector, parabolic dish collector, Rankine cycle, Stirling cycle, Stirling engine array, cascade solar thermal power

目 录

摘要	I
插图索引	XII
表格索引	XV
1 绪论	1
1.1 研究背景及意义	1
1.2 研究现状	3
1.3 Literature summary	18
1.4 Research content	18
2 系统拓扑结构	20
2.1 系统拓扑结构的设计	20
2.2 系统拓扑结构的选择	28
2.3 选定的梯级系统拓扑结构	34
2.4 本章小结	36
3 Modeling	37
3.1 Component modeling	37
3.2 Stirling engine array modeling	59
3.3 Steam generating system modeling	61
3.4 System modeling	63
3.5 Conclusion	65
4 Optimization of Stirling engine array	66
4.1 Connection types of SEA	66
4.2 Modeling of the SEAs	67
4.3 Result analysis	69
4.4 Conclusion	77

5 Optimization of steam generating system	78
5.1 Steam generating subsystem	78
5.2 Multistage exergy loss reduction system	80
5.3 Comparison	83
5.4 Conclusion	86
6 Cascade system performance evaluation	87
6.1 System description	87
6.2 System evaluation method	89
6.3 System parameters	91
6.4 Stand-alone system selection	93
6.5 Comparison with stand-alone system	95
6.6 Conclusion	100
7 Experiment research on solar thermal power platform	102
7.1 Platform introduction	102
7.2 Experiments	108
7.3 Result analysis	112
7.4 Conclusion	121
8 Summaries and outlooks	122
8.1 Summaries	122
8.2 Innovations	125
8.3 Outlooks	126
致谢	127
参考文献	129
附录 A Heat transfer under constant temperature	137
附录 B Thermal gradient under constant heat flux	139
附录 C MATLAB code of class Stream	141
附录 D 攻读学位期间发表的学术论文	143

Nomenclature

\dot{m}	Mass flow rate, $\text{kg}\cdot\text{s}^{-1}$
$\overline{d_{cav}}$	Effective diameter of the cavity, m
A	Heat transfer area, m^2
$A_{dr,1}$	Heat transfer area of dish receiver between tube and air, m^2
$A_{se,1}$	Heat transfer area of Stirling engine at air side, m^2
$A_{se,2}$	Heat transfer area of Stirling engine at water side, m^2
c_p	Specific heat at constant pressure, $\text{J}\cdot\text{kg}^{-1}\cdot\text{K}^{-1}$
c_r	Heat transfer correction factor of coiled tube of volumetric receiver
c_v	Specific heat at constant volume, $\text{J}\cdot\text{kg}^{-1}\cdot\text{K}^{-1}$
d	Diameter, m
d_i	Inner diameter of trough receiver, m
dep	Depth, m
e	Regenerator effectiveness
f	Focal length, m
J	Annular gap cylinder displacer, m
K	Dead volume factor
k	Specific heat ratio (c_p/c_v), thermal conductivity, $\text{W}\cdot\text{m}^{-1}\cdot\text{K}^{-1}$
m	Mass of working fluid in Stirling engine, kg
n	Number of collectors

n_1	Number of columns of the Stirling engine array
n_2	Number of rows of the Stirling engine array
n_g	Amount of working gas in each Stirling engine, mol
n_{se}	Number of Stirling engines in the Stirling engine array
Nu	Nusselt number
P	Power of Stirling engine, W
p	Pressure, Pa
p_e	Extraction pressure of the steam turbine, Pa
Pr	Prandtl number
Q	Absorbed heat, J
q''	Heat flux, $\text{W}\cdot\text{m}^{-2}$
R	Gas constant, $\text{J}\cdot\text{kg}^{-1}\cdot\text{K}^{-1}$
Re	Reynolds number
s_{se}	Speed of Stirling engine, Hz
T_H	Working fluid temperature in the hot space, K
T_L	Working fluid temperature in the cold space, K
T_R	Effective working fluid temperature in regenerator, K
T_w	Wall temperature, K
U	Overall heat transfer coefficient, $\text{W}\cdot\text{m}^{-2}\cdot\text{K}^{-1}$
V_C	Compression volume, m^3
V_D	Total dead volume, m^3
V_E	Expansion volume, m^3

V_{DC} Cold space dead volume, m³

V_{DH} Hot space dead volume, m³

V_{DR} Regenerator dead volume, m³

W Output work, J

x Dryness fraction

y Extraction rate of steam turbine

Z Displacer stroke, m

Abbreviations

ANN Artificial neural network

CCHP Combined cooling, heating and power

CFD Computational fluid dynamics

CPC Compound parabolic collector

CRTEn Research and technologies centre of energy in Borj Cedria

CSP 太阳能聚光集热发电

DSG Direct Steam Generation

HTF Heat Transfer Fluid

ISCC Integrated Solar Combined Cycle

LFC Linear Fresnel Collector

LM Levenberge Marguardt

LSSVM Least squares support vector machine

MCRT Monte Carlo Ray Tracing

ORC Organic Rankine Cycle

PCG Pola-Ribiere Conjugate Gradient

PTC Parabolic Trough Collector

SCG Scaled Conjugate Gradient

SNL Sandia National Laboratory

SRC Steam Rankine Cycle

Greek Symbols

β Ratio of power of Stirling engines to the total output power of cascade system

δ Thickness, m

ϵ Emissivity

η_{diff} Efficiency difference of cascade system and stand-alone systems, $\eta_{cs} - \eta_s$

$\eta_{shading}$ Shading factor

γ Intercept factor; compression ratio

γ_H Space ratio in process 12

γ_L Space ratio in process 34

λ Thermal conductivity, $\text{W}\cdot\text{m}^{-1}\cdot\text{K}^{-1}$

μ Viscosity, $\text{kg}\cdot\text{m}^{-1}\cdot\text{s}^{-1}$

ρ Reflectivity

θ_{dc} Dish aperture angle (0° is horizontal, 90° is vertically down)

Subscripts

c Cooling fluid; counterflow

cd Condenser

cs Cascade system

<i>cw</i>	Cooler wall
<i>g</i>	General solution
<i>h</i>	Heating fluid; homogeneous solution
<i>hw</i>	Heater wall
<i>i</i>	Inlet
<i>insu</i>	Insulating layer
<i>o</i>	Outlet
<i>p</i>	Parallel flow; particular solution; piston
<i>pu</i>	Pump
<i>r</i>	Regenerator
<i>s</i>	Stand-alone systems
<i>se</i>	Stirling engine
<i>sea</i>	Stirling engine array
<i>th</i>	Theoretical
<i>w</i>	Tube wall
<i>x</i>	Stirling engine in column <i>x</i>
<i>rk</i>	Rankine cycle

插图索引

图 1-1	三种 CSP 技术的应用实例	2
图 1-2	The SG3 400 m ² dish in Australian National University	8
图 1-3	Two-stage receiver system	13
图 1-4	Simplified schematic of a proposed integrated CSP plant configuration	14
图 1-5	The proposed ISCC scheme	15
图 1-6	Schematic of the proposed ISCC with two bottoming cycles	16
图 2-1	太阳能槽式发电系统和太阳能碟式发电系统结构示意图	20
图 2-2	太阳能光热发电系统中的元件列表	21
图 2-3	用于朗肯循环的理想工质的温熵图	22
图 2-4	典型的水工质和有机工质的朗肯循环的太阳能光热系统结构示意图	23
图 2-5	太阳能烟囱电站的结构示意图	24
图 2-6	槽式系统和太阳能烟囱组合结构示意图	25
图 2-7	一种采用集热器串联连接的梯级系统	25
图 2-8	典型的 DSG 太阳能系统示意图	26
图 2-9	使用空气-导热油换热器的太阳能光热系统示意图	27
图 2-10	两种使用了空气-水换热器的梯级系统实例	27
图 2-11	典型热机的热功转换图	28
图 2-12	太阳能光热应用中所使用的三种热力循环的 T-s 图	29
图 2-13	不同运行温度下的效率曲线	29
图 2-14	采用多种型式集热器串联连接的太阳能塔式发电系统	31
图 2-15	使用空气-导热油换热器的太阳能光热系统示意图	33
图 2-16	两种使用了空气-水换热器的梯级系统实例	33
图 2-17	采用多个热力循环之间热量回收利用的梯级系统结构图	34
图 2-18	两种选定的梯级系统拓扑结构图	35
图 2-19	图 2-18b 的一个计算案例	36
图 3-1	Some of the optical parameters of a parabolic trough	39

图 3-2	Schematic diagram of the absorber pipe	39
图 3-3	The structure of the dish receiver	41
图 3-4	Thermal network of dish receiver	42
图 3-5	$T-s$ diagram of a Stirling cycle	46
图 3-6	$T-s$ diagram of the water circuit and $h-s$ diagram of the process 2a-2b	55
图 3-7	$T-s$ diagram of water and a typical organic fluid in Rankine cycles . .	58
图 3-8	The schematic diagram of an ORC system with regenerator	58
图 3-9	Layout of Stirling engines	59
图 3-10	Heat transfer diagrams of parallel flow and counterflow	60
图 3-11	An example of steam generating system in a cascade system	62
图 3-12	The steam generating process	63
图 4-1	Five basic connection types of SEA	67
图 4-2	An instance of connection type of an SEA	68
图 4-3	Flowcharts of the SEA model for performance analysis of the SEAs .	70
图 4-4	Influence of $T_{i,h}$ on efficiency and power of SEA	72
图 4-5	Influence of $\dot{m}_h c_{p,h}$ on efficiency and power of SEA	73
图 4-6	Influence of $\dot{m}_c c_{p,c}$ on efficiency and power of SEA	74
图 4-7	Influence of n_{se} on efficiency and power of SEA	76
图 5-1	A typical solar parabolic trough system	78
图 5-2	The steam generating process in counterflow heat exchangers	79
图 5-3	The tradeoff to choose \dot{m}_3	80
图 5-4	Change \dot{m}_3 in the heat exchangers to reduce the temperature difference	81
图 5-5	The schematic diagram of the MELRS	81
图 5-6	T_{3b} in the $T-Q$ diagram of the heat transfer processes	85
图 6-1	Sketch of the cascade system	88
图 6-2	Diagrams of water circuit and 2e-2f process	89
图 6-3	Sketch of the stand-alone systems	94
图 6-4	Curve fits of efficiency difference η_{diff} versus I_r	97
图 6-5	Curve fits of efficiency difference η_{diff} versus β	97
图 6-6	Parallel flow: Temperature series of two fluids and efficiency of Stir- ling engines in column x	99

图 6-7	Counterflow: Temperature series of two fluids and efficiency of Stirling engines in column x	99
图 6-8	Efficiency of Stirling engine array with different $q_{2,m}$	100
图 7-1	Schematic structure of the platform	103
图 7-2	Trough collector of the platform	105
图 7-3	Dish collector of the platform	106
图 7-4	ORC system of the platform	107
图 7-5	Control screen of the ORC system	107
图 7-6	Influence of solar irradiance on the thermal efficiency	114
图 7-7	Influence of inlet flow rate on the thermal efficiency	115
图 7-8	Influence of inlet temperature on the thermal efficiency	116
图 7-9	Influence of solar irradiance on the thermal efficiency	118
图 7-10	Simulation results of influence of solar irradiance on the thermal efficiency	118
图 7-11	Influence of inlet flow rate on the thermal efficiency	119
图 7-12	Influence of inlet temperature on the thermal efficiency	120
图 1-1	Diagram of heat transfer under constant temperature	137
图 2-1	Diagram of heat transfer with one constant temperature heat source and constant heat flux	139

表格索引

表 2.1	对应温度下的饱和蒸气的压力和密度	23
表 2.2	太阳能烟囱设计参数及模拟结果	30
表 3.1	Key parameters of the dish collector	42
表 3.2	Design specifications of the GPU-3 Stirling engine ^[1,2]	50
表 3.3	Thermal efficiency of the models and experimental data (at $T_{hw} = 922\text{ K}$ and $T_{cw} = 288\text{ K}$)	51
表 3.4	Output power of the models and experimental data (at $T_{hw} = 922\text{ K}$ and $T_{cw} = 288\text{ K}$)	52
表 4.1	Parameters of SEA models	69
表 4.2	Results of SEA models under specified parameters	71
表 5.1	Main parameters used for SGSS and MELRS	83
表 5.2	Simulation results of SGSS and MELRS	84
表 6.1	Main parameters of LS-3	92
表 6.2	Basic design parameters of the cascade system	93
表 6.3	Some important results using design parameters	96
表 6.4	Results of Stirling engine array with two different flow types	98
表 7.1	Key parameters of the designed dish collector	104
表 7.2	Designed cases of the solar trough system	109
表 7.3	Designed cases of the solar dish system	112
表 7.4	Experiment results of Case 1 to Case 10 of the trough collector	113
表 7.5	Experiment results of Case 11 to Case 15 of the trough collector	114
表 7.6	Experiment results of Case 16 to Case 20 of the trough collector	115
表 7.7	Experiment results of Case 1 to Case 10 of the dish collector	117
表 7.8	Experiment results of Case 11 to Case 15 of the dish collector	119
表 7.9	Experiment results of Case 16 to Case 20 of the dish collector	120

— 绪论

1.1 研究背景及意义

可再生能源在世界范围内已经成为主流能源。可再生能源,尤其是清洁电力的快速发展,受到诸多因素的推动,包括可再生能源技术成本的降低,政府专项政策的推动,融资渠道更加完善,能源安全和环境问题,发展中国家和新兴经济体对能源需求的不断增长,以及获得现代能源的需求。

太阳能因具有分布广泛,能量巨大,取之不竭,安全环保等优点,受到很多国家的关注,被认为是化石能源的最佳潜在替代者。国际能源机构预计,到 2050 年“大量应用可再生能源”的情景下,太阳能光伏发电量和太阳能光热发电量将分别占全球总用电量的 16% 和 11%,太阳能将成为全球最大的电力来源^[3]。

太阳能光热发电是除太阳能光伏发电之外的另一种太阳能发电技术。由于太阳能能量密度较低,为了提高可用的能量密度,太阳能光热发电通常采用聚光集热发电(CSP)的形式,使用反射镜将太阳光会聚到用于吸收太阳能的接收器上,产生热量并将其传递给合成油,熔融盐或空气等传热流体。然后,传热流体直接或间接地为动力循环系统提供热源。与太阳能光伏发电相比,太阳能集热发电因其能量密度高,发电平稳,电网兼容性好,易于与现有火力发电厂集成等优点受到越来越多的关注。

太阳能光热发电技术使用不同种类的反射镜将太阳的光能会聚到接收器上并将其转换成热量。现有三种已商业应用的 CSP 技术:太阳能槽式发电,太阳能碟式发电和太阳能塔式发电。这三种集热发电技术因其各自的反射镜类型而得名。图1-1展示了这三种 CSP 技术的应用实例。

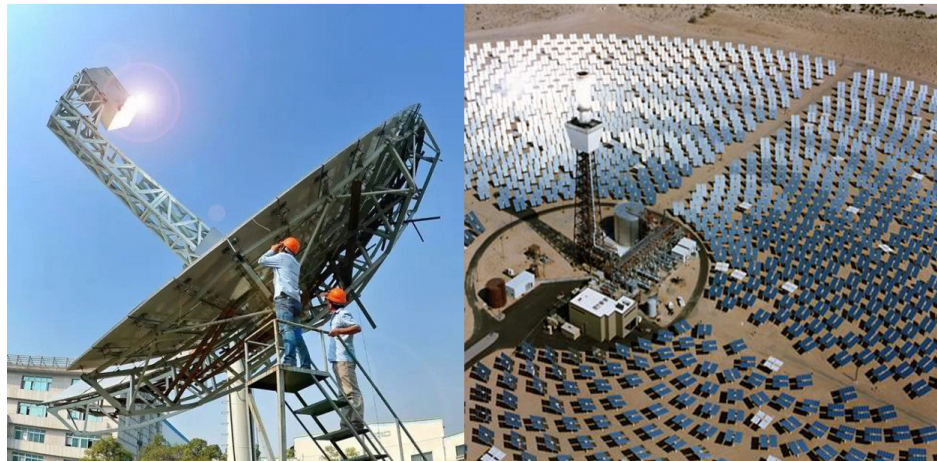
太阳能槽式发电的反射镜是槽型抛物面。反射镜在白天采用单轴跟踪的形式跟踪太阳。反射镜将太阳光反射聚集到位于焦线处的集热管上。传热流体(例如合成油)流经集热管并吸收由聚集的太阳光产生的热量,然后为发电系统提供热量。

太阳能碟式发电的反射镜是旋转抛物面,它可以将沿着轴线照射的太阳光会聚到焦点上。碟式集热发电采用双轴跟踪系统来保证反射镜始终直接朝向太阳从而避免了余弦损失。它可以获得很高的聚光比,并因此获得高温热源。通常情况下,焦点处放置有接收器或斯特林发动机来吸收会聚到的能量。

太阳能塔式发电是一种使用位于高塔顶部的接收器来接收聚焦阳光的太阳能发电形式。它使用大量可移动的太阳能反射镜(称为定日镜)。每台定日镜都各自配有跟



太阳能槽式发电



太阳能碟式发电

太阳能塔式发电

图 1-1 三种 CSP 技术的应用实例

踪机构将太阳光实时准确地反射到位于塔顶的接收器上。该跟踪机构为双轴跟踪(从东向西,向上和向下)跟踪太阳。接收器吸收集中的太阳辐射并将太阳能转换成热量,并将热量传递给传热流体,传热流体将热量传递至热力循环系统用于发电。

在三种太阳能光热发电技术中,太阳能槽式发电是最成熟和最具商业化的技术。但是,它的聚光比较低,接收器的温度比较低,光热发电效率也比较低。太阳能碟式发电的聚光比达数百甚至数千,因此可以获得很高温度的热能,其光热发电效率高于太阳能槽式发电。此外,太阳能碟式发电的一个优点是它的发电过程用水量非常少。然而,太阳能碟式发电并未实现大规模应用,其结构紧凑,安装方便,主要应用于分布式发电。当使用大量的定日镜时,太阳能塔式发电的塔顶会聚了大量的能量,接收器的

温度可以达到非常高,而且太阳能塔式发电也可以实现大规模应用。但与此同时,它也具有投资高,系统复杂度高的缺点。太阳能塔式发电目前处于快速发展阶段。

不同种类的太阳能光热发电技术具有各自的优缺点,找到一种能够利用现有太阳能光热发电技术的优势并克服其缺点的方法是非常重要的。换句话说,开发出一种效率更高,成本更低的新的太阳能光热发电技术是迫在眉睫的。本文试图通过提出使用不同型式的太阳能集热器和不同种类的热力循环的梯级系统来实现这一目标。这可能是实现大规模,高效率和低成本太阳能光热发电的新的可行技术。

1.2 研究现状

1.2.1 太阳能槽式发电

抛物槽太阳能技术是目前最成熟和成本最低的大规模太阳能发电技术^[4]。许多研究人员已经做了大量的工作来研究太阳能槽式发电,以提高性能或降低成本。其中很多研究着重于旨在测试抛物槽收集器的热性能和机械性能的实验性工作。

来自桑迪亚国家实验室的 Dudley 等人^[5] 测试了应用于 SEGS 太阳能光热电站的 LS-2 型槽式接收器的集热效率和热损失。试验分析了不同类型的选择性涂层,不同接收器配置,不同真空度对集热器性能的影响。他们还建立了槽式接收器的一维分析模型,并将模拟结果与试验数据进行了对比分析。来自美国国家可再生能源实验室的 Burkholder 和 Kutscher^[6] 测试了来自 Solel 的 UVAC3 型槽式集热器和来自 Schott 的 PTR70 型槽式集热器,并建立了以接收器平均温度和环境温度为参数的热损失方程。Reddy 等人开发并研究了六种不同型式的槽式集热器,并进行了性能对比分析。根据 ASHRAE 93-1986 测试程序,对一台 15 美元的收集器进行了实验测试。

It is well known that experimental studies are the most accurate and convincing method for parabolic trough collector research. However, this method is not only investment required and also time consuming. In order to reduce the R&D cost and time, parabolic trough collectors are usually modeled.

Some researchers investigated the optical model of the parabolic trough solar collectors. Wang et al.^[9] proposed a mathematical model for optical efficiency of the trough collector and selected three typical regions of solar thermal utilization in China for the model. The model is validated by comparing the test results in parabolic trough power plant, with relative error range of 1% to about 5%. Zou et al.^[10] investigated the influences of sunshape and incident angle on the optical performance of the trough collectors. It is found that the sunshape

has significant effect on the optical efficiency and should be taken into consideration in practice. Larger aperture with smaller absorber diameter leads to more end loss caused by incident angle. It is also found that optimal focal length exists for the optical efficiency. Lüpfert et al.^[11] introduced the specific techniques to analyze the geometry and optical properties of trough collectors and summarized results in collector shape measurement, flux measurement, ray tracing, and thermal performance analysis for parabolic troughs. It is shown that the measurement methods and the parameter analysis give consistent results, which can provide references for the next generation trough collector relevant improvements. Xu et al.^[12] analyzed the optical efficiency of a PTC with horizontal north-south axis and proposed a method to compensate the end loss effect of the PTC. The calculation formula of the optical end loss rate and the increased optical efficiency for the system using the compensation method were derived. A five-meter experimental system was built to verify the feasibility of the compensation method proposed. The increased thermal efficiency of the experimental system was measured, and it was proved that the proposed compensation method is feasible. Huang et al.^[13] proposed an analytical model for optical performance which employed a modified integration algorithm to simulate the performance of trough collectors. The analytical equation of the optical efficiency of each point of the reflector was deduced to obtain the optical efficiency of the system by integration algorithm.

Some researchers investigated the exergy performance of the parabolic trough collectors. Padilla et al.^[14] performed a comprehensive exergy balance of a parabolic trough collector based on the previous heat transfer model^[15]. The results show that inlet temperature of heat transfer fluid, solar irradiance, and vacuum in annulus have a significant effect on the thermal and exergetic performance, but the effect of wind speed and mass flow rate of heat transfer fluid is negligible. It was obtained that inlet temperature of heat transfer fluid cannot be optimized to achieve simultaneously maximum thermal and exergetic efficiency because they exhibit opposite trends. Finally, it was found that the highest exergy destruction is due to the heat transfer between the sun and the absorber while for exergy losses is due to optical error. Guo et al.^[16] investigated the energy efficiency and exergy efficiency of the parabolic trough collector. The result shows that there exists an optimal mass flow rate of working fluid for exergy efficiency, and the thermal efficiency and exergy efficiency have opposite changing tendencies under some conditions.

Some researchers are dedicated to developing more accurate models using new meth-

ods. Behar et al.^[17] developed and validated a novel parabolic trough solar collector model. The model has been compared with models made by Lab. SNL and NREL. The proposed model has a better accuracy of thermal performance prediction. Padilla et al.^[15] performed a detailed one dimensional numerical heat transfer analysis of a PTC (Parabolic Trough Collector). To solve the mathematical model of heat transfer of the PTC model, the partial differential equations were discretized and the nonlinear algebraic equations were solved simultaneously. The numerical results was validated to the data from Sandia National Laboratory (SNL). Hachicha et al.^[18] presented a detailed numerical heat transfer model based on the finite volume method for the parabolic trough collector. This model is based on finite volume method and ray trace techniques and takes into account the size of the Sun. The model is thoroughly validated with results from the literature and it shows a good agreement with experimental and analytical results. Guo and Huai^[19] implemented a multi-parameter optimization of parabolic trough solar receiver based on genetic algorithm where Exergy and thermal efficiencies were employed as objective function. Boukelia et al.^[20] investigated the feed-forward back-propagation learning algorithm with three different variants; Levenberge Marguardt (LM), Scaled Conjugate Gradient (SCG), and Pola-Ribiere Conjugate Gradient (PCG), used in artificial neural network (ANN) to find the best approach for prediction and techno-economic optimization of parabolic trough solar thermal power plant integrated with fuel backup system and thermal energy storage. Liu et al.^[21] developed a mathematical model of PTC using the least squares support vector machine (LSSVM) method. Numerical simulations were implemented to evaluate the feasibility and efficiency of the LSSVM method, where the sample data derived from the experiment and the simulation results of two solar collector systems with 30 m² and 600 m² solar fields, and the complicated relationship between the solar collector efficiency and the solar flux, the flow rate and the inlet temperature of the heat transfer fluid (HTF) is extracted. Lobon et al.^[22] introduced a computational fluid dynamic simulation approach to predict the behavior of a solar steam generating system, which is located at the Plataforma Solar de Almeria, Spain. The CFD package STAR-CCM+ code has been used to implement an efficient multiphase model capable of simulating the dynamics of the multiphase fluid in parabolic-trough solar collectors. Numerical and experimental data are compared in a wide range of working conditions. To understand the thermal performance of the collector and identify the heat losses, Mohamad et al.^[23] analyzed the temperature variation of the working fluid, tube and glass along the

collector. It is found that using double glazing cover enhances the thermal efficiency of the collector operating at high temperature. However, when the collector length is 10 m or less, it is more economical to use a single glass cover for the collector than a double glazing cover. Also, it is clearly shown that increasing the diameter of absorbing tube enhances the rate of heat transfer losses, consequently decreasing the thermal efficiency of the collector. Guo et al.^[24] developed a nonlinear distribution parameter model to model the dynamic behaviors of direct steam generation parabolic trough collector loops under either full or partial solar irradiance disturbance.

Some researchers have proposed some new types of solar trough systems. Ashouri et al.^[25] coupled a small scale parabolic trough collector and a thermal storage tank along with an auxiliary heater to a Kalina cycle to study the performance of the system throughout the year, both thermodynamically and economically. Bader et al.^[26] developed a numerical model of a tubular cavity-receiver that uses air as the heat transfer fluid. Four different receiver configurations are considered, with smooth or V-corrugated absorber tube and single- or double-glazed aperture window. The different types of energy loss by the collector have been quantified, and the temperature distribution inside the receiver has been studied. The pumping power required to pump the HTF through the receiver has been determined for a 200 m long collector row. Good et al.^[27] proposed solar trough concentrators using air as heat transfer fluid at operating temperatures exceeding 600°C. It consists of an array of helically coiled absorber tubes contained side-by-side within an insulated groove having a rectangular windowed opening. Secondary concentrating optics are incorporated to boost the geometric concentration ratio to 97×. Kaloudis et al.^[28] investigated a PTC system with nanofluid as the HTF in terms of Computational Fluid Dynamics (CFD). Syltherm 800 liquid oil was used as the HTF, and Al₂O₃ nanoparticles with the concentrations ranges from 0% to 4% was investigated. A boost up to 10% on the collector efficiency was reported for Al₂O₃ concentration of 4%. Al-Sulaiman et al.^[29] proposed a novel system based on PTC and ORC for combined cooling, heating and power (CCHP). Performance assessment, including efficiency, net electrical power, and electrical to heating and cooling ratios, of the system shown that when CCHP is used, the efficiency increases significantly. This study reveals that the maximum electrical efficiency for the solar mode is 15%, for the solar and storage mode is 7%, and for the storage mode is 6.5%. The maximum CCHP efficiency for the solar mode is 94%, for the solar and storage mode is 47%, and for the storage mode is 42%.

1.2.2 Parabolic dish

The solar parabolic dish system is known for its highest efficiency of all solar technologies (around 30%). It is suitable for distributed power generation for its compact structure and easy installation.

Many researchers conducted experiments to investigate the solar parabolic dish system or to validate proposed models. To investigate the heat loss of semi-spherical cavity receiver applied for solar parabolic dish system, Tan et al.^[30] conducted experiments with different fluid inlet temperatures, receiver inclination angles and aperture sizes. Correlations of Nusselt number as a function of Grashof number were developed by the experiment results. Chaudhary et al.^[31] investigated a solar cooker based on dish collector with phase change thermal (PCM) storage unit. Three cases have been considered for the investigation: ordinary solar cooker, solar cooker with outer surface painted black, and solar cooker with outer surface painted black along with glazing. It was observed that the last case shows the best performance, which can store 32.3% and 26.8% more heat for the PCM compared with the first and second cases respectively. Mawire and Taole^[32] investigated the thermal performance of a cylindrical cavity receiver for an SK-14 parabolic dish concentrator. The receiver exergy rates and efficiencies are found to be appreciably smaller than the receiver energy rates and efficiencies. The exergy factor is found to be high under conditions of high solar radiation and high operating temperatures. An optical efficiency of around 52% for parabolic dish system is determined under high solar radiation conditions. Zhu et al.^[33] conducted an experimental investigation of a coil type solar dish receiver. The solar irradiance is about 650 W/m², while the concentrated solar flux at the aperture is approximately 1000 kW/m². The energy and exergy performance of the receiver was analyzed and the experimental results show that, at steady state, the energy efficiency is maintained around 80%, and the exergy efficiency is around 28%. CRTEn developed a solar dish system using four types of absorbers: flat plat, disk, water calorimeter and solar heat exchanger.^[34] For the different types of absorbers, experiments were conducted to obtain the mean concentration ratio and both energy and exergy efficiency. Results shown that thermal energy efficiency of the system varies from 40% to 77%, the concentrating system reaches an average exergy efficiency of 50% and a concentration factor around 178. Thirunavukkarasu et al.^[35] carried out an experimental study to investigate the thermal performance of a cavity receiver for a dish concentrator. The overall system efficiency of the solar collector is 69.47%. The average exergy

efficiency of the receiver is found to be 5.88% with a peak value of 10.35%. Pavlovic et al.^[36] performed the experimental study of a solar dish system. In this system, different working fluids (water, thermal oil and air) were used to validate the numerical models developed in EES (Engineering Equation Solver). It was found that water is the most appropriate working fluid for low-temperature applications, while thermal oil is the most appropriate working fluid for higher-temperature applications.

Some researchers focused on the dish concentrator, many proposed different shapes of concentrators. The perfect concentrator has a parabolic shape, but for some considerations (better production, safer transportation, less cost and so on), some solar concentrators are composed of multiple spherically shaped mirrors. A large dish solar concentrator, SG3, which is about 400 m^2 , was designed and demonstrated in Australian National University in 1994 as shown in Figure 1-2.^[37] It successfully proved the technical viability of a concentrator that is approximately three times bigger than any other produced. Berumen et al.^[38]

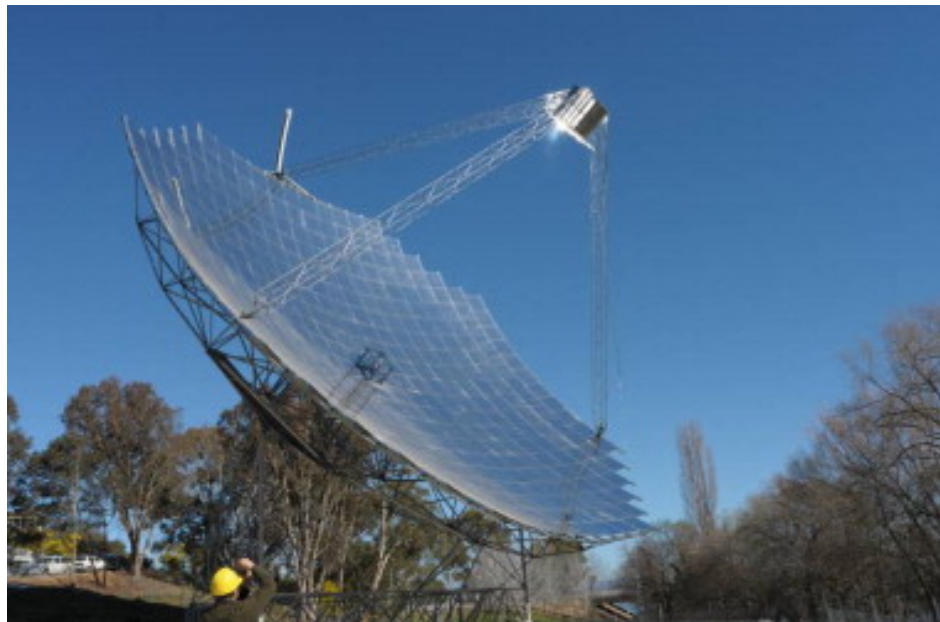


图 1-2 The SG3 400 m² dish in Australian National University

developed a reflector consists of 12 facets made of fiberglass with a reflecting surface made of aluminum sheet with reflectance of 86%. Pavlovic et al.^[39] presented a procedure to design a square facet concentrator for laboratory-scale research on medium-temperature thermal processes. A parabolic collector made up of individual square mirror panels (facets) were

investigated. These facets can deliver up to 13.604 kW radiative power over a 250 mm radius dish receiver with average concentrating ratio exceeding 1200. Hijazi et al.^[40] designed a low cost parabolic solar dish concentrator with small-to moderate size for direct electricity generation and special attention is given to the selection of the appropriate dimensions of the reflecting surfaces. Ma et al.^[41] designed a solar dish concentrator based on triangular membrane facets. A 600-facet concentrator with focal-diameter ratio of 1.1 will achieve 83.63% of radiative collection efficiency over a 15 cm radius disk located in the focal plane, with a mean solar concentration ratio exceeding 300. A 3.6-meter diameter stretched-membrane optical facet for a parabolic dish has been successfully designed and demonstrated under contract with Sandia National Laboratories.^[42] Twelve facets identical to them will be used to make the lightweight reflector of the dish. The project goal of 2.5 mrad surface accuracy was met with each of the two full-sized prototypes, and accuracies of as low as 1.1 mrad were achieved.

Many researches investigated the flux distribution and thermal performance of the solar dish receiver. Shuai et al.^[43] developed a flux distribution measurement system for dish concentrators. A charge coupled device camera was applied to obtain the contours of the flux distribution for target placements with different location. Further, the measured flux distributions are compared with a Monte Carlo-predicted distribution. The results can be a valuable reference for the design and assemblage of the solar collector system. Mao et al.^[44] simulated the flux distribution of a dish receiver using MCRT method. The impacts of incident solar irradiation, aspect ratio (the ratio of the receiver height to the receiver diameter), and system error on the radiation flux of the receiver are investigated. Li et al.^[45] used the Monte-Carlo ray-tracing method for the radiation flux distribution of the solar dish receiver system. The result was validated by experiment and used as the boundary conditions of a CFD receiver model. The fluid flow and conjugate heat transfer in the receiver was numerically simulated and validated by experiments. Wang and Laumert^[46] used the ray-tracing methodology to investigate the effects of cavity surface materials on the flux distribution for an impinging receiver. Five cavity surface materials and their combinations have been studied. The results show that the flux distribution and the total optical efficiency are much more sensitive to the absorptivity on the cylindrical surface than on the bottom. Blazquez et al.^[47] studied the optimization of the concentrator and receiver cavity geometry of parabolic dish system. Ray-tracing analysis has been performed with the open source software Tonatiuh, a

ray-tracing tool specifically oriented to the modeling of solar concentrators. Reddy et al.^[7,48] performed the theoretical thermal performance analysis of a fuzzy focal solar parabolic dish concentrator with modified cavity receiver. Total heat loss from the modified cavity receiver was estimated considering the effects of wind conditions, operating temperature, emissivity of cavity cover and thickness of insulation. Time constant test was carried out to determine the influence of sudden change in solar radiation at steady state conditions. The daily performance tests were conducted for different flow rates. Vikram and Reddy^[49] used a three-dimensional numerical model to investigate the total heat losses of three modified cavity with three configurations for parabolic dish receiver. The effects of cavity diameter ratio, tilt angle, operating temperature, insulation thickness and emissivity on the heat loss of the modified cavity receiver were studied. Based on artificial neural network (ANN) modeling, an improved Nusselt number correlation was proposed for convection, radiation and total heat loss calculation.

Some researchers focused on the solar tracking system. Patil et al.^[50] described the development of automatic dual axis solar tracking system for solar parabolic dish. Five light dependent resistors were used to sense the sunlight and two permanent magnet DC motors are used to move the solar dish. A controller software were developed to control the motors using the data sensed by the resistors. Raturi et al.^[51] proposed a solar tracking system based on gravity which does not require any external source of power. The prototype test results and analysis show that the system can run successfully. Kuang and Zhang^[52] developed new design and implementation of tracking system to improve tracking accuracy for dish solar based on embedded system that mixes active and passive tracking. Jin et al.^[53] described a two-axis sun tracking system with PLC (programmable logic controller) controlled and a combinative tracking method combined active and passive tracking methods for higher accuracy. Shanmugam and Christraj^[54] presented a method of intermittent tracking of the sun in the north-south direction with no tracking in the east-west direction for less energy yield and the frequency of tracking in the north-south direction determined by variations in solar altitude angle and size of the absorber in paraboloidal dish concentrator.

1.2.3 Power tower

Solar power tower technology is gaining more and more interest for its large scale, high concentration ratio and high operating temperature. It is widely regarded as the most promis-

ing solar thermal power technology.

Advances in the power tower technology are mainly the component update as well as system improvement. Some researchers focused on the choice of HTF that used in the power tower. One already standardized commercial plant cycle is the solar tower with conventional steam cycle.^[55] Steam is used as both HTF and working fluid in the Rankine cycle. Steam is directly generated in the receiver and flows into the steam turbine for power generation.^[56–60] Many researchers concerned about using other fluids (molten salt, air) as HTF. Toto et al.^[61] proposed an idea of a hybrid power tower using air as the working fluid of a topping Brayton cycle and HTF of a bottoming Rankine cycle. Rold^[62] proposed an idea of using supercritical CO₂ as HTF. A simplified CFD model has been built to analyze the feasibility of supercritical CO₂ as HTF in solar towers. It was found that it is a promising alternative for both better operating conditions and lower maintenance cost. Joshi et al.^[63] used the dynamic simulation technology to evaluate a molten salt central receiver design and control strategies.

Many researchers concerned about the heliostats to reach high tracking accuracies under wind loads and thermal stress situations. On the other hand, trade-off between higher land utilization and lower block ratio is also a hot spot. Thalange et al.^[64] presented the protocol and results of systematic structural analysis of tripod heliostats to reduce the cost and enhance the mechanical behavior. Besarati and Yogi^[65] developed a new and simple method to improve the calculation speed and accuracy for shading and blocking computation of the heliostat field. The Sassi method^[66] is used for the shading and blocking efficiency. A 50 MWth heliostat field in Daggett, California, USA was used as a case study for the proposed method. Wei et al.^[67] proposed a new method for the design of the heliostat field layout for solar tower power plant. Based on the new method, a new code for heliostat field layout design (HFLD) has been developed and a new heliostat field layout for the PS10 plant at the PS10 location has been designed using the new code. Compared with current PS10 layout, the new designed heliostats has the same optical efficiency but with a faster response speed.

Some researchers concerned about the performance of central receiver of power tower. Kim et al.^[68] investigated the heat loss of solar central receiver. Numerical simulations using CFD (Computational Fluid Dynamics) with the consideration of four different receiver shapes were carried out to get the influence on convection and radiation heat losses. Different opening ratio between cavity aperture area and receiver aperture area, receiver temperatures, wind velocities and wind directions (head-on and side-on) were considered for the simu-

lations. Results were used to get a simplified correlation model which gets the fraction of convection heat loss. The correlation obtained shows good agreements with the simulation results. The correlation was also validated with experimental data from three central receiver systems (Martin Marietta, Solar One and Solar Two). Lara et al.^[69] presented a novel modeling tool for calculation of central receiver concentrated flux distributions. The modeling tool is based on a drift model that includes different geometrical error sources in a rigorous manner and on a simple analytic approximation for the individual flux distribution of a heliostat.

Some researchers devoted on the simulation of power tower plants. Franchini et al.^[70] developed a computing procedure for solar tower system under both nominal and part load conditions. A Siemens gas turbine product, SGT-800, was applied for the Integrated Solar Combined Cycle (ISCC) as a study case for the solar tower system. The turbine has a dual pressure heat recovery steam generator, which can be used for the Integrated Solar Combined ISCC plant. A model of Solar Rankine Cycle (SRC) driven by power tower was also developed for comparison. A highest solar-to-electric efficiency of 21.8% can be achieved by the designed ISCC plant. And in all conditions, the global solar energy conversion efficiency of the ISCC is higher than that of the SRC. Xu et al.^[71,72] created a model of the 1 MW Dahan solar thermal power tower plant using the modular modeling method. The dynamic and static characteristics of the power plant are analyzed based on these models. Response curves of the system state parameters are given for different solar irradiance disturbances. Conclusions in this paper are good references for the design of solar thermal power tower plant. Benamar et al.^[73] developed a mathematical model based on energy analysis for solar tower power plants. A general nonlinear mathematical model of the studied system has been presented and solved using numerical optimization methods. The analysis of these results shows the existence of an optimal receiver efficiency value for each steam mass flow, receiver surface temperature and receiver surface area.

1.2.4 Cascade solar system

To fully utilize the features of components of solar thermal power system, cascade solar systems are researched by many researchers. There are mainly two directions of the research of cascade solar systems. One is cascade collection, the other is cascade utilization.

1.2.4.1 Cascade collection

Some researchers have investigated the combination of different types of collectors for CSP to achieve cascade solar collection. Suzuki^[74] analyzed the solar thermal systems with two different types of collectors connected in series. A value of the collectors, the product of the collector efficiency factor and the optical efficiency, was revealed to be the key factor to determine whether a cascade system is better than either one of the collectors alone. If the value of the lower concentration ratio collector is larger than that of the higher concentration ratio, the cascade system is more effective. Furthermore, it was found that to obtain the maximum energy gain, there exists the optimum operating conditions.

Kribus et al.^[75] proposed an idea of using separate aperture stages for different irradiance distribution. The working fluid is gradually heated when it flows through the receiver elements with increasing irradiance levels. A two-stage system was set up to demonstrate this principle at the Weizmann Institute's Solar Tower. Air was used as the HTF to obtain 750°C after the low-temperature stage and 1000°C after the high-temperature stage. Figure 1-3 shows the two-stage receiver system.

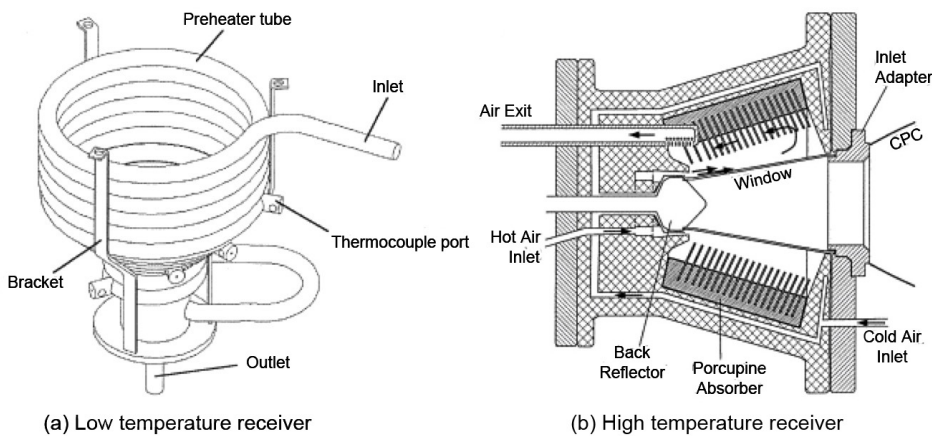


图 1-3 Two-stage receiver system

Gordon and Saltiel^[76] presented an analytic method for predicting the long-term performance of solar energy systems with more than one collector brand (“multistage” systems). This procedure enables the designer to determine the most cost-effective method of combining different collector brands for a given load. The analytic method is illustrated by a solved example which shows that significant savings can be realized by combining different

collector brands for a given application (multi-staging).

Oshida and Suzuki^[77] presented the idea of optical cascade heat collection of solar energy. Two absorbers, one warm and the other hot, are used in the cascade system. The warm absorber is heated by the Fresnel lenses and the hot absorber is heated by CPC. HTF flows into the warm absorber firstly and then flows into the hot absorber. The temperature of HTF can increase more effectively by the cascade heating design.

Desai et al.^[78] presented an integrated CSP plant configuration with the combination of both PTC and LFC. Thermo-economic comparisons between PTC-based, LFC-based and integrated CSP plant configurations, without hybridization and storage, were analyzed. Figure 1-4 shows a simplified schematic of a proposed integrated CSP plant configuration. It is demonstrated that the cost of energy of an integrated CSP plant is 9.6% cheaper than PTC-based CSP plant and 13.5% cheaper than LFC-based CSP plant.

Coco et al.^[79] developed four different line-focusing solar power plant configurations integrated both direct steam generation and Brayton power cycle. In these configurations, collectors are divided into different solar fields to supply different heat demands. This provides the ability to use different types of collectors (parabolic trough and linear Fresnel) in the systems.

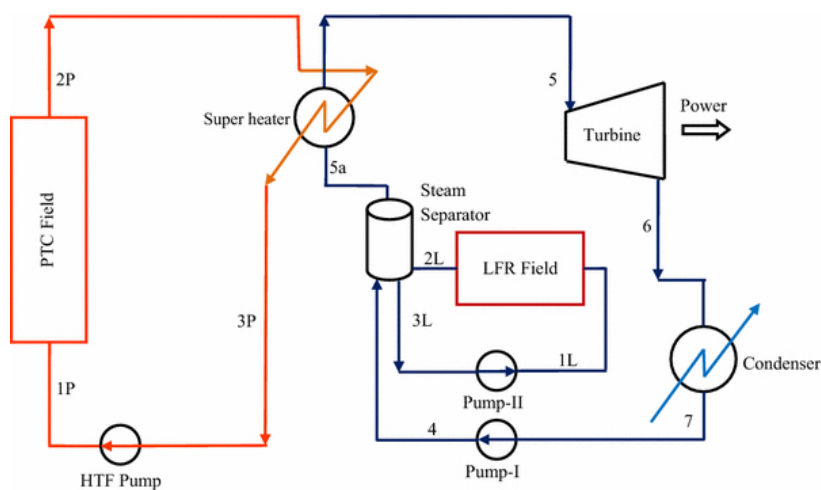


图 1-4 Simplified schematic of a proposed integrated CSP plant configuration

1.2.4.2 Cascade utilization

Many researchers have done the work on the combination of different thermodynamic cycles for CSP. Lots of the work focused on integrated solar combined cycle (ISCC) with parabolic trough, where Rankine cycle is used as the bottom cycle.

Li and Yang^[80] proposed a novel two-stage ISCC system that could reach up to 30% of the net solar-to-electricity efficiency as shown in Figure 1-5. In their research, the impact on the system overall efficiencies of how and where solar energy is input into ISCC system was investigated.

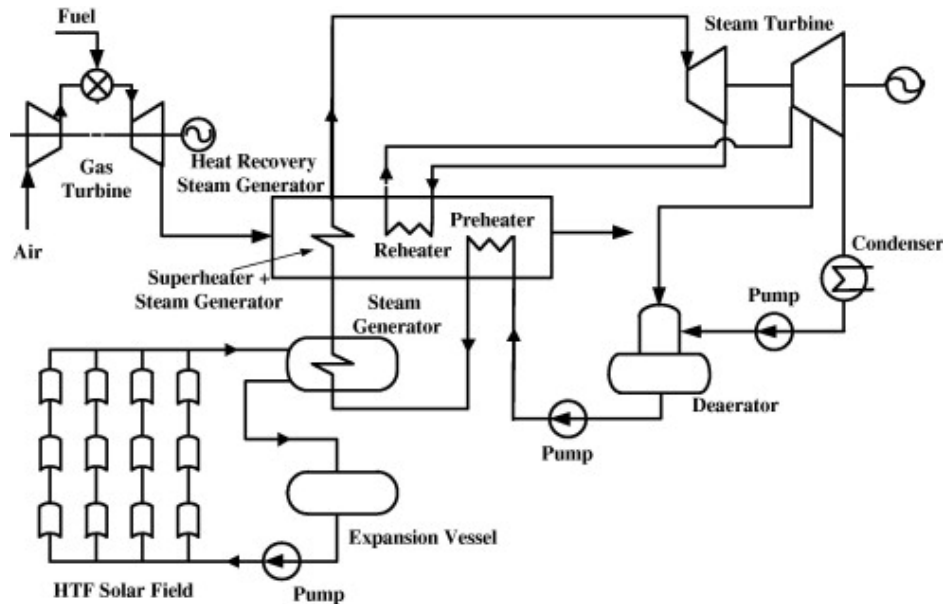


图 1-5 The proposed ISCC scheme

Gülen^[81] used the exergy concept of the second law of thermodynamics to simplify the optimization process of ISCCS. After the exergy analysis, physics-based, user-friendly guidelines were provided for ISCC designs.

Shaaban^[82] introduced a novel ISCC with steam and organic Rankine cycles. The ORC was used in order to intercool the compressed air and produce a net power from the received thermal energy. The proposed cycle performance was studied and optimized with different ORC working fluids. Figure 1-6 shows the schematic of the proposed ISCC.

Alqahtani and Dalia^[83] quantified the economic and environmental benefits of an ISCC power plant relative to a stand-alone CSP with energy storage, and a natural gas-fired com-

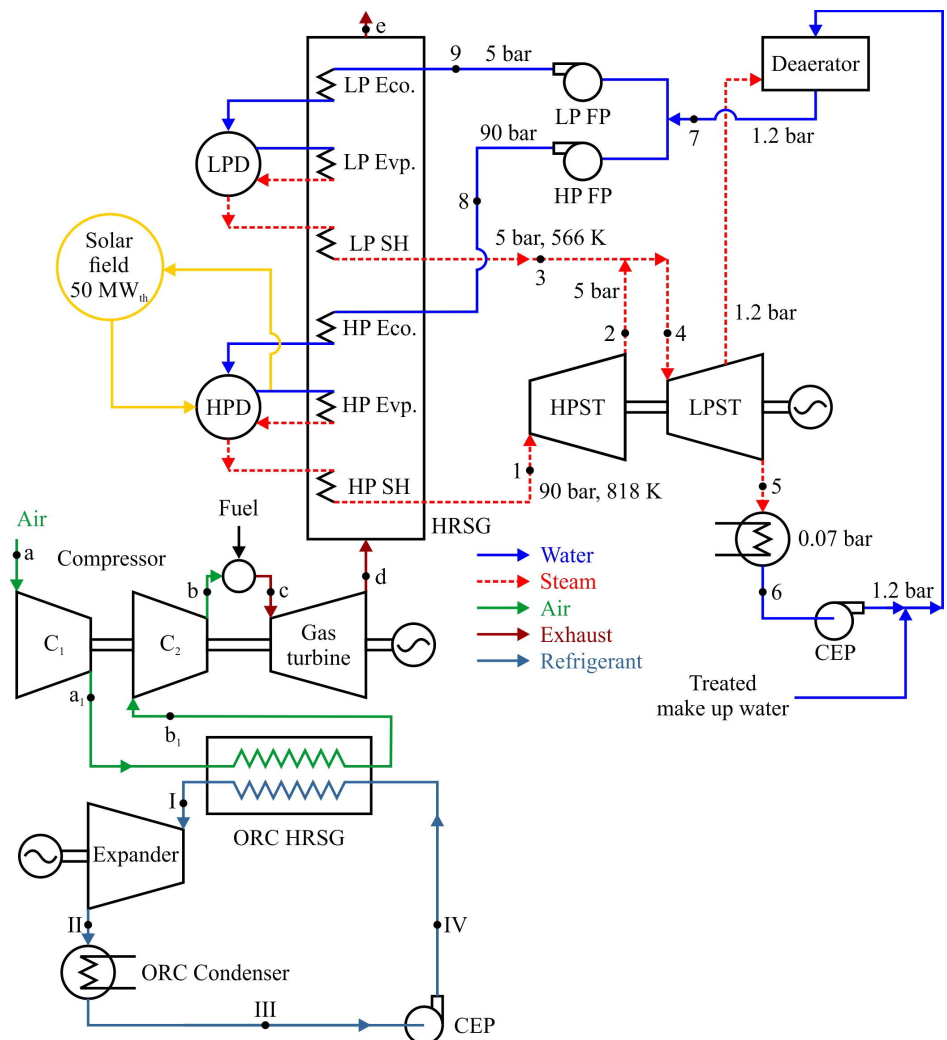


图 1-6 Schematic of the proposed ISCC with two bottoming cycles

bined cycle plant. Results show that integrating the CSP into an ISCC reduces the LCOE of solar-generated electricity by 35-40% relative to a stand-alone CSP plant, and provides the additional benefit of dispatch ability.

Manente^[84] developed a 390 MWe three pressure level natural gas combined cycle to evaluate different integration schemes of ISCC. Both power boosting and fuel saving operation strategies were analyzed in the search for the highest annual efficiency and solar share. Result shown that, compared to power boosting, the fuel saving strategy shows lower thermal efficiencies of the integrated solar combined cycle due to the efficiency drop of gas turbine at reduced loads.

Turchi et al.^[85] represented two new conceptual hybrid designs for ISCC with parabolic trough. In the first design, gas turbine waste heat is supplied for both heat transfer fluid heating and feed water preheating. In the second design, gas turbine waste heat is supplied for a thermal energy storage system.

Mukhopadhyay and Ghosh^[86] presented a conceptual configuration of a solar power tower combined heat and power plant with a topping air Brayton cycle. The conventional gas turbine combustion chamber is replaced with a solar receiver. A simple downstream Rankine cycle with a heat recovery steam generator and a process heater have been considered for integration with the solar Brayton cycle.

Li et al.^[87] presented a novel cascade system using both steam Rankine cycle and organic Rankine cycle. Screw expander is employed in the steam Rankine cycle for its good applicability in power conversion with steam-liquid mixture. The heat released by steam condensation is used to drive the organic Rankine cycle.

Al-Sulaiman^[88] compared the produced power of an SRC-ORC combined cycle with traditional SRC cycle. The SRC is driven by parabolic trough solar collectors, and the ORC cycle is driven by the condensation heat of the SRC.

Dunham and Lipi^[89] proposed a single Brayton and a combined Brayton-Rankine power cycle for distributed solar power generation and compared its theoretical efficiency to a single Brayton cycle. Different working fluids were examined as working fluids in the bottoming Rankine cycle. It is found that the combination of the Brayton topping cycle using carbon dioxide and the Rankine bottoming cycle using R-245fa gives the highest combined cycle efficiency of 21.06%, while a single Brayton cycle is found to reach a peak cycle efficiency of 15.31% with carbon dioxide at the same design point conditions.

Bahrami et al.^[90] proposed a combined ORC power cycle. An ORC was used as the cold-side heat rejector of a Stirling engine. The operating temperatures of the ORC are between 80°C and 140°C and the combined system can achieve 4% to 8% higher efficiency compared with a standard Stirling cycle.

Thierry et al.^[91] proposed a nonlinear optimization formulation of multistage Rankine cycle with two types of configurations. Both cascade style and series style of the ORC are considered. The results show that for some cases the multistage configurations can achieve higher efficiency at low temperature.

Bahari et al.^[92] considered the optimization of an integrated system using organic Rank-

ine cycle to utilize the heat released by the Stirling cycle. However, the integrated system is a primitive design and it takes no consideration of the application in CSP.

1.3 Literature summary

Reviewing the former literatures concerning solar thermal power it can be found that most of the research works have focused on specific solar thermal power technologies to increase efficiency or reduce costs.

A small number of researchers have also studied the cascade collection or cascade utilization of solar energy.

There is no literature on the combination of cascade collection and cascade utilization in one cascade solar thermal power system. No systematically analysis of the cascade system has been found.

1.4 Research content

This research is based on the international cooperation project "Collaborative research on key technologies to produce electricity by cascade utilization solar thermal energy" as the background. The objective of this project is to research the equipment of solar thermal power generation system, to propose, develop and optimize a solar thermal cascade system depending on the advantages and disadvantages of the solar thermal power generation systems, and to explore a new feasible technology for large-scale solar thermal power generation. The main research contents of this thesis are as follows:

- (1) Selecting reasonable topologies for cascade solar thermal power generation systems.
According to the thermodynamic characteristics and operating behaviors of components in thermal power generation systems, reasonable topologies are selected. These topologies should be able to embody the benefits of cascade systems and help to improve the performance of solar thermal power system.
- (2) Establishing the mechanical model of each component in solar thermal power generation system. Based on the governing equations and operating characteristics of each component, a mechanism model will be established. Object-oriented features will be applied to create component models easy to combine, extend, and replace.
- (3) System modeling for each proposed cascade system scheme. Based on the mechanism

models of the components, a software that provides the functions of system topology arrangement, component connection, parameter setting and environment selection will be developed for the system investigation.

- (4) Optimizing the subsystem of the cascade system. Specifically, a staged heating method will be analyzed for the optimization of the steam generating system. Different layouts of Stirling engines will be analyzed to find out best layouts of the Stirling engines in the cascade system.
- (5) Finding out the conditions conductive for cascade solar thermal power application. Selecting appropriate stand-alone systems for comparative analysis of the cascade systems. Analysis of the influences of various parameters on the efficiency difference between cascade system and its corresponding stand-alone systems will be conducted.
- (6) Building a solar thermal power generation test platform to carry out experimental works for solar thermal power generation. Special experiment cases considering the features of solar irradiance need to be designed to investigate the impact of different factors on the system performance. Influences of different factors on the performance of components will be investigated. Thermal performances of trough collectors and dish collectors will be analyzed, and the simulation models will be validated.

二 系统拓扑结构

2.1 系统拓扑结构的设计

本文的研究目的是分析太阳能光热发电系统的设备的特点,根据现有太阳能光热发电技术的优缺点,提出、开发和优化梯级太阳能光热发电系统。

现有的经过商业验证的太阳能热发电技术有三种——太阳能槽式发电,太阳能碟式发电和太阳能塔式发电。由于太阳能塔式发电系统占地面积较大,投资成本太高,考虑到未来需要搭建太阳能光热梯级发电示范系统,本文仅选择两种太阳能光热发电技术(太阳能槽式发电和太阳能碟式发电)作为太阳能光热梯级发电系统设计的基本系统。为了实现对太阳能碟式集热器获得的高温热量进行梯级利用,采用空气(或氮气)作为太阳能碟式发电系统的传热介质来传输所收集的热量。典型的太阳能槽式发

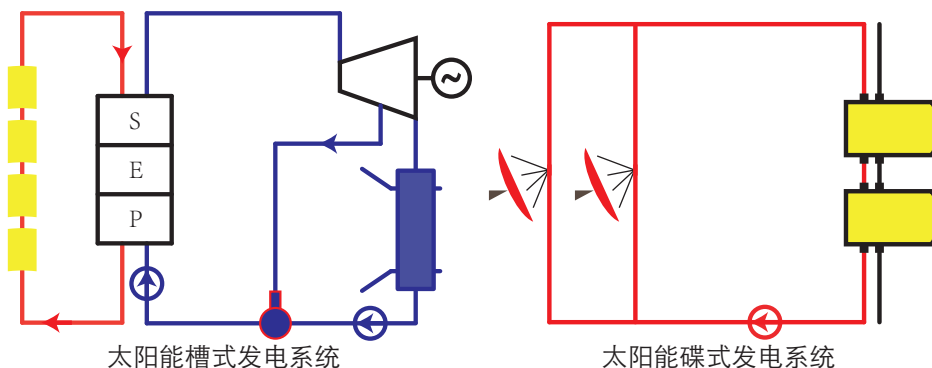


图 2-1 太阳能槽式发电系统和太阳能碟式发电系统结构示意图

电系统和太阳能碟式发电系统的结构示意图如图2-1所示。为使本文中的系统结构图更加清晰和一致,图2-2列出了太阳能光热发电系统中可能出现的所有元件的图例。

利用这两种基本系统,通过选择不同的系统拓扑结构,来实现能量的梯级收集和梯级利用。由于梯级系统的拓扑结构需要考虑多种因素,例如水工质朗肯循环或有机工质朗肯循环、多种集热器的配合使用、不同热工循环的组合等,梯级系统可以组合的拓扑结构的数量非常之多。为了获得最合适的梯级系统拓扑结构,需要从可行性、经济性等角度仔细分析这些因素。

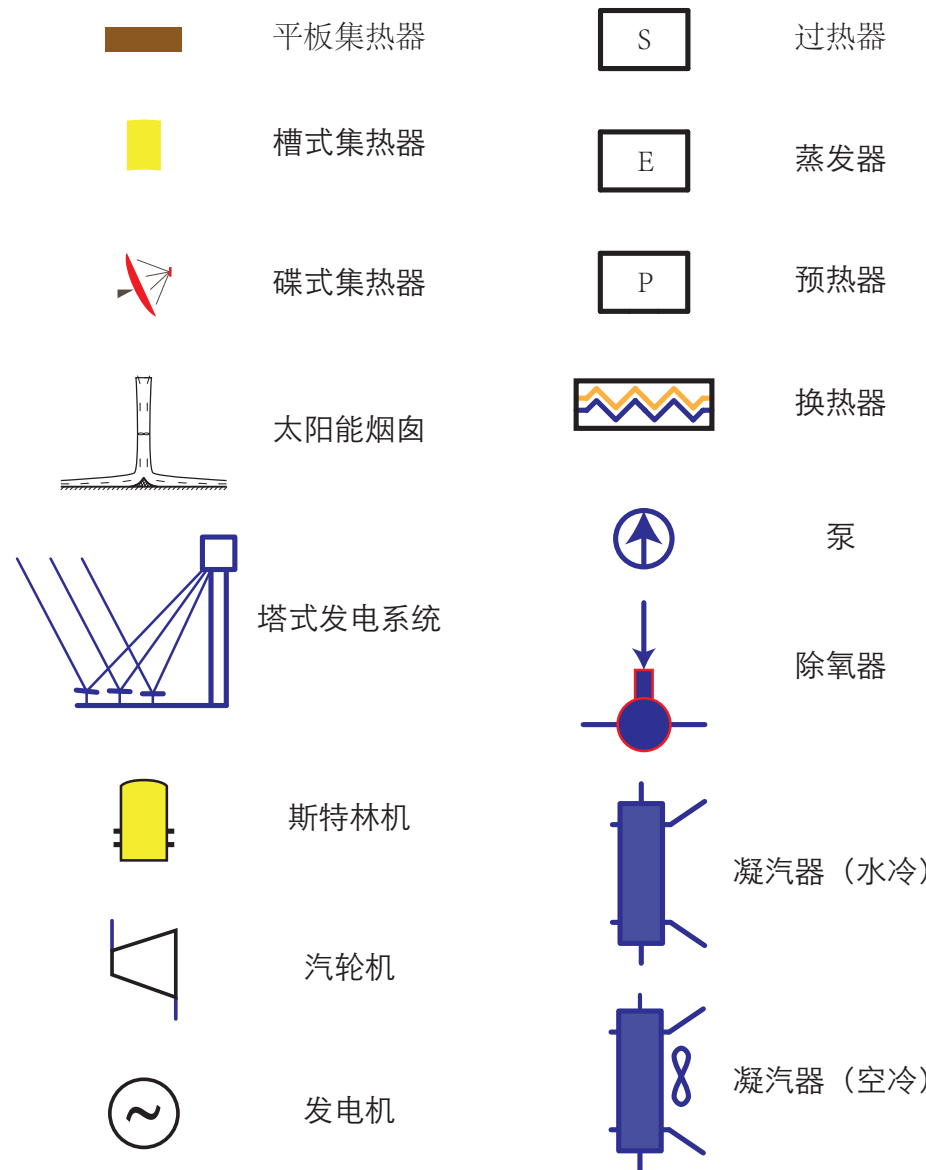


图 2-2 太阳能光热发电系统中的元件列表

2.1.1 朗肯循环工质

不同应用于朗肯循环的工质的温熵曲线如图2-3所示。需要说明的是，图中各曲线只是用于表示不同工质的饱和曲线形状，曲线对应的熵值和温度不代表其真实熵值和温度，也不能用于不同工质之间的比较。其中，理想工质具有以下特点^[93]：

- 饱和液体的比热容要小，这样图2-3中的曲线 2-2' 才接近竖直。
- 临界点温度要高于最高运行温度，以便于所有的吸热过程都发生在临界点温度

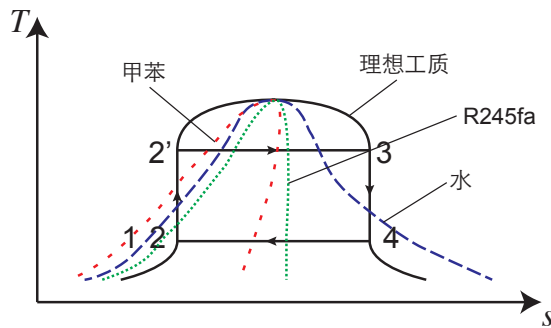


图 2-3 用于朗肯循环的理想工质的温熵图

以下。

- 最高运行温度所对应的饱和蒸汽压力应该适中，以便安全运行并有利于降低设备的制造成本。
- 凝气温度下对应的蒸气压力应该高于大气压，以避免空气泄漏到系统中。
- 状态点 4 的蒸气的密度应该较大，这样可以避免大直径的汽轮机叶片，壳体和换热器。
- 图2-3中气态饱和曲线 3-4 应该接近竖直，从而避免汽轮机中的工质膨胀进入湿蒸汽区($ds/dT < 0$ 的情况)或是过热区($ds/dT > 0$ 的情况)。
- 对于小功率汽轮机的应用，工质应该具有较高的分子量以减小汽轮机的转速和(或)级的数量，并且允许合适的质量流量和汽轮机喷嘴面积。
- 工质在常温常压下为液体，以便于运输和控制。
- 工质的凝固点应该低于工作的环境温度。
- 工质具有良好的传热性能，价格便宜，在最高操作温度下热稳定较好，不易燃烧，无腐蚀性，无毒性等。

水是朗肯循环中最常用的工质，水工质朗肯循环的各部件相关的技术比其他工质更为成熟。水的价格便宜(虽然锅炉级的水必须是高度蒸馏的，因此成本比自来水高)，水工质朗肯循环的高压部分的密封并没有其它工质那么重要。此外，蒸汽的不易燃性和可用性是其额外的优点。因为它的临界温度和压力分别为 374°C 和 22 MPa ，它可以在中等压力下实现较高温度的等温吸热。典型水工质朗肯循环太阳能光热系统的示意图如图2-4a所示。

水工质朗肯循环也存在一些缺点。蒸汽的低温特性并不理想，因为蒸汽在常温下具有很低的蒸气压和密度(参见表2.1)。对于低压部件，保持密封性，防止空气泄漏是

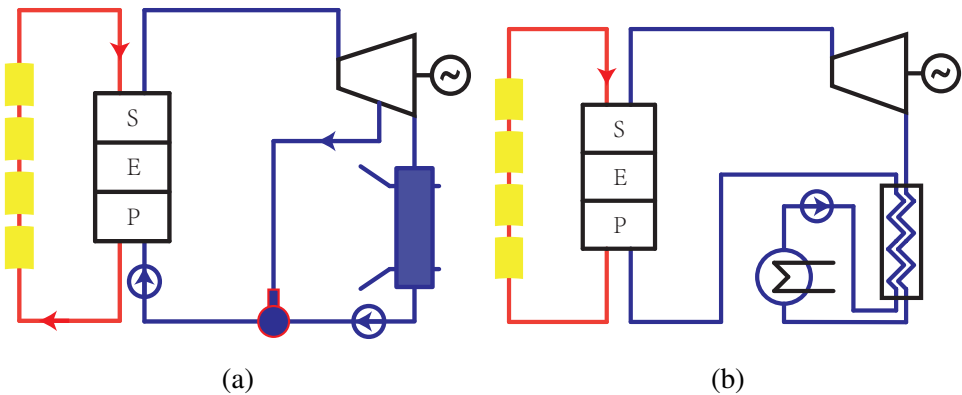


图 2-4 典型的水工质和有机工质的朗肯循环的太阳能光热系统结构示意图

设计中主要关注的问题。

表 2.1 对应温度下的饱和蒸气的压力和密度

$T(K)$	373.15	363.15	353.15	343.15	333.15	323.15	313.15	303.15	293.15
$p(Pa)$	101322	70117	47373	31176	19932	12344	7381	4246	2339
$\rho(kg/m^3)$	0.5982	0.4239	0.2937	0.1984	0.1304	0.0831	0.0512	0.0304	0.0173

有机工质朗肯循环(ORC)也可应用于太阳能槽式发电,取代常见的水工质朗肯循环。ORC可以在小功率和低集热温度的条件下进行发电,因此可以用于生产低成本,小规模的分布式 CSP 装置。ORC 中使用的大多数有机工质是干流体(温熵图上 $ds/dT > 0$)。汽轮机出口的气体具有一定的过热度,由于汽轮机出口温度高于冷凝器温度,所以可以将一部分热量传递给压缩过的液态有机工质。回热器就是为了利用这一部分热量而设计的,回热器为过热蒸气-过冷液体换热器。典型的有机工质太阳能光热系统结构示意图如图2-4b所示。

与水工质朗肯循环相比,它具有以下优点:

- 在中等转速和单级或双级的设计条件下可以实现小型汽轮机。
- 较低的体积比更有利于流道的设计。
- 较高的体积流量和音速值便于设计合理大小的流通面积。
- 有机工质在膨胀的过程中温降很小,这有利于减少热应力导致的各种问题。
- 干流体可以避免由于乏气存在湿度造成的叶片侵蚀。

- 较低的系统运行压力便于一体化设计。

2.1.2 太阳能烟囱

太阳能烟囱电站也被称为太阳能气流电站,直接(不聚光)利用太阳产生的热能来发电。太阳能烟囱发电系统由太阳能集热棚、太阳能烟囱和涡轮机发电机组3个基本部分所构成,典型的太阳能烟囱电站的示意图如图2-5所示。太阳能烟囱电站建立在太阳辐射强度高、土地保温性能好的地区。集热棚离地面有一定距离,其外围周边是开放的。太阳能烟囱和集热棚连接,位于集热棚中央。涡轮机发电机组位于烟囱底部。在这种电站中,空气在半透明的集热棚下由于温室效应而升温,由于集热棚的周边是开放的,外部空气由于密度分布不同而流入集热棚,然后在浮力的作用下热空气流入烟囱。在气流的路径上设置有涡轮机发电机组,用于将气流的动能转化为电能。

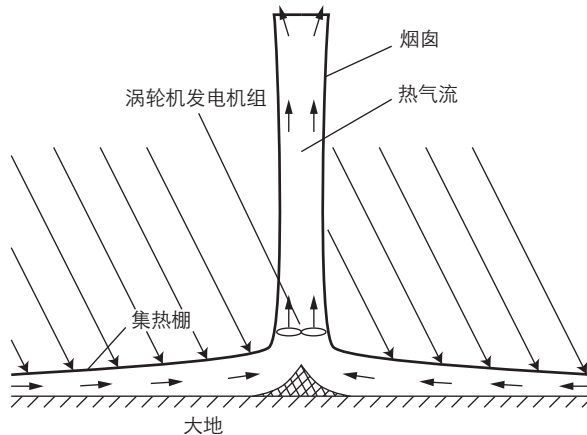


图 2-5 太阳能烟囱电站的结构示意图

太阳能烟囱可以利用低温热源(低品位能源)发电。因此,槽式系统和太阳能烟囱的组合可以作为能源梯级利用的有效途径。在组合系统中,朗肯循环中的冷凝器是采用空冷。空冷风扇将冷却过冷凝器的热空气从太阳能烟囱的周边吹入太阳能烟囱发电厂。热气流汇聚在烟囱底部,在浮力作用下向上流动,带动烟囱内的涡轮机发电机组,从而实现朗肯循环凝结热的有效利用。图2-6显示了一个槽式系统和太阳能烟囱组合的例子。

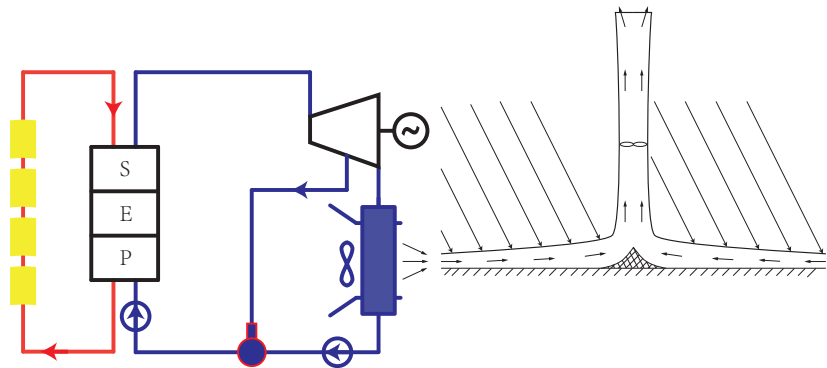


图 2-6 槽式系统和太阳能烟囱组合结构示意图

2.1.3 集热器串联连接

考虑到不同类型集热器的集热温度不同,采用不同类型集热器的串联连接是梯级集热的一种可行方案。槽式集热器和菲涅耳集热器更适合于低温集热,碟式集热器和塔式集热器更适合于更高温度的集热。串联连接利用不同类型的集热器可以有效利用它们各自的优点。图2-7给出了一个采用集热器串联连接的梯级系统的例子。在这个系统中,空气作为传热介质在流入碟式集热器之前先被槽式集热器预热。槽式集热器用于收集低温热能,碟式集热器用于收集高温热能。

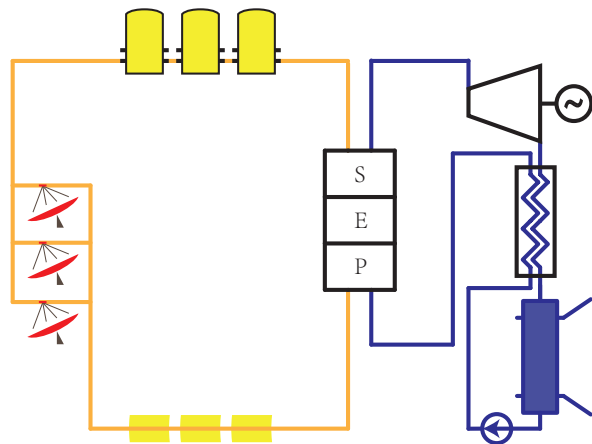


图 2-7 一种采用集热器串联连接的梯级系统

2.1.4 直接产蒸汽

在太阳能槽式系统中采用直接产蒸汽(DSG)技术被认为是太阳能光热发电应用中可以同时提高系统效率并降低成本的选择。它允许更高的循环温度，并可以带来更高的朗肯循环效率。常规太阳能槽式系统中，传热流体(通常是合成油或熔融盐)用于将收集到的热能传递给朗肯循环做功工质。这会导致较高的压力损失，限制了传热流体相关设备的运行维护成本。此外，朗肯循环的最高温度受到传热流体温度的限制，而且传热流体与朗肯循环的工作介质之间存在较大的温差。因此，传统太阳能槽式系统的光电转换效率并不高。在太阳能集热器的接收管中直接产蒸汽是降低成本并提高系统效率的方法之一。典型的 DSG 太阳能系统的示意图如图2-8所示。

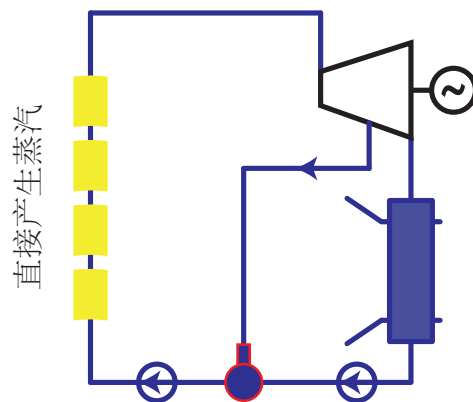


图 2-8 典型的 DSG 太阳能系统示意图

2.1.5 回路间的传热

不同回路之间的传热可用于实现能量的梯级利用。根据图2-1所示的两个基本太阳能系统，可以在太阳能梯级系统中应用两种类型的换热器。

第一种是在空气回路和导热油回路之间使用空气-导热油换热器。图2-9是使用了这种换热器的一个梯级系统实例。在这个系统中，热空气在为斯特林机组供热后，再流过空气-导热油换热器为导热油提供热量。

第二种是在空气回路和水回路之间使用空气-水换热器。图2-10a和图2-10b是使用了这种换热器的两个梯级系统实例。图2-10a中，热空气在为斯特林机组供热后，再流经空气-水换热器，为水的过热过程提供热量。图2-10b中，热空气在为斯特林机组供热后，再流经空气-水换热器，为水的预热过程提供热量。

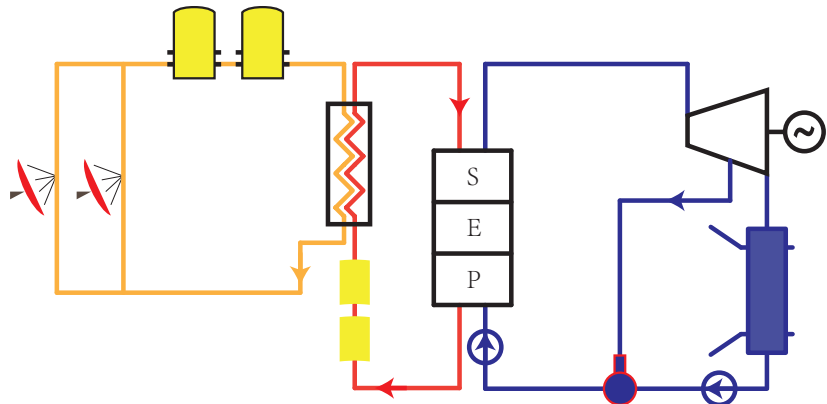


图 2-9 使用空气-导热油换热器的太阳能光热系统示意图

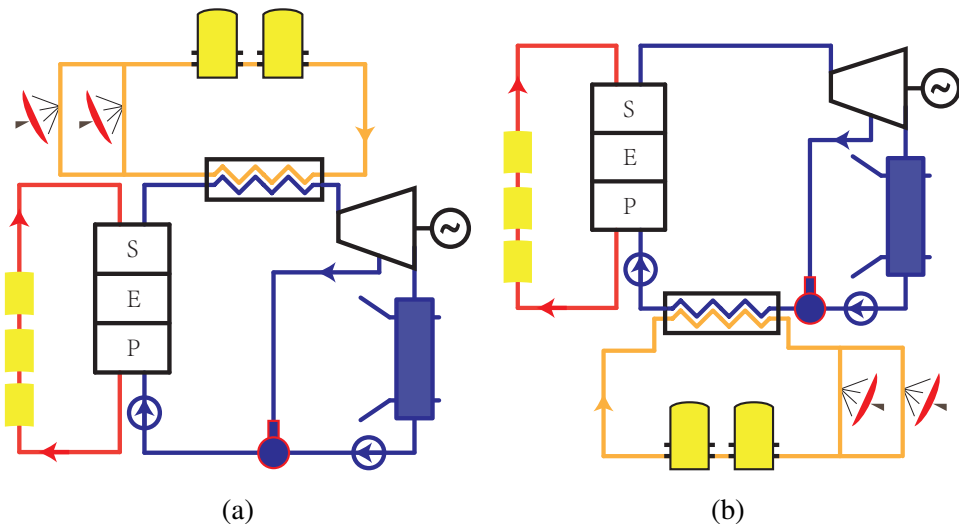


图 2-10 两种使用了空气-水换热器的梯级系统实例

2.1.6 循环之间热量利用

根据热力学第二定律,不可能从单一热源吸热使之完全转换为有用的功而不产生其他影响。对于热机,它同时需要热源和冷源来将热能转化为机械能。典型热机的热功转换图如图2-11所示。在热力循环中,从热源吸收的热量,只有一部分可以通过热机转化为机械功,其它部分需要传递到冷源。卡诺定理从根本上限制了与热源温度和冷源温度有关的热功转换比,即 $\frac{W}{Q_H} \leq \frac{T_H - T_C}{T_H}$, 其中 T_H 和 T_C 的单位为 K。

对于太阳能光热应用,仅考虑外部加热的热机。与在工作流体内产生热量的内燃机不同,外部加热的热机需要通过换热器向工作流体添加外部热量。

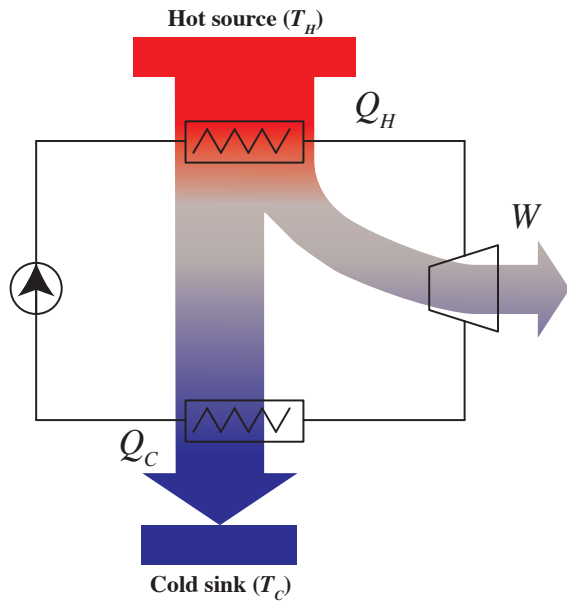


图 2-11 典型热机的热功转换图

根据热力循环型式的不同,有三种设计成接受外部热量的热机,它们都已经应用于太阳能光热应用。这三种热机所采用的热工循环型式为朗肯循环(Rankine cycle)、斯特林循环(Stirling cycle)和布雷顿循环(Brayton cycle)。其中,朗肯循环和布雷顿循环都适用于恒压加热。

最初的布雷顿热机使用活塞式压缩机和活塞式膨胀机,但更现代化的燃气轮机和吹气式喷气发动机也遵循布雷顿循环。尽管循环通常是一个开放的系统,但为了进行热力学分析,通常假定废气被重新用作进气,使得整个过程可以被分析为闭式循环。斯特林机采用往复式活塞设计,可将外部加热结合到恒温加热过程中。在朗肯循环中,加压液体进入换热器,在换热器中由外部热源以恒定压力加热成为蒸气。

这三种循环具有不同的最佳工作温度。朗肯循环的最佳工作温度最低,布雷顿循环的最佳工作温度最高。太阳能光热应用中使用的三种热力循环的 $T-s$ 图如图2-12所示。

2.2 系统拓扑结构的选择

2.2.1 朗肯循环工质

选择朗肯循环太阳能系统的传热流体时需要考虑两个重要方面:

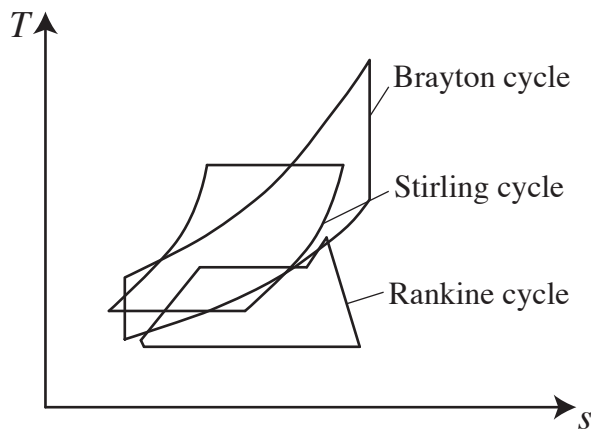


图 2-12 太阳能光热应用中所使用的三种热力循环的 T - s 图

1. 选择的传热流体易于在最佳运行温度条件下运行。对于朗肯循环太阳能光热系统，集热器效率随着工作温度的升高而降低，朗肯循环的效率随着工作温度的升高而升高，系统的总效率存在如图2-13所示的最佳工作温度。传热流体应当有利于达到该最佳工作温度。
2. 如果使用传热流体，则传热流体的状态需要和热力循环的工作流体的状态相匹配。一方面，工作流体的工作温度应该低于传热流体的收集温度。另一方面，工作流体的工作温度不应该比传热流体的收集温度低很多，以避免热交换过程中产生大量的熵损失。

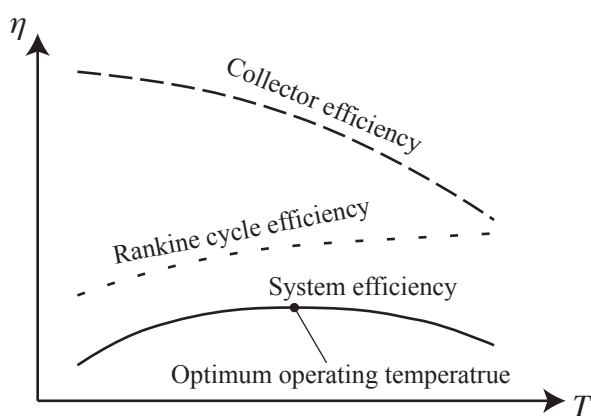


图 2-13 不同运行温度下的效率曲线

第2.1.1节中详细介绍了水和有机流体作为朗肯循环的工作流体的优缺点，很清

楚,对于低参数和小容量的配电发电,有机流体将是更好的选择,否则水是更好的选择。Bao 和 Zhao^[98]对工作流体的选择(包括纯液体和混合液)进行了全面的综述。在该综述中,考虑了许多因素,如操作条件,工作流体的特性,设备结构和环境安全等。必须指出的是,工作流体的种类(主要是干流体或湿流体)会影响系统的运行和布局。

2.2.2 太阳能烟囱

第2.1.2小节提出了将太阳能烟囱连接到太阳能槽式光热发电技术的观点。然而,目前的太阳能烟囱系统的效率非常低。Bilgen 和 Rheault 利用 MATLAB 建立了 5MW 的太阳能烟囱模型^[99]。他们对不同地理位置,不同烟囱高度和集热器高度的太阳能烟囱电站进行了模拟分析。其主要设计数据如表2.2所示。初步的设计参数为太阳辐射强度为 1000W/m² 和额定功率为 5MW。从表中可以看出,烟囱效率和系统总效率都很低,太阳能烟囱技术仍处于发展阶段。

表 2.2 太阳能烟囱设计参数及模拟结果

地理位置	Ottawa	Winnipeg	Edmonton	Schlaich
集热棚直径 (m)	1110	1110	1110	1110
集热棚面积 (m ²)	950000	950000	950000	950000
烟囱高度 (m)	123	60	35	547
集热器高度 (m)	848	975	1024	-
烟囱直径 (m)	54	54	54	54
集热棚内温升 (°C)	25.9	25.9	25.9	25.9
气流速度 (m/s)	9.1	9.1	9.1	9.1
总压头 (Pa)	518.3	518.3	518.3	383.3
平均效率				
集热棚 (%)	56.00	56.00	56.00	56.24
烟囱 (%)	1.82	1.82	1.82	1.45
涡轮机 (%)	77.0	77.0	77.0	77.0
系统整体 (%)	0.79	0.79	0.79	0.63

另外,太阳能烟囱成本高,占地面积大,不利于今后搭建太阳能光热梯级发电示范系统。鉴于这些考虑,梯级系统不采用太阳能烟囱。

2.2.3 集热器串联连接

每种类型的集热器都有其适宜的工作温度范围。使用串联的不同类型的集热器逐步加热传热流体是可行的。

根据基本系统(槽式-朗肯循环系统和碟式-斯特林机系统),在第2.1.3节(见图2-7)提出了一种集热器串联连接的方案。在这种方案中,空气依次在槽式集热器和碟式集热器中被加热。为斯特林机提供热量后,热空气流入换热器为朗肯循环提供热量。在这种拓扑结构中,空气被用作太阳能槽的导热油,这个想法目前只有少数研究人员进行了数值和实验研究,至今还没有商业应用^[27,100]。这种技术最大的技术难题在于,空气导热系数低,热容量低,导致系统效率非常低。为此,由于该拓扑结构使用了尚不成熟的空气槽式集热技术,固不采用这种方案。

有的太阳能塔式电厂采用水作为传热流体(如 Solar One 电厂),这时可以利用平板式太阳能集热器和(或)槽式集热器作为低温段的集热器。系统结构图如图2-14所示,冷凝水由平板式集热器加热,给水由槽式集热器加热。与太阳能塔式电厂相比,平板式集热器和槽式集热器的收集低温热量的单位热成本要低很多。平板式集热器和槽式集热器的串联连接加入可以有效降低系统发电成本。虽然该方案式有前途的,值得进一步研究,但本文的梯级系统不考虑采用太阳能塔式系统,所以该方案留给后续研究工作。

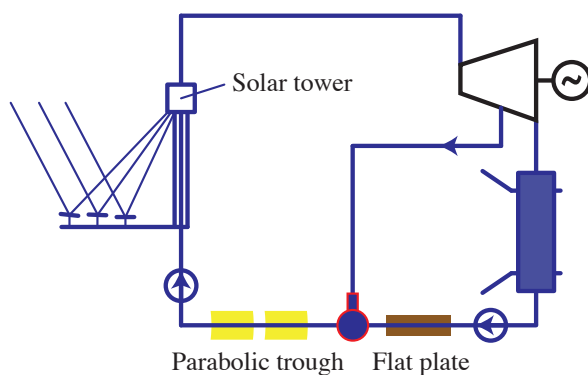


图 2-14 采用多种型式集热器串联连接的太阳能塔式发电系统

2.2.4 直接产蒸汽

在太阳能光热发电系统中应用直接产蒸汽技术所需部件较少,不存在传热温差等优点。水具有比合成油和太阳盐更低的凝固点,不需要像其他传热流体一样做大量的防冻保护措施。水的腐蚀性也比合成油和太阳盐小^[102]。此外,水的环境风险要远低于其它传热流体,DSG 电厂的泄漏不会对环境造成太大的破坏^[101]。

然而,除了在泰国的装机容量为 5 MWe 的泰国太阳能一号(TSE-1)工厂(泰国,2012)外,所有已建成的 CSP 商业工厂都应用间接蒸汽发电^[103]。这种方案被普遍接受的原因在于,吸热管中两相流区域的流量控制和制造工艺非常困难。槽式集热器的吸热管内两相流的存在,需要配备复杂而昂贵的控制系统,并需要较快的流速以避免出现层流。

此外,应当谨慎设计接收器,以确保蒸汽区域的光通量小于发生沸腾的区域。这是因为液体的传热系数明显高于过热蒸汽。如果二者光通量接近,则接收器存在蒸汽的区域则可能因不能快速带走热量而出现灼伤。还有许多集热器的跟踪系统要求接收器在跟踪太阳时改变其方位。这种方位的调整增大了含蒸汽的接收器部分接受到高光通量的可能性。

与 DSG 相关的另一个问题是与汽轮机入口压力相匹配,接收器管内的蒸汽压力比较高。事实上,在高压下处理形成收集器接收管的可移动和柔性部件是 DSG 技术面临的主要问题之一。

在未来的梯级系统中应用直接产蒸汽技术可能是一个较好的选择,然而,由于其技术尚不成熟,现阶段梯级系统的技术方案不采用直接产蒸汽技术。

2.2.5 回路间的换热

第2.1.5节介绍了两种可应用于太阳能梯级集热系统的换热器,空气-导热油交换器(参见图2-15)和空气-水换热器(参见图2-16)。

对于第一种类型,空气为导热油提供热量。从几个方面来看,这是不经济的。首先,导热油的温度并不能进一步提高。导热油的极限温度受到本身物质属性的限制,而并非受限于槽式集热器,槽式集热器的集热温度可以超过这个值。在高温条件下,油品可能会变质,蒸发,分解,对系统的稳定和安全运行产生不利影响。其次,使用碟式集热器为导热油提供热量是不经济的,因为碟式集热器是为了收集更高温度的热量而设计的,与槽式集热器相比,它的在收集中低温热量时效益更低。

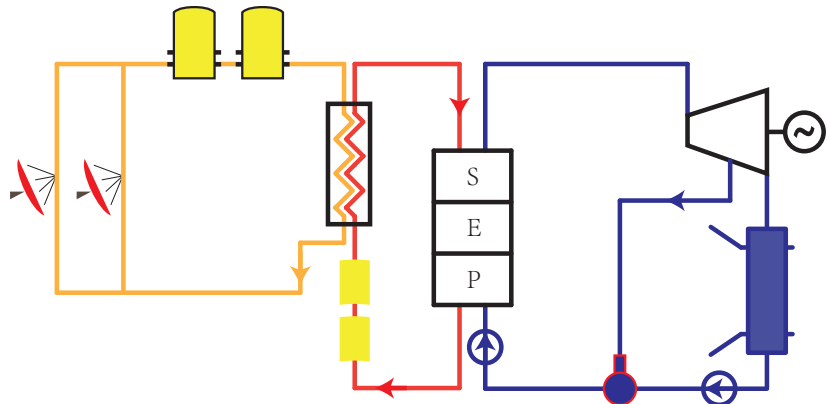


图 2-15 使用空气-导热油换热器的太阳能光热系统示意图

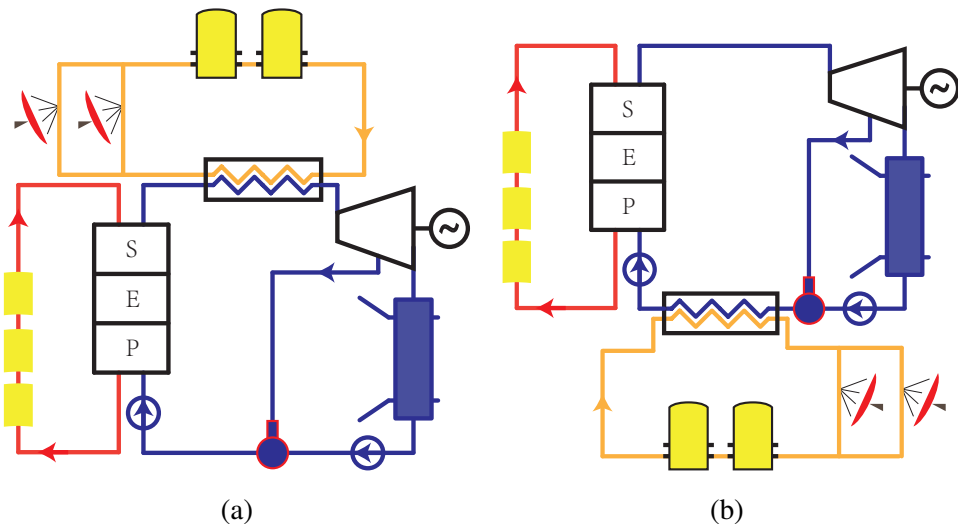


图 2-16 两种使用了空气-水换热器的梯级系统实例

对于第二种类型,空气为水提供热量。图2-16中给出了两种使用空气-水换热器的太阳能梯级系统方案。其中,图2-16a给出的是使用加热过斯特林机之后的热空气来继续为过热蒸汽提供热量的方案。这是可行的,因为热空气可以提升水的吸热过程的平均温度从而提高朗肯循环的效率。另一方面,在传统的太阳能槽式系统中,主蒸汽温度受到导热油极限温度的限制,这不利于提升朗肯循环的效率。在这个梯级系统中,朗肯循环的主蒸汽温度可以提高到高于 400°C 以消除导热油极限温度带来的负面影响。这一系统方案将作为主要研究方案在接下来的内容里详细讨论。图2-16b给出的是使用加热过斯特林机后的热空气预热给水的方案。由于斯特林机出口的空气温度较高,而朗肯循环的给水温度较低,二者之间存在很大的温差。如果采用此方案,则换

热过程产生的熵损很大。此外,由于给水温度的提升导致太阳能场内的导热油的平均温度也会有所上升,这将降低太阳能场的集热效率,进而降低整个系统的效率。

2.2.6 循环之间热量利用

正如在第2.1.6节中提到的,不同的热力循环有着在不同的最佳工作温度。由于每个热力循环都具有吸热和放热过程,因此可以组合多种热力循环,使一个循环(底部循环)吸收利用另一个循环(顶部循环)释放的热量。在我们的基本系统中(参见图Figure 2-1),朗肯循环和斯特林循环可以耦合起来用于梯级发电。

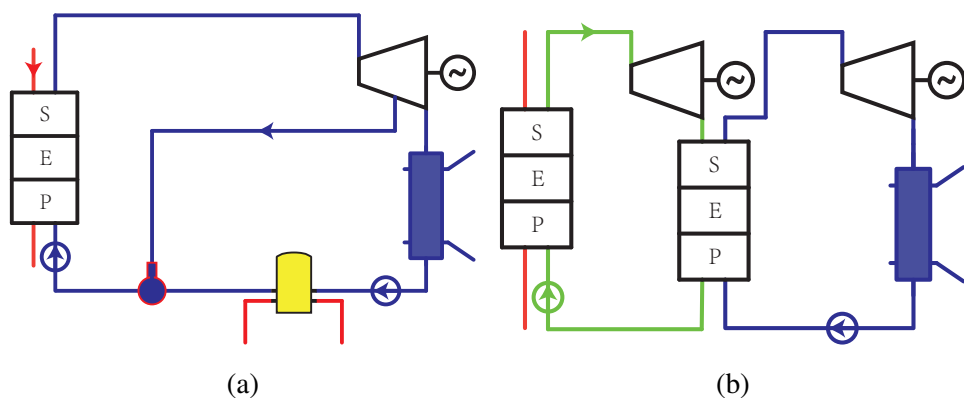


图 2-17 采用多个热力循环之间热量回收利用的梯级系统结构图

图2-17给出了热力循环之间热量回收利用的梯级系统的两种系统结构。传统的斯特林机为了提高性能,使用冷却水来吸收斯特林机释放的热量,吸收的热量被浪费掉而没有回收利用。在图2-17a中,采用朗肯循环的凝结液来冷却斯特林机。斯特林循环排出的热量可以通过朗肯循环回收利用。对于有机朗肯循环,不同的工作流体决定循环的工作温度区间。用一个有机朗肯循环重复利用另一个有机朗肯循环的凝结热是可行的。在图2-17b中,两个有机朗肯循环耦合在一起用于发电。底部循环利用顶部循环的凝结热来实现预热,蒸发和过热,再利用朗肯循环发电。

2.3 选定的梯级系统拓扑结构

考虑了第2.1节和第2.2节中的所有因素,本文选择了两个系统拓扑结构进行太阳能光热梯级发电技术的研究,其系统结构图如图2-18所示。

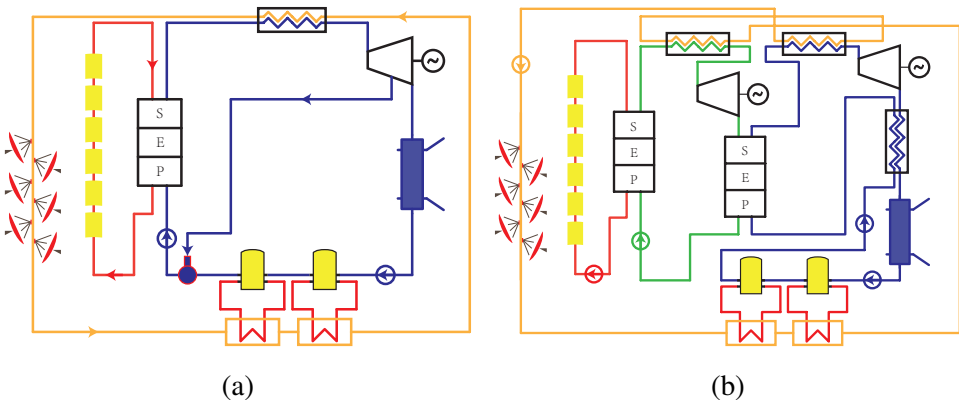


图 2-18 两种选定的梯级系统拓扑结构图

图2-18a中的梯级系统具有以下特点：

- 选用了多种型式的集热器。槽式集热器用于较低温度的集热，集热器用于较高温度的集热。这有助于降低成本并提高系统效率。
- 使用了多种型式的热力循环。朗肯循环适用于较低温度的热利用。斯特林循环适用于更高温度的热利用。二者工作区间的不同使得底部循环利用顶部循环的释放的热量成为可能。
- 使用了空气-水换热器。使用空气-水换热器来提高主蒸汽的温度，这有助于提高朗肯循环的效率。另一方面它克服了传统太阳能槽式系统中导热油极限温度较低的缺点，有助于实现比传统太阳能槽式系统更高的主蒸汽参数。
- 采用朗肯循环的凝结液来冷却斯特林机。采用朗肯循环的凝结液来冷却斯特林机。斯特林循环的废弃热量可以通过朗肯循环回收利用，这有助于提高整个系统的效率。

图2-18b中的梯级系统也具有上述特点。此外，它采用不同种类的有机工质作为工作流体，使太阳能光热系统具有更广泛的工作温度区间，可以适用于多种能量需求。它的一个计算案例如图2-19所示。本文将重点分析这两个梯级系统。但是，考虑到蒸汽朗肯循环的应用更加广泛，下面的章节将使用图2-18a所描述的系统作为主要的研究内容。

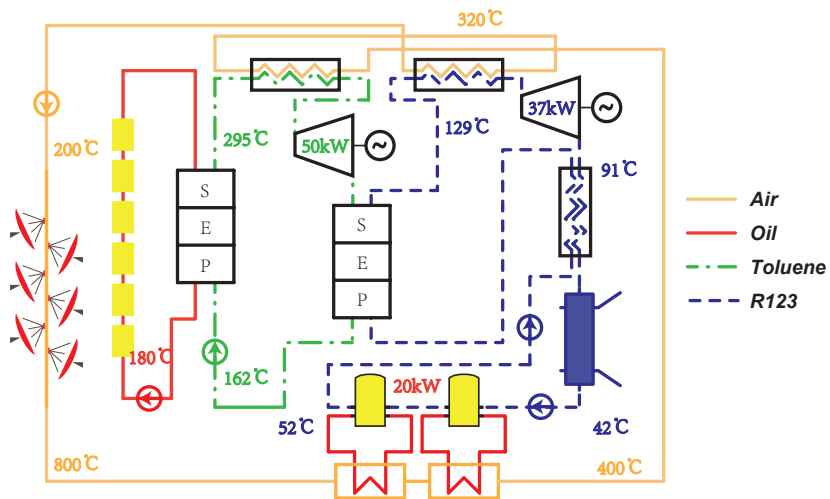


图 2-19 图2-18b的一个计算案例

2.4 本章小结

本章系统地介绍了太阳能光热梯级发电系统设计中的一些考虑因素。这些考虑因素包括朗肯循环工质类型,太阳能烟囱,集热器串联连接,直接产蒸汽,回路间的传热和循环之间的能量利用。接着,本文对这些考虑因素进行了仔细的研究。结合研究方向,经过分析和排除,提出了两种适用于太阳能光热梯级发电的典型的系统拓扑结构。这两种典型的系统拓扑具有以下特点:

- 使用了多种型式的集热器。
- 使用了多种型式的热力循环。
- 使用了空气-水换热器来提高朗肯循环的效率。
- 使用朗肯循环的凝结液来冷却斯特林机。

值得注意的是,系统拓扑设计的一些考虑因素有待后续研究工作进行研究。例如,塔式太阳能发电技术与槽式集热器和平板式集热器的组合,如图2-14所示,该系统结构有效地利用了各中集热器的工作特性,有利于提升系统的效率并降低系统成本。另外,当直接产蒸汽技术成熟时,考虑到其具有所需设备少,不存在温度损失的特点,值得将其应用于太阳能光热梯级发电系统。

III Modeling

To investigate the performance of the proposed cascade systems, mechanism models of the systems are developed with EES (Engineering Equation Solver) and MATLAB (Matrix Laboratory). Bottom-up design method is used for the system modeling. Firstly, the mechanism models developed in EES are used to validate the theoretical relationships of the models. Secondly, the component models are developed in MATLAB using object-oriented method. It makes full use of inheritance and polymorphism to ensure both the independence and the relevance of the components. Three circuits, air circuit, water circuit and oil circuit, are developed with some specific state parameters in some key components. Energy-based models of these key components are created on the basis of their thermodynamic behavior, heat transfer and the second law.

The following part introduce models of some key components.

3.1 Component modeling

3.1.1 Parabolic trough collector

Parabolic trough collector consists of a reflector and a receiver. The reflector (mirror) reflects direct normal radiation and concentrates it onto a receiver tube located at the focal line of the parabola. The receiver is typically a metal absorber tube with high absorption rate coating. An outer glass tube is used outside the absorber tube to reduce thermal losses and the space between the absorber tube and the glass tube is usually drawn into a vacuum to further reduce thermal losses.

Optical loss exists in the reflection process due to optical efficiency terms. The reflection terms can be listed as bellow^[4]:

- Shadowing factor
- Tracking error
- Geometry error
- Clean mirror reflectance
- Dirt on mirrors

- Unaccounted errors

Another term, incident angle modifier $K(\theta)$, should be concerned when the solar irradiation is not normal to the collector aperture. It is a function of the solar incidence angle to the normal of the collector aperture (θ).

$K(\theta)$ is expressed by the following equation concluded from trough collector testing conducted at SNL.^[5]

$$K(\theta) = \cos \theta + 0.000884\theta - 0.00005369\theta^2 \quad (3.1)$$

The optical losses are associated with five parameters (see Figure 3-1):

- (1) Reflectivity, ρ : only a fraction of the incident radiation is reflected towards the receiver. The fraction is determined by the reflector type and dirt condition. Reflectivity of commercial parabolic trough mirrors can be assumed to be 0.9 for washed mirrors.
- (2) Intercept factor, γ : a fraction of the direct solar radiation reflected by the mirrors does not reach the glass cover of the absorber tube due to either microscopic imperfections of the reflectors or macroscopic shape errors in the parabolic trough concentrators (e.g., imprecision during assembly). These errors cause reflection of some rays at wrong angles, and therefore they do not intercept the absorber tube. These losses are quantified by an optical parameter called the intercept factor, γ , that is typically 0.95 for a collector properly assembled.
- (3) Transmissivity of the glass tube, τ : only a fraction of the direct solar radiation reaching the glass cover of the absorber pipe is able to pass through it. The ratio between the radiation passing through the glass tube and the total incident radiation on it, gives transmissivity τ , which is typically 0.93.
- (4) Absorptivity of the absorber selective coating, α_{abs} : this parameter quantifies the amount of energy absorbed by the steel absorber pipe, compared with the total radiation reaching the outer wall of the steel pipe. This parameter is typically 0.95 for receiver pipes with a cermet coating, whereas it is slightly lower for pipes coated with black nickel or chrome.
- (5) Soiling factor, F_e : the dirt on reflectors will reduce the reflectivity, it needs to concern the soiling factor. The soiling factor F_e takes into account the progressive soiling of mirrors and glass tubes after washing.

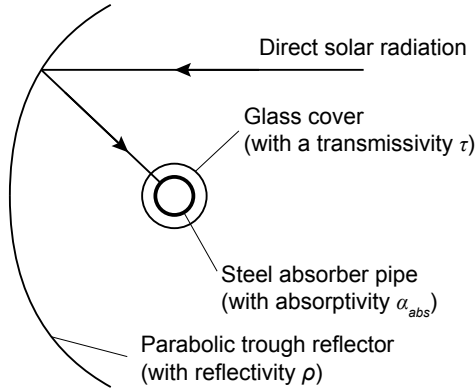


图 3-1 Some of the optical parameters of a parabolic trough

The energy passes through the glass tube to the receiver can be expressed by

$$P = I_r w_{tc} L_{tc} \rho \gamma \tau F_e K(\theta) \quad (3.2)$$

The solar energy absorbed by the absorber occurs very close to the outer surface, to simplify the absorption process, it is treated as a uniform heat flux q'' .

$$q'' = \frac{P}{\pi d_o L_{tc}} = \frac{I_r w_{tc} \rho \gamma \tau F_e K(\theta)}{\pi d_o} \quad (3.3)$$

Assume overall heat transfer coefficient $U(T_{abs})$ is uniform for whole length of the collector, and the heat transfer correlation in Appendix B can be applied. Figure 3-2 shows the schematic diagram of the thermal analysis of the absorber pipe.

$$\frac{T_o - T_{amb} - \frac{q''}{U(T_{abs})}}{T_i - T_{amb} - \frac{q''}{U(T_{abs})}} = \exp\left(-\frac{U(T_{abs}) \pi d_o L_{tc}}{\dot{m} c_p}\right) \quad (3.4)$$

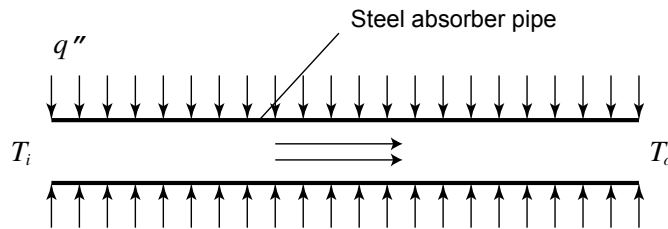


图 3-2 Schematic diagram of the absorber pipe

Since the Nusselt number Nu in the pipe is very large (about 1×10^4), small temperature difference exists between absorber and oil. So the average fluid temperature $(T_i + T_o)/2$ can be used as the average value of T_{abs} , and $U(T_{abs})$ can be expressed by the a second-order polynomial function given by Romero and Zarza^[104]. The length L_{tc} to get the required number of trough collectors in a row can be obtained from Equation (3.4).

The energy projected perpendicularly to the aperture of the trough collectors is

$$Q_{total} = I_r L_{tc} w_{tc} \quad (3.5)$$

The energy absorbed by the heat transfer fluid is

$$Q_{use} = \dot{m} c_p (T_o - T_i) \quad (3.6)$$

The thermal efficiency of the trough collectors

$$\eta_{tc} = \frac{Q_{use}}{Q_{total}} = \frac{I_r L_{tc} w_{tc}}{\dot{m} c_p (T_o - T_i)} \quad (3.7)$$

3.1.2 Parabolic dish collector

Parabolic dish collector consists of a reflector and a receiver. The reflector tracks the sun to reflect direct solar radiation and concentrates it onto a receiver located at the focal point of the reflector. Two axes tracking system needs to be applied for the reflector to continuously follow the daily path of the sun.

Two different methods are applied for the sun tracking systems:^[105]

- Azimuth elevation tracking by an orientation sensor or by calculated coordinates of the sun performed by the local control.
- Polar tracking, where the concentrator rotates about an axis parallel to the earth's axis rotation.

In a traditional dish-Stirling system, a Stirling engine is located at the focal point. The Stirling engine has a receiver to absorb the thermal energy from the concentrated sunlights. The receiver consists of an aperture and an absorber. The aperture in a Stirling receiver is located at the focal point of the reflector to reduce the radiation and convection losses. The absorber absorbs the solar radiation and transfers the thermal energy to the working gas of the Stirling engine. An electrical generator, directly connected to the crankshaft of the engine, converts the mechanical energy into electricity.

In a proposed cascade system, a volumetric receiver is located at the focal point. A spiral tube is located in the receiver to absorb the concentrated solar energy. Air (or nitrogen, is used as the heat transfer fluid) flows through the tube to transfer the absorbed energy as the heat source of Stirling engine(s).

The reflector is a key element of the systems. The curved reflective surface can be manufactured by attached segments, by individual facets or by a stretched membranes shaped by a continuous plenum. In all cases, the curved surface should be coated or covered by aluminum or silver reflectors.

A dish reflector product of SES (Stirling Energy System) is used in this cascade system, and its key parameters can be found in Table 3.1. The structure of the receiver is shown in Figure 3-3.

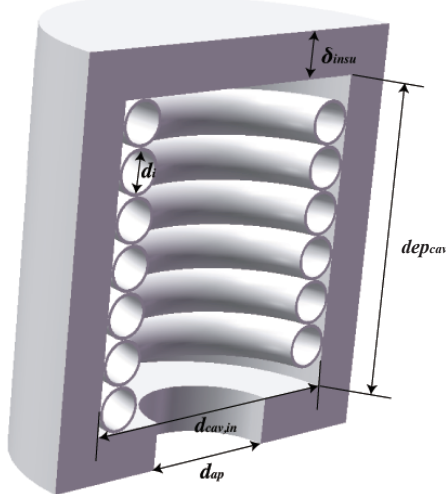


图 3-3 The structure of the dish receiver

The dish receiver model concerns the losses include: collector losses due to mirror reflectivity, receiver intercept losses, losses due to shading, and thermal losses. Thermal losses take the largest portion of all those losses, which are due to conduction, convection and radiation. Figure 3-4 shows the thermal network of dish receiver, which concerns the losses:

- Radiation losses reflected off of the receiver cavity surfaces and out of the receiver through the aperture. ($q_{rad,ref}$)
- Conductive losses through the receiver insulating layer. ($q_{cond,tot}$)

表 3.1 Key parameters of the dish collector

Parameter	Value	Parameter	Value	Parameter	Value
d_{cav}	0.46 m	ϵ_{insu}	0.6	θ_{dc}	45°
δ_{insu}	0.075 m	α_{cav}	0.87	γ	0.97
dep_{cav}	0.23 m	δ_a	0.005 m	$\eta_{shading}$	0.95
d_{ap}	0.184 m	$d_{i,1}$	0.07 m	ρ	0.91
λ_{insu}	0.06 W/(m · K)	A_{dc}	87.7 m ²		

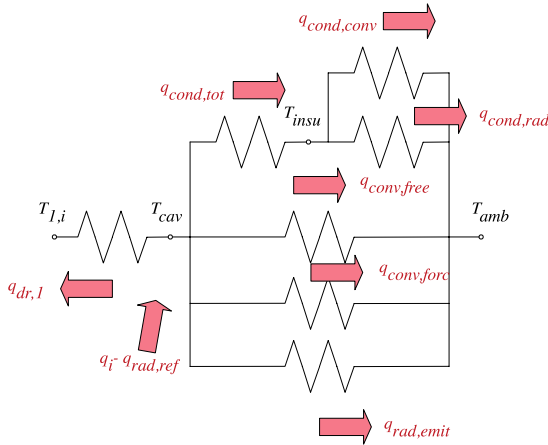


图 3-4 Thermal network of dish receiver

- Free convection from the cavity in the absence of wind. ($q_{conv,free}$)
- Forced convection in the presence of wind. ($q_{conv,forc}$)
- Emission losses due to thermal radiation emitted from the receiver aperture. ($q_{rad,emit}$)

To solve the thermal network in Figure 3-4, correlations and relationships of the heat fluxes should be clear.

(1) *Inlet energy from the reflector, q_i*

To simplify the model, influences made by receiver blocking and imperfection track are ignored.

$$q_i = I_r A_{dc} \gamma \eta_{shading} \rho \quad (3.8)$$

In Equation (3.8), γ is the intercept factor, $\eta_{shading}$ is the shading factor between different collectors, ρ is the reflectivity of the reflector.

(2) *Heat exchange between the HTF and the dish absorber, $q_{dr,1}$*

The heat transfer process between the HTF and the dish absorber is simplified to a heat exchange process of a flow in a uniform temperature heat pipe. So $q_{dr,1}$ can be written as

$$q_{dr,1} = h_{dr,1} A_{dr,1} \Delta T_{ln,dr,1} \quad (3.9)$$

where

$$h_{dr,1} = Nu_{tube} \lambda_{dr,1} / d_{i,1} \quad (3.10)$$

$$Nu_{tube} = c_r Nu'_{tube} \quad (3.11)$$

For helical spiral pipe, multiplier c_r based on curvature ratio can be expressed as^[106]

$$c_r = 1 + 3.5 \frac{d_{i,1}}{d_{cav} - d_{i,1} - 2\delta_a} \quad (3.12)$$

Nu'_{tube} is the Nusselt number of straight circular tube, which can be expressed by^[107]

$$Nu'_{tube} = 0.027 Re_{tube}^{0.8} Pr_{tube}^{1/3} (\mu_{tube} / \mu_{tube,w})^{0.14} \quad (3.13)$$

and the logarithmic mean temperature difference $\Delta T_{ln,dr,1}$ can be written as

$$\Delta T_{ln,dr,1} = \frac{(T_{cav} - T_{dc,i}) - (T_{cav} - T_{dc,o})}{\ln \frac{T_{cav} - T_{dc,i}}{T_{cav} - T_{dc,o}}} \quad (3.14)$$

(3) *Radiation losses reflected off the receiver, $q_{rad,ref}$*

$$q_{rad,ref} = (1 - \alpha_{eff}) q_i \quad (3.15)$$

where α_{eff} is the effective absorptivity of the receiver.

$$\alpha_{eff} = \frac{\alpha_{cav}}{\alpha_{cav} + (1 - \alpha_{cav}) \frac{A_{ap}}{A_{cav}}} \quad (3.16)$$

α_{cav} is the absorptivity of the cavity, A_{cav} is the cavity area, A_{ap} is the aperture area.

(4) *Conductive losses through the receiver insulating layer, $q_{cond,tot}$*

$$q_{cond,tot} = 2\pi\lambda_{insu}dep_{cav} \frac{T_{cav} - T_{insu}}{\ln(1 + 2\delta_{insu}/d_{cav})} \quad (3.17)$$

where T_{cav} is the temperature of the cavity wall, T_{insu} is outside temperature of the insulation wall.

(5) *Convection losses from the receiver insulating layer, $q_{cond,conv}$*

$$q_{cond,conv} = h_{insu}A_{insu}(T_{insu} - T_{amb}) = \frac{k_{insu}Nu_{insu}A_{insu}(T_{insu} - T_{amb})}{d_{cav} + 2\delta_{insu}} \quad (3.18)$$

where Nu_{insu} can be obtained from the correlation for flow over a circular cylinder.^[108]

(6) *Radiation losses from the receiver insulating layer, $q_{cond,rad}$*

$$q_{cond,rad} = \epsilon_{insu}A_{insu}\sigma(T_{insu}^4 - T_{amb}^4) \quad (3.19)$$

(7) *Free convection from the cavity in the absence of wind, $q_{conv,free}$*

Ma^[109] conducted tests to determine the free convection losses from the receiver for alternative setups, and the data were consistent with Stine and McDonald's free convection correlation. It is assumed that forced convection is independent of free convection in the receiver, so the total convection losses can be represented as the total of the free and forced convection losses as shown in Figure 3-4.

$$q_{conv,free} = h_{free}A_{cav}(T_{cav} - T_{amb}) \quad (3.20)$$

where $h_{free} = k_{film}Nu_{free}/\overline{d}_{cav}$, \overline{d}_{cav} is the effective diameter of the cavity, $\overline{d}_{cav} = d_{cav} - 2d_i - 4\delta_a$. $d_i = 0.066$ m

(8) *Force convection from the cavity in the presence of wind, $q_{conv,forc}$*

$$q_{conv,forc} = h_{forc}A_{cav}(T_{cav} - T_{amb}) \quad (3.21)$$

Wu et al.^[110] present a comprehensive review and systematic summarization of convection heat loss from cavity receiver in parabolic dish solar thermal power system. And we choose the correlation presented by Leibfried and Ortjohann^[111]. This correlation gives an extended model of Koenig and Marvin^[112] and Stine and Diver^[113] with better results.

For forced convection loss, side-on wind convection loss model given by Ma^[109], which is independent of the aperture orientation, is used

$$h_{forc} = 0.1967v_{wind}^{1.849} \quad (3.22)$$

(9) *Emission losses due to thermal radiation emitted from the receiver aperture*, $q_{rad,emit}$

The emissivity is set equal to the effective absorptivity of the cavity (gray body),

$$\epsilon_{cav} = \alpha_{eff} \quad (3.23)$$

$$q_{rad,emit} = \epsilon_{cav} A_{ap} \sigma (T_{cav}^4 - T_{amb}^4) \quad (3.24)$$

From Figure 3-4, it can be found that

$$q_{eff} = q_i - q_{rad,ref} \quad (3.25)$$

$$q_{eff} = q_{dr,1} + q_{cond,tot} + q_{conv,free} + q_{conv,forc} + q_{rad,emit} \quad (3.26)$$

$$q_{cond,tot} = q_{cond,conv} + q_{cond,rad} \quad (3.27)$$

So the temperature nodes in the thermal network can be solved by these equations.

$q_{dr,1}$ can be obtained from Equation (3.9), and efficiency of the dish receiver

$$\eta_{dr} = \frac{q_{dr,1}}{q_i} \quad (3.28)$$

Efficiency of the dish collector

$$\eta_{dc} = \frac{q_{dr,1}}{I_r A_{dc}} \quad (3.29)$$

3.1.3 Stirling engine

3.1.3.1 Theoretical Stirling cycle

In a Stirling cycle, there are two isothermal processes that exchange heat with heating and cooling fluids, two isochoric processes that exchange heat with regenerator. Figure 3-5 shows the $T-s$ diagram of a typical Stirling cycle. The heat absorbed by regenerator in process 4-1 is reused in process 2-3, but only able to heat the working gas from 2 to 3' due to the imperfect regeneration. e is defined as the regenerator effectiveness^[114,115], $e = \frac{T_R - T_L}{T_H - T_L}$, where T_H is the temperature in the hot space, T_L is the temperature in the cold space, T_R is the effective working fluid temperature in the regenerator.

In order to obtain a simplified analytical model, several simplifications are made:

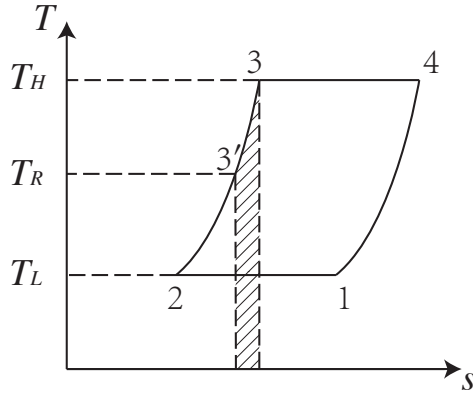


图 3-5 T - s diagram of a Stirling cycle

- The working gas in Stirling engines obeys the ideal gas law.
- No heat loss to the environment for Stirling engines.
- Overall heat transfer coefficients of the fluids are constant.
- A symmetrical regenerator behavior is assumed so that a simple effectiveness can be obtained by $T_R = \frac{T_H - T_L}{\ln(T_H/T_L)}$.^[114,115]

To consider internal irreversibilities in a Stirling cycle made by dead volumes, total dead volume V_D can be divided into heater dead volume V_{DH} , regenerator dead volume V_{DR} and cooler dead volume V_{DC} .^[116] There exists a factor K to describe the dead volumes under different temperatures. K is relevant with temperatures in the process and regenerator effectiveness.

$$K = \frac{V_{DH}}{T_H} + \frac{V_{DR}}{T_R} + \frac{V_{DC}}{T_L} \quad (3.30)$$

For the isothermal compression process 1-2, the output work

$$W_{12} = \int_{V_E+V_C}^{V_E} p_{12} dV = -mRT_L \ln \frac{V_E + V_C + KT_L}{V_E + KT_L} \quad (3.31)$$

For the isothermal expansion process 3-4, the output work

$$W_{34} = \int_{V_E}^{V_E+V_C} p_{34} dV = mRT_H \ln \frac{V_E + V_C + KT_H}{V_E + KT_H} \quad (3.32)$$

Define $\gamma_H = \frac{V_E + V_C + KT_H}{V_E + KT_H}$, and $\gamma_L = \frac{V_E + V_C + KT_L}{V_E + KT_L}$. In a cycle, the theoretical output work

$$W_{th} = W_{12} + W_{34} = mR(T_H \ln \gamma_H - T_L \ln \gamma_L) \quad (3.33)$$

For the isochoric heating process 3'-3, the absorbed heat

$$Q_{3'3} = nc_v(T_H - T_R) = \frac{1-e}{k-1}mR(T_H - T_L) \quad (3.35)$$

For the isothermal expansion process 3-4, the absorbed heat

$$Q_{34} = W_{34} = mRT_H \ln \gamma_H \quad (3.36)$$

In a cycle, the theoretical absorbed heat

$$Q_{th} = Q_{3'3} + Q_{34} = \frac{1-e}{k-1}mR(T_H - T_L) + mRT_H \ln \gamma_H \quad (3.37)$$

3.1.3.2 Irrevisibilities and losses

(1) Non-ideal heat transfer effect

Because of non-ideal heater and cooler, the working fluid temperature (T_H/T_L) in these two heat exchangers is less/higher than the wall temperature (T_{hw}/T_{cw}), respectively. T_H and T_L can be corrected by the wall temperatures as follows:

$$T_H = T_{hw} - \frac{Qs_{se}}{h_h A_{hw}} \quad (3.38)$$

$$T_L = T_{cw} + \frac{(Q-W)s_{se}}{h_c A_{cw}} \quad (3.39)$$

The heat transfer coefficient can be obtained using the following correlation^[1]:

$$h_{h,c} = \frac{\mu c_p f_{Re}}{2D_{h,c} Pr_{h,c}} \quad (3.40)$$

where f_{Re} is a Reynolds friction factor defined as:

$$f_{Re} = 0.0791 Re_{h,c}^{0.75} \quad (3.41)$$

$Re_{h,c}$, $Pr_{h,c}$ and $D_{h,c}$ are Reynolds number, Prandtl number and hydraulic diameter of the heater/cooler exchanger.

(2) Effect of pressure drop

Pressure drops in the heat exchangers cause power losses of the Stirling engine. The pressure drops can be expressed by:^[117]

$$\Delta p = -\frac{2f_{Re}\mu uV}{d^2 A} \quad (3.42)$$

where u is the working gas speed, V is volume, A is flow cross-section area.

The net power loss of the Stirling engine due to pressure drop of the heat exchangers can be evaluated by:

$$W_{pd} = \oint \sum_{i=E,C} (\Delta p_i \frac{dV_i}{d\theta}) d\theta \quad (3.43)$$

(3) Effect of finite speed of piston and mechanical friction

Due to the finite speed of piston, the pressure on the piston surface is different from the pressure of expansion and compression spaces. It has been demonstrated that the pressure on the piston surface in the expansion process is less than the mean pressure in the expansion space. Similarly, the pressure on the piston surface in the compression process is greater than the mean pressure in the compression space. This means the output work is less than the theoretical value. Besides, The output work also reduces due to mechanical friction. The output work loss due to finite speed of piston and mechanical friction can be obtained as follows:^[1]

$$W_{fs} = \oint p(\pm \frac{au_p}{c} \pm \frac{\Delta p_f}{p}) dV \quad (3.44)$$

where the sign (+) is used in the compression space, and the sign (-) is used in the expansion space. p is the mean pressure in the compression/expansion space, u_p is velocity of the piston, c is the average speed of molecules and Δp_f is the pressure loss due to mechanical friction. Δp_f , a and c can be expressed by:^[118]

$$\Delta p_f = 0.97 + 0.009s_{se} \quad (3.45)$$

$$a = \sqrt{3k} \quad (3.46)$$

$$c = \sqrt{3RT} \quad (3.47)$$

(4) Energy losses due to internal conduction

The temperature differs from the heater and cooler, heat losses from heater to cooler exists due to internal conduction through the walls of regenerator.^[119] The internal conduction loss in a cycle can be expressed by follows:

$$Q_{id} = \frac{k_r A_r}{L_r s_{se}} (T_{hw} - T_{cw}) \quad (3.48)$$

where, k_r , A_r and L_r denote the regenerator matrix conductivity, regenerator length, and regenerator conductive area respectively.

(5) Energy losses due to shuttle conduction

The displacer shuttles between the expansion and compression space. It absorbs heat during the hot end of its stroke and releases it during the cold end of its stroke. This heat loss can be estimated as^[120]:

$$Q_{sc} = 0.4 \frac{Z^2 k_p D_p}{J L_d s_{se}} (T_H - T_L) \quad (3.49)$$

where, Z , k_p , D_p , J and L_d denote the displacer stroke, piston thermal conductivity, displacer diameter, gap between the displacer and the cylinder, and length of the displacer respectively.

So, in a Stirling engine, the total absorbed heat in a cycle

$$Q = Q_{th} + Q_{id} + Q_{sc} \quad (3.50)$$

the output work

$$W = W_{th} - W_{pd} - W_{fs} \quad (3.51)$$

Power of the Stirling engine

$$P = W s_{se} \quad (3.52)$$

Efficiency of the Stirling engine

$$\eta = W/Q \quad (3.53)$$

3.1.3.3 Model validation

Evaluation of the developed thermal model is performed by considering the GPU-3 Stirling engine as a case study. Design specifications of the GPU-3 Stirling engine are indicated

表 3.2 Design specifications of the GPU-3 Stirling engine^[1,2]

Parameter	Value
Engine type	β
Working gas	Helium
Mass of the working gas	1.136 g
<i>Heater</i>	
Number of tubes	40
Tube external diameter	4.83×10^{-3} m
Tube internal diameter	3.02×10^{-3} m
Tube length (cylinder side)	0.1164 m
Tube length (regenerator side)	0.1289 m
<i>Cooler</i>	
Number of tubes	312
Tube external diameter	1.59×10^{-3} m
Tube internal diameter	1.09×10^{-3} m
Average tube length	4.61×10^{-2} m
<i>Regenerator</i>	
Number of regenerator	8
Regenerator internal diameter	2.26×10^{-2} m
Regenerator length	2.26×10^{-2} m
Diameter of regenerator tube	4×10^{-5} m
Material	Stainless steel
<i>Volume</i>	
Swept Vol. (expansion/compression)	120.82/114.13 cm ³
Clearance Vol. (expansion/compression)	30.52/28.68 cm ³
Dead Vol. (heater/cooler/regenerator)	70.28/13.18/50.55 cm ³

表 3.3 Thermal efficiency of the models and experimental data (at $T_{hw} = 922\text{ K}$ and $T_{cw} = 288\text{ K}$)

Rotation speed (Hz)	Mean effective pressure (MPa)	The simple analysis (variable Pr ^[117])			The adiabatic analysis (simple II ^[119])			The proposed Stirling engine model			Experimental efficiency ^[1]
		Value (%)	Error (%)	Average error (%)	Value (%)	Error (%)	Average error (%)	Value (%)	Error (%)	Average error (%)	
16.67	38.72	18.22		32.48	11.98		28.16	7.66		20.50	
25.00	36.16	15.46		31.21	10.51		27.75	7.05		20.70	
33.33	33.79	15.79		29.45	11.45		27.43	9.43		18.00	
41.67	31.48	16.28		27.45	12.25		27.17	11.97		15.20	
50.00	29.12	17.32		25.21	13.41		26.94	15.14		11.80	
58.33	29.74	24.34		22.89	17.49		26.74	21.34		5.40	
25.00	35.65	10.85		32.29	7.49		27.29	2.49		24.80	
33.33	33.52	9.62		30.40	6.50		26.94	3.04		23.90	
41.67	4.14	31.48	10.18	11.46	28.39	7.09	8.28	26.65	5.35	6.65	21.30
50.00	29.45	11.25		26.33	8.13		26.39	8.19		18.20	
58.33	27.40	15.40		24.21	12.21		26.17	14.17		12.00	
41.67	31.20	8.70		28.59	6.09		26.24	3.74		22.50	
50.00	5.52	29.33	10.53	10.82	26.62	7.82	8.11	25.97	7.17	7.48	18.80
58.33	27.44	13.24		24.62	10.42		25.73	11.53		14.20	
50.00	6.90	29.07	10.37	11.73	24.67	10.47	9.19	25.62	6.92	9.05	18.70
58.33	27.29	13.09					25.37	11.17		14.20	

表 3.4 Output power of the models and experimental data (at $T_{hw} = 922\text{ K}$ and $T_{cw} = 288\text{ K}$)

Rotation speed (Hz)	Mean effective pressure (MPa)	The simple analysis			The adiabatic analysis (simple II ^[119])			The proposed Stirling engine model			Experiment (kW) ^[1]
		Value (kW)	Error (%)	Average error (%)	Value (kW)	Error (%)	Average error (%)	Value (kW)	Error (%)	Average error (%)	
16.67	1.796	119.02	1.772	116.10	0.861	4.98	0.82	0.82	4.98	0.82	0.82
25.00	2.555	128.13	2.500	123.21	1.253	11.88	1.12	1.12	11.88	1.12	1.12
33.33	3.215	165.70	3.117	157.60	1.632	34.88	1.21	1.21	34.88	1.21	1.21
41.67	2.76	3.769	272.03	3.615	254.71	2.001	65.37	104.84	2.001	65.37	104.84
50.00	4.195	303.37	3.973	282.08	2.362	127.12	1.04	1.04	127.12	1.04	1.04
58.33	4.505	704.46	4.203	650.54	2.715	384.82	0.56	0.56	384.82	0.56	0.56
25.00	3.844	114.75	3.761	110.11	1.818	1.56	1.79	1.79	1.56	1.79	1.79
33.33	4.856	120.73	4.708	114.00	2.362	7.36	2.20	2.20	7.36	2.20	2.20
41.67	4.14	5.734	136.94	259.70	5.501	127.31	158.41	2.890	19.42	39.83	2.42
50.00	6.462	174.98	6.126	160.68	3.405	44.89	2.35	2.35	44.89	2.35	2.35
58.33	7.030	306.36	6.573	279.94	3.908	125.90	1.73	1.73	125.90	1.73	1.73
41.67	7.645	133.08	7.334	123.60	3.742	14.09	3.28	3.28	14.09	3.28	3.28
50.00	5.52	8.655	163.87	180.02	8.206	150.18	4.401	34.18	43.68	3.28	3.28
58.33	9.470	243.12	8.858	220.94	5.045	82.79	2.76	2.76	82.79	2.76	2.76
50.00	10.788	174.50	10.223	160.13	5.362	36.44	3.93	3.93	36.44	3.93	3.93
58.33	6.90	11.840	399.58	287.04	11.071	367.13	2.37	2.37	367.13	2.37	2.37

in Table 3.2. The thermal efficiency and power of the proposed Stirling engine model are compared with previous thermal models and experimental data as shown in Table 3.3 and Table 3.4.

It can be found that the proposed model has much better agreement with the experimental results than previous thermal models at various rotation speeds and mean effective pressures. It is required to mention that in all thermal models both power W and input heat Q are determined by the thermal process of heat transfer between the wall and working gas. In the proposed model, W and Q are obtained from Equation (3.38) and (3.39). Therefore all the three parameters W , Q and η are determined by the thermal model and input parameters to the model. These input parameters includes heater, cooler, mean effective pressure, type of working gas and geometrical specification of the engine.

Table 3.3 and 3.4 indicate that when mean effective pressure of the engine increases from 2.76 MPa to 6.90 MPa, best performance (efficiency and power) prediction of the proposed model exists. When rotation speed increases from 16.67 Hz to 58.33 Hz, error in prediction of performance of the proposed model increases. The proposed model may have the best performance prediction at a low rotation speed, with mean effective pressure between 4.14 MPa and 5.52 MPa.

However, there is still some discrepancy between the simulation results of proposed model and the experimental data. In the future researches, more accurate models of Stirling engine may be developed by considering other irreversibilities such as heat loss to the environment, gas spring hysteresis, and etc. It is worth pointing that there are more accurate Stirling engine models. For example, polytropic simulation models of Stirling engine show higher accuracy than our proposed model^[1,121]. However, the model needs more costly calculations and the polytropic indexes are engine-specific.

3.1.3.4 Heat transfer between the engine and the fluids

For a Stirling engine thermal process, the wall temperatures of the heater and cooler are considered to be uniform and constant. The heat transferred between the wall and the fluids after a contact area of dA is

$$(T_w - T)UdA = \dot{m}c_p dT \quad (3.54)$$

$$\frac{dT}{T - T_w} = -\frac{UdA}{\dot{m}c_p} \quad (3.55)$$

With $T(0) = T_i$, $T(A) = T_o$,

$$\frac{T_o - T_w}{T_i - T_w} = \exp\left(-\frac{UA}{\dot{m}c_p}\right) \quad (3.56)$$

For a Stirling engine, T_{hw} or T_{cw} can be used to substitute T_w to get the relationships between $T_{i,h}$, $T_{o,h}$ and T_{hw} , or $T_{i,c}$, $T_{o,c}$ and T_{cw} respectively.

$$\frac{T_{o,h} - T_{hw}}{T_{i,h} - T_{hw}} = \exp\left(-\frac{U_h A_h}{\dot{m}_h c_{p,h}}\right) \quad (3.57)$$

$$\frac{T_{o,c} - T_{cw}}{T_{i,c} - T_{cw}} = \exp\left(-\frac{U_c A_c}{\dot{m}_c c_{p,c}}\right) \quad (3.58)$$

Heat transferred from heating fluid to Stirling engine in a cycle

$$\dot{m}_h c_{p,h} (T_{i,h} - T_{o,h}) / s_{se} = Q \quad (3.59)$$

Heat transferred from Stirling engine to cooling fluid in a cycle

$$\dot{m}_c c_{p,c} (T_{o,c} - T_{i,c}) / s_{se} = Q - W \quad (3.60)$$

3.1.4 Rankine power generation system

Based on different working fluids, there are two different kinds of Rankine power generation systems, steam Rankine power generation system and organic Rankine power generation.

3.1.4.1 Steam Rankine cycle

For steam Rankine cycle, a deaerator is used to remove the oxygen and other non-condensable gases in the feedwater of steam generating system. Dissolved oxygen in feedwater will cause serious corrosion damage in steam generating system by forming oxides (rust) of the metal pipes. Dissolved carbon dioxide combines with water to form carbonic acid will cause further corrosion. The accumulation of the non-condensable gases will increase

the heat transfer resistance, which is harmful for the heat exchangers. The extraction of the steam turbine provides heat for the deaerator.

Figure 3-6a shows the $T-s$ diagram of the water circuit in the cascade system in Figure 3-11. Process 2a-2c-2b shows the heat process in the steam turbine (see Figure 3-6b). State point 2b and $i, 2b$ have the same pressure, state point 2c and $i, 2c$ have the same pressure. To simplify the inner process 2a-2c-2b of the turbine, same isentropic efficiency of steam turbine with different loads and in different stages is assumed, which means

$$\eta_{i,tb} = (h_{2a} - h_{2b})/(h_{2a} - h_{i,2b}) = (h_{2a} - h_{2c})/(h_{2a} - h_{i,2c}) \quad (3.61)$$

where $h_{i,2b}$ is determined by s_{2a} and p_c ; $h_{i,2c}$ is determined by s_{2a} and p_e .

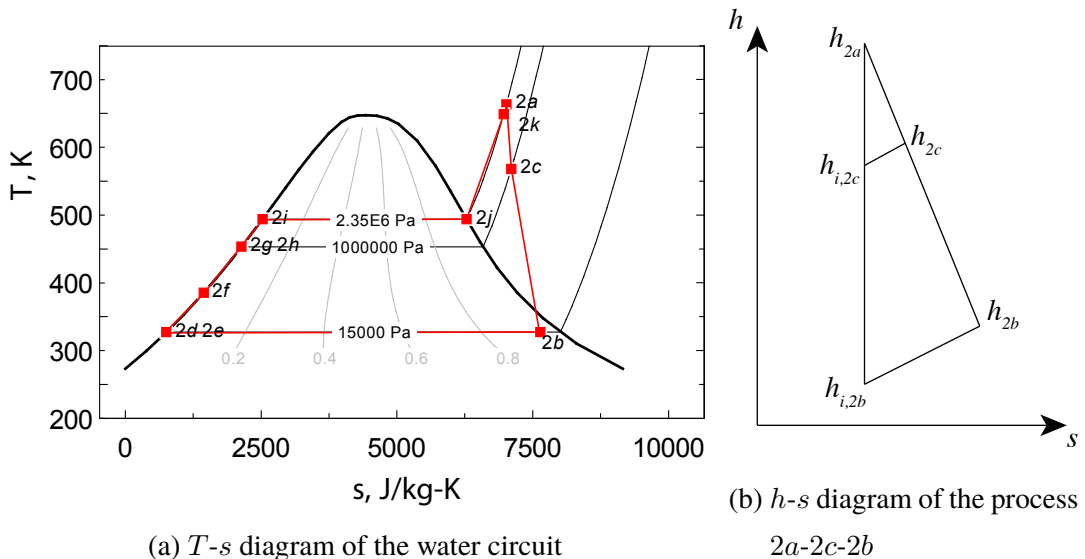


图 3-6 $T-s$ diagram of the water circuit and $h-s$ diagram of the process 2a-2b

The output power of the steam turbine

$$P_{tb} = (1 - y) \dot{m}_2 (h_{2a} - h_{2b}) + y \dot{m}_2 (h_{2a} - h_{2c}) \quad (3.62)$$

Process 2b-2d shows the heat process in the condenser. The outlet water in the condenser is saturated water. The outlet temperature T_{2d} and outlet enthalpy h_{2d} are determined by the exhaust pressure of the turbine p_c . The released heat of the condenser

$$Q_{cd} = (1 - y) \dot{m}_2 (h_{2b} - h_{2d}) \quad (3.63)$$

State points $2c$, $2f$ and $2g$ have the same pressure (p_e , 1 MPa). The water at the outlet of the deaerator is saturated fluid, its enthalpy is determined.

$$yh_{2c} + (1 - y)h_{2f} = h_{2g} \quad (3.64)$$

The total power of the pumps

$$P_{pu} = (1 - y)\dot{m}_2(h_{2e} - h_{2d}) + \dot{m}_2(h_{2h} - h_{2g}) \quad (3.65)$$

where h_{2e} can be obtained from $\eta_{pu} = (h_{i,2e} - h_{2d})/(h_{2e} - h_{2d})$, h_{2h} can be obtained from $\eta_{pu} = (h_{i,2h} - h_{2g})/(h_{2h} - h_{2g})$. $h_{i,2e}$ is determined by s_{2d} and p_e , $h_{i,2h}$ is determined by s_{2g} and p_s .

The outlet water of the deaerator is saturated water ($x = 0$), so the outlet temperature T_{2g} and outlet enthalpy h_{2g} of the heated fluid is determined by pressure p_{2g} . For the deaerator, the outlet pressure equals to any of the inlet pressure.

$$p_{2g} = p_{2c} \quad (3.66)$$

Heat injected in the water circuit

$$Q_2 = (1 - y)\dot{m}_2(h_{2f} - h_{2e}) + \dot{m}_2(h_{2a} - h_{2h}) \quad (3.67)$$

The efficiency of Rankine cycle can be expressed as

$$\eta_{rk} = (P_{tb} - P_{pu}/\eta_{ge})/Q_2 \quad (3.68)$$

3.1.4.2 Organic Rankine cycle

Compared with steam Rankine cycle, ORC has the following features:

- (1) Organic fluid has lower boiling point, and higher evaporation pressure. It is suitable for the recovery of low temperature waste heat. Besides, it has small density and specific heat capacity, the required size of turbine, pipes and heat transfer areas are small, which is beneficial for cost saving.
- (2) The exhaust fluid of the turbine is dry. So without overheating, the saturated gas can be used as the main gas for the turbine. The corrosion situation caused by the impact of the droplets to the high-speed rotating blades will not happen with ORC.

- (3) Organic fluid has lower sound speed than vapor, the turbine can achieve favorable aerodynamic performance with lower wheel speed.
- (4) Organic fluid has higher condensing pressure than water. It can condense under the pressure higher than the atmosphere. The system pressure can be maintained above the atmosphere pressure to prevent air leak into the system. This means a deaerator is no more necessary.
- (5) Organic fluid has low freezing point, no anti-freezing treatment is required even in the cold area.

The shapes of curves in the $T-s$ diagram of different fluids are different. According to the saturated vapor curve dT/ds in the $T-s$ diagram, the working fluid can be divided into three types: $dT/ds > 0$ means dry fluid (moisture does not form when high-pressure saturated vapor expanded reversibly from a high pressure), most of the organic fluid are dry fluids; $dT/ds < 0$ means wet fluid (moisture forms when high-pressure saturated vapor expanded reversibly from a high pressure), such as water; $dT/ds \rightarrow \pm\infty$ means isentropic fluid, such as R134a. For the high temperature high pressure dry fluid and isentropic fluid, since there is no droplets after work in the expansion turbine, no superheater is required. On the other hand, since the purpose of the ORC focuses on the recovery of low grade heat power, a superheated approach like the traditional Rankine cycle is not appropriate.

Figure 3-7 shows the $T-s$ diagram of steam Rankine cycle and ORC cycle. Figure 3-8 shows the schematic diagram of the ORC system. For a dry fluid, the cycle can be improved by the use of a regenerator: since the fluid has not reached the two-phase state at the end of the expansion, its temperature at this point is higher than the condensing temperature. This higher temperature fluid can be used to preheat the liquid before it enters the evaporator. A counter-current heat exchanger is thus installed between the expander outlet and the evaporator inlet. The power required from the heat source is therefore reduced and the efficiency is increased.

The isentropic efficiency of the turbine

$$\eta_{i,tb} = (h_{4a} - h_{4b}) / (h_{4a} - h_{i,4b}) \quad (3.69)$$

where $h_{i,4b}$ is determined by s_{4a} and p_c .

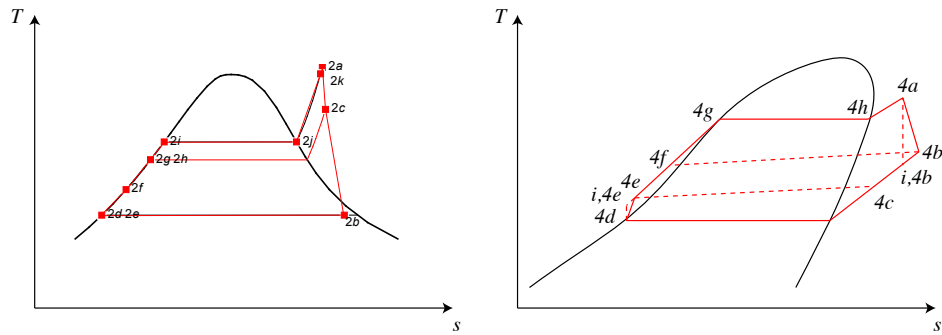


图 3-7 $T-s$ diagram of water and a typical organic fluid in Rankine cycles

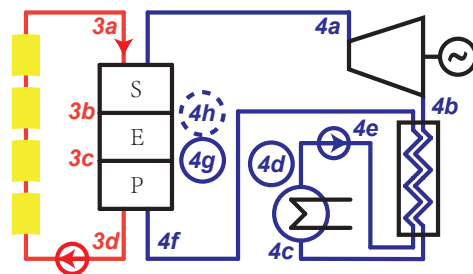


图 3-8 The schematic diagram of an ORC system with regenerator

The output power of the turbine

$$P_{tb} = \dot{m}_4(h_{4a} - h_{4b}) \quad (3.70)$$

Process 4c-4d shows the heat process in the condenser. The outlet fluid of the condenser is saturated liquid. The outlet temperature T_{4d} and outlet enthalpy h_{4d} are determined by the exhaust pressure of the turbine p_c .

For the regenerator,

$$h_{4b} - h_{4c} = h_{4f} - h_{4e} \quad (3.71)$$

The released heat of the condenser

$$Q_{cd} = \dot{m}_4(h_{4c} - h_{4d}) \quad (3.72)$$

The power of the pump

$$P_{pu} = \dot{m}_4(h_{4e} - h_{4d}) \quad (3.73)$$

where h_{4e} can be obtained from $\eta_{pu} = (h_{i,4e} - h_{4d})/(h_{4e} - h_{4d})$. $h_{i,4e}$ is determined by s_{4d} and p_s .

Heat injected in the circuit

$$Q_4 = \dot{m}_4(h_{4a} - h_{4f}) \quad (3.74)$$

The efficiency of Rankine cycle can be expressed as

$$\eta_{rk} = \frac{P_{tb} - P_{pu}/\eta_{ge}}{\dot{m}_4(h_{4a} - h_{4f})} \quad (3.75)$$

3.1.4.3 Generator

The generator is relatively independent of the cascade system and its efficiency is assumed to be a constant value, 0.975.

3.2 Stirling engine array modeling

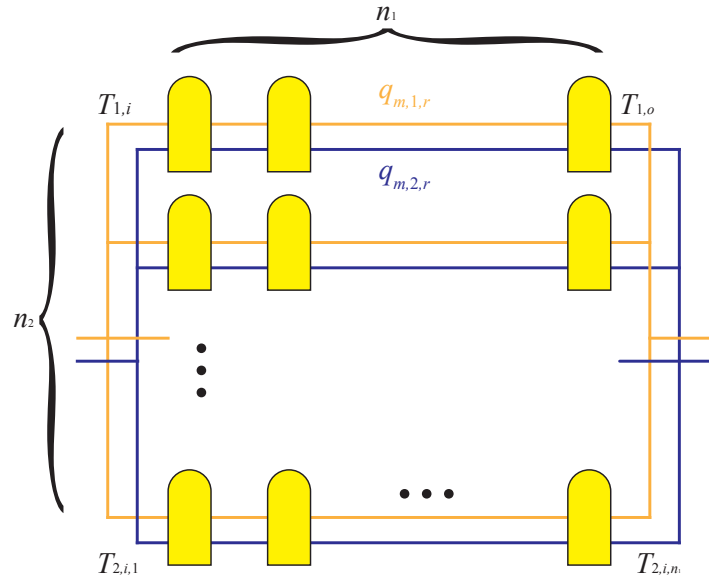


图 3-9 Layout of Stirling engines

Stirling engine array is used in the cascade system, Figure 3-9 shows the layout of a Stirling engine array. Each Stirling engine in the Stirling engine array has the identical parameters: $U_{se,1} = 30 \text{ W}/(\text{m}^2 \cdot \text{K})$, $U_{se,2} = 150 \text{ W}/(\text{m}^2 \cdot \text{K})$, $A_{se,1} = 6 \text{ m}^2$, $A_{se,2} = 6 \text{ m}^2$, $k_{se} = 1.4$, $\gamma_{se} = 3.375$, $n_g = 7.84 \times 10^{-2} \text{ mol}$, $s_{se} = 10 \text{ s}^{-1}$.

Depending on the direction of heating and cooling flows, there are two possible flow types: parallel flow and counterflow. Figure 3-10 and Figure 3-10b show the heat transfer diagrams of the two flow types. n_1 is chosen to be 10 and can be optimized later.

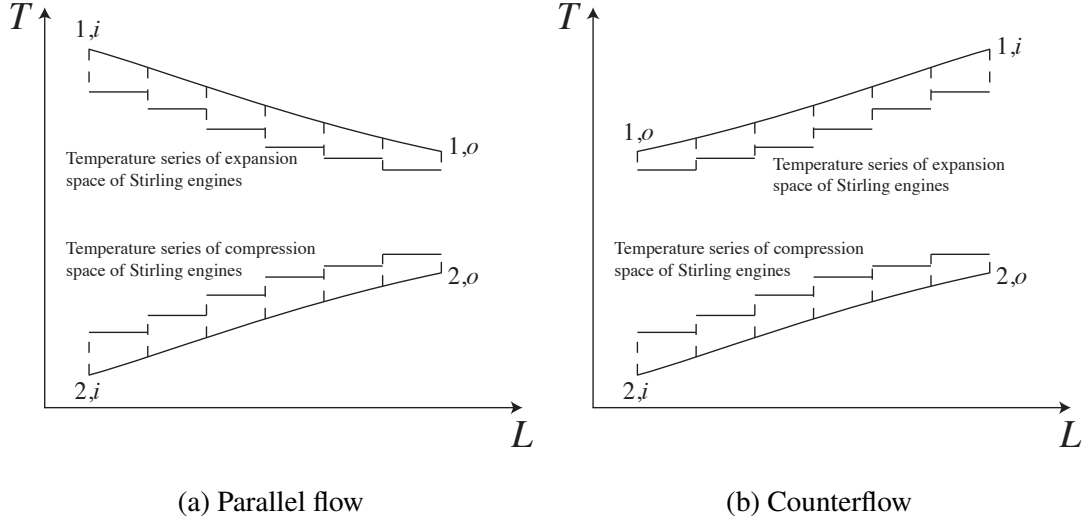


图 3-10 Heat transfer diagrams of parallel flow and counterflow

In Figure 3-9, $T_{1,i,1} = T_{1,i}$, $\dot{m}_{1,r} = \dot{m}_1/n_2$. For x from 1 to $n_1 - 1$, where x is the column number of Stirling engines, $T_{1,i,x+1} = T_{1,o,x}$, $T_{2,i,x+1} = T_{2,o,x}$.

Assume that the positive flow direction is to the right, for parallel flow, $T_{2,i,1} = T_{2,i}$, $\dot{m}_{2,r} = \dot{m}_2/n_2$; for counterflow, $T_{2,o,n_1} = T_{2,i}$, $\dot{m}_{2,r} = -\dot{m}_2/n_2$.

Assume linear temperature profile across the regenerator, the mean effective temperature $T_{R,x} = \frac{T_{H,x} - T_{L,x}}{\ln(T_{H,x}/T_{L,x})}$ ^[122,123] and the symmetrical regenerator behaviour assumption $e_x = \frac{T_{R,x} - T_{L,x}}{T_{H,x} - T_{L,x}}$ ^[114,115]

For a Stirling engine in column x , x from 1 to n_1 , according to Equation (3.38) and Equation (3.39),

$$T_{hw,x} = T_{1,i,x} - \frac{T_{1,i,x} - T_{1,o,x}}{1 - \exp(-\frac{U_{se,1}A_{se,1}}{\dot{m}_{1,r}c_{p,1,x}})} \quad (3.76)$$

$$T_{cw,x} = T_{2,i,x} - \frac{T_{2,i,x} - T_{2,o,x}}{1 - \exp(-\frac{U_{se,2}A_{se,2}}{\dot{m}_{2,r}c_{p,2,x}})} \quad (3.77)$$

The power of each Stirling engine in column x can be written as

$$P_{se,x} = W_{th,x} - W_{pd,x} - W_{fs,x} \quad (3.78)$$

The efficiency of each Stirling engine in column x can be written as

$$\eta_{se,x} = \frac{W_{th,x} - W_{pd,x} - W_{fs,x}}{Q_{th,x} + Q_{id,x} + Q_{sc,x}} \quad (3.79)$$

For energy balance,

$$\dot{m}_{1,r}(h_{1,i,x} - h_{1,o,x})(1 - \eta_{se,x}) = \dot{m}_{2,r}(h_{2,o,x} - h_{2,i,x}) \quad (3.80)$$

Using equations in Section 3.1.3 and the energy balance equations, key parameters of the Stirling engine array can be obtained.

The efficiency of the Stirling engine array

$$\eta_{sea} = 1 - \frac{\dot{m}_2(h_{2,o,n_1} - h_{2,i,1})}{\dot{m}_1(h_{1,i,1} - h_{1,o,n_1})} \quad (3.81)$$

The output power of each Stirling engine in column x

$$P_{se,x} = \dot{m}_{1,r}(h_{1,i,x} - h_{1,o,x})\eta_{se,x} \quad (3.82)$$

The total output power of the Stirling engine array

$$P_{sea} = \eta_{sea}\dot{m}_1(h_{1,i,1} - h_{1,o,n_1}) \quad (3.83)$$

3.3 Steam generating system modeling

The steam generating system can be divided into preheater, evaporator and superheater, they are collectively referred to as PES. They are all heat exchangers. It is assumed that, in these heat exchangers, the pressure of the fluid does not change significantly. It can be assumed that the water pressure in the steam generating system equals to the pressure of the inlet pressure of the turbine. Besides, these heat exchangers do not exchange heat with the environment. To clearly understand the modeling process of these heat exchangers, an example of steam generating system as shown in Figure 3-11 is used for explanation. Figure 3-12 shows the $T-Q$ diagram of the heat transfer process. State points of different fluids are marked on the sketch. The number indicates the type of the fluid, the letter indicates the

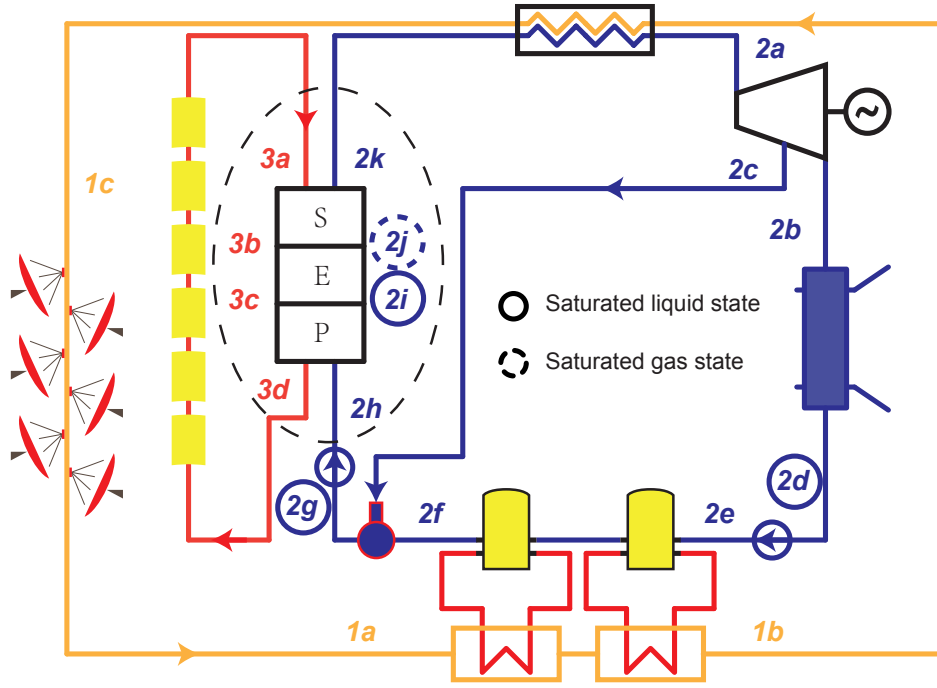


图 3-11 An example of steam generating system in a cascade system

state point of the fluid. A state point with solid circle indicates saturated liquid state ($x = 0$), and with dotted circle indicates saturated gas state ($x = 1$).

The modeling process of PES is the process of solving the unknown states of the state points. Notice that, the pressure of the fluids keeps constant in the heat transfer process. For an unsaturated state, known the temperature or enthalpy, the state is determined. This means, the temperature can be obtained from the enthalpy, and vice versa. For a saturated state, known the dryness (x) of the fluid, the state is determined.

For a typical PES modeling process as shown in Figure 3-11, \dot{m}_2 , state $2h$ and state $2k$ are determined by the parameters of the turbine. State $3a$ is determined by the design parameters. State $2i$ and state $2j$ are determined by their dryness values.

(1) Preheater

The outlet of the heated fluid is saturated liquid ($x = 0$), so the outlet temperature T_{2i} and outlet enthalpy h_{2i} of the heated fluid are determined by the main pressure of the

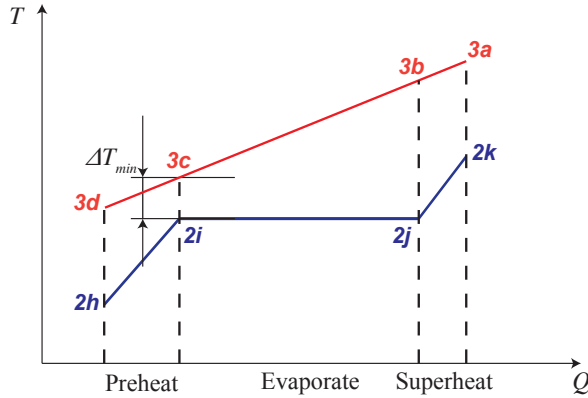


图 3-12 The steam generating process

turbine, p_s .

$$\dot{m}_3(h_{3c} - h_{3d}) = \dot{m}_2(h_{2i} - h_{2h}) \quad (3.84)$$

(2) Evaporator

The outlet of the heated fluid is saturated gas ($x = 1$), so the outlet temperature T_{2j} and outlet enthalpy h_{2j} of the heated fluid are determined by the main pressure of the turbine, p_s .

$$\dot{m}_3(h_{3b} - h_{3c}) = \dot{m}_2(h_{2j} - h_{2i}) \quad (3.85)$$

It has to be mentioned that, state $3c$ is determined by T_{3c} , which equals to $T_{2i} + \Delta T_{min}$.

$$(T_{3c} = T_{2i} + \Delta T_{min})$$

(3) Superheater

For the energy balance,

$$\dot{m}_3(h_{3a} - h_{3b}) = \dot{m}_2(h_{2k} - h_{2j}) \quad (3.86)$$

By solving the equations (3.84) to (3.86), \dot{m}_3 , state $3b$ and $3d$ can be obtained.

3.4 System modeling

Different components are connected to form a system by their interfaces (inlets and outlets). These interfaces are interacted with each other by "streams". For example, the steam turbine in Figure 3-11 is connected with the deaerator by a steam stream. This steam stream has its own properties such as fluid type, mass flow rate, temperature, pressure and

so on. "Streams" are defined as objects in the modeling language – MATLAB. Appendix C shows the source code of the definition of the class – **Stream**.

Some properties, **T**, **q_m** and **p**, of **Stream** are also objects. They belong to the classes **Temperature**, **Massflow** and **Pressure** separately.

Given the inherent properties of a **Stream**, its dependent properties, mass specific enthalpy (**h**), mass specific entropy (**s**) and pressure (**p**), can be obtained.

If the stream is a single phase stream, its dryness does not exist. Its dependent properties (h, s, c_p) can be obtained from its temperature (T) and pressure (p) by calling the open source MATALB wrapper CoolProp. If the stream is a two-phase stream, $0 \leq x \leq 1$. Its dependent properties (h, s, c_p) can be obtained from its pressure (p) and dryness (x). The reason of choosing pressure (p) instead of temperature (T) as the input value is that it is easier to be determined.

A **stream** can be used to record a state point since it contains all the information for a state point. Streams are defined in a system for component connection and system calculation. Different components are connected by streams to form a system. The Streams are passed as parameters to the components, completing the calculation of the methods in the components.

Components are connected each other by streams. Their inlets and outlets are used as interfaces for connection. Two interfaces are connected together by being assigned the same stream.

Systems are initialized by given parameters (design parameters). These parameters are assigned to corresponding properties of the streams and thus affect the state of the related components.

For system calculation, it has to be mentioned that, some parameters of a component are related with other components. In such situations, guess values are used for the calculation methods in the components. The guess values are set to be the properties of some streams. Each of these streams is assigned to two components (evaporator and superheater). These streams are assigned to corresponding components to accomplish the calculation methods in the components. These calculation methods will return solutions for the stream parameters. Then the parameters will be compared with the guess values for verification. If the differences between guess values and the calculated parameters are within permissible error, the guess values are accepted; otherwise, the guess values will be iteratively readjusted according to the Runge-Kutta method until accepted.

For example, the mass flow rate of oil of the evaporator (\dot{m}_3) is related with the superheater in a system as described in Figure 2-18a. A guess value of \dot{m}_3 , $\dot{m}_{3,g}$, is required to determine it. $\dot{m}_{3,g}$ is assigned to the evaporator oil stream. This stream is assigned to both evaporator and superheater. In **evaporator**, the method **get_T_3b** will change the temperature of the stream (T_{3b}) from the default value. In **superheater**, the method **get_q_m_3** will return a solution of \dot{m}_3 , $\dot{m}_{3,s}$, for verification. If $|\dot{m}_{3,g} - \dot{m}_{3,s}|$ is less than permissible error (10^{-4}), then $\dot{m}_{3,g}$ is accepted as the value of \dot{m}_3 ; otherwise, $\dot{m}_{3,g}$ will be iteratively readjusted according to the Runge-Kutta method until $|\dot{m}_{3,g} - \dot{m}_{3,s}| < 10^{-4}$.

3.5 Conclusion

This chapter presents the modeling method of the cascade system and introduces the modeling of some key components and subsystems in detail. The component models are developed in MATLAB using object-oriented method. Bottom-up design method is applied for system development. Models of the components of a system are developed first according to their mechanism characteristics, and the system model is established by these component models. A MATLAB class **Stream** created for component connection is used as an example to introduce the system modeling process. The components' inlets and outlets are used as interfaces for connection. Two interfaces are connected together by being assigned the same stream. The calculation process related with different components is also briefly introduced in this chapter.

Due to the encapsulation, composition and polymorphism of the object-oriented language, the system model has some advantages such as easy to establish, convenient to replace a component and clearly check the performance of specific components.

The key component models in the cascade system can be validated experimentally or be compared with the classic models. The validation of Stirling engine model shows that the proposed model has much better agreement with the experimental results than previous classic thermal models at various rotation speeds and mean effective pressures.

四 Optimization of Stirling engine array

4.1 Connection types of SEA

For a single Stirling engine, the heat transfer processes between fluids and engine are independent and irrelevant with the directions of the flows, which means the efficiency and power are not affected by the direction of fluids. However, for an SEA, the connection type will affect the temperature profiles through the array and the specific work production, both of which will determine the efficiency and power of the SEA. It is practically significant to investigate the influence of connection type of an SEA on its performance. Using parallel flow, on the one hand, will reduce the flow rate of the fluid, which will reduce the power of each engine; however, on the other hand, will take the advantage of higher inlet heating fluid temperature (or lower inlet cooling fluid temperature), which may increase the power of each engine. Using serial flow, on the one hand, will increase the flow rate of the fluid, which will increase the power of each engine; however, on the other hand, the inlet heating fluid temperature reduces with the flow direction (or the inlet cooling fluid temperature increases with the flow direction), which leads to lower engine power along the flow direction. Using the same order will lead to largest fluid temperature difference (temperature difference of the heating and cooling fluids) at the first engines and smallest fluid temperature difference at the last engines. Using the reverse order will lead to more averaged fluid temperature differences of each engine. For a heat exchanger, the reverse order (counterflow), which leads to a smaller fluid temperature difference, has a better heat transfer effect for its lower exergy loss. However, for a Stirling engine, the smaller fluid temperature difference leads to lower performance due to the lower temperature difference of the working gas in the hot space and cold space. To find out the influence of connection types on the performance of SEA, it is essential to classify the connection types.

Five basic connection types of SEA are summarized according to the direction-irrelevant feature of Stirling engine, as shown in Figure 4-1. Type 1 is parallel flow, Type 2 is serial flows in the same order, Type 3 is serial flows in the reverse order, Type 4 is heating fluid in serial flow and cooling fluid in parallel flow and Type 5 is heating fluid in parallel flow and cooling fluid in serial flow. All other connection types are the combination of these five

basic connection types. For instance, an SEA in Figure 4-2 is the combination of Type 2 and Type 4.

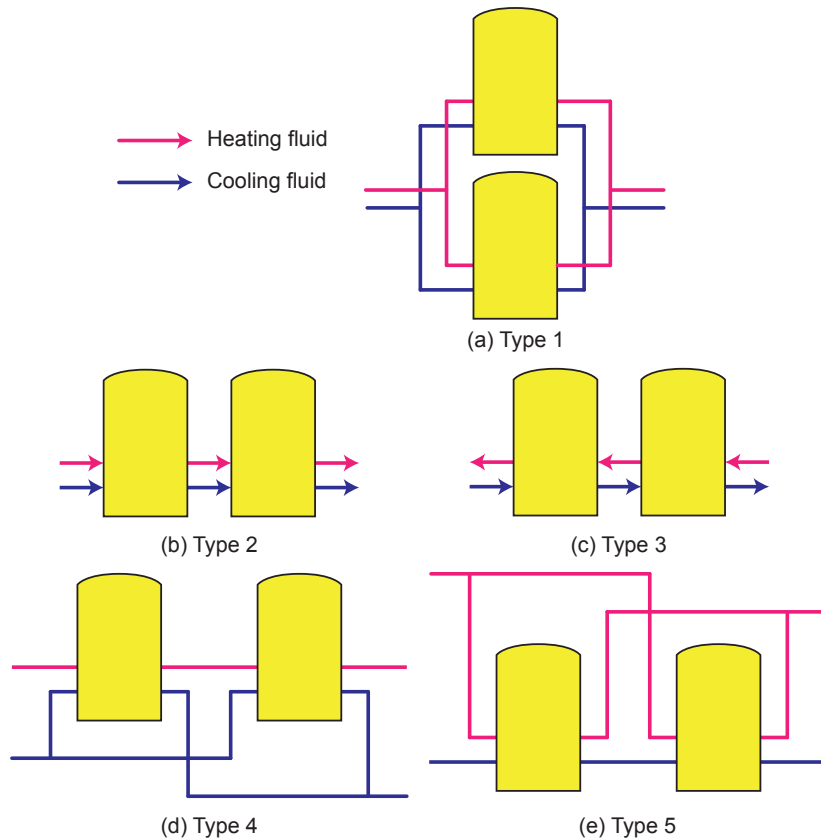


图 4-1 Five basic connection types of SEA

4.2 Modeling of the SEAs

As mentioned in Section 4.1, there are five basic connection types for an SEA. All other connection types are the combination of these five basic connection types. This thesis investigates the five basic connection types.

To determine the performance of an SEA, models of all the Stirling engines need to be built depending on their thermodynamic characteristic. Stirling engines are chosen to have

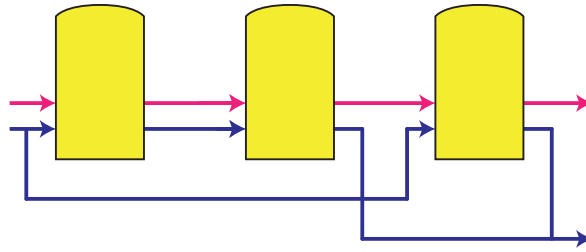


图 4-2 An instance of connection type of an SEA

the same parameters including the same speed s_{se} . This is a reasonable assumption when using SEA for power generation, where the output power frequency should be constant. The speed of Stirling engine can be calibrated by speed controller system^[124]. To eliminate interference of other factors, heating and cooling fluids are chosen to have same parameters for different connection types of SEAs. To clearly find out the performance differences of different SEAs, large temperature differences of the heating/cooling fluids after heat exchange with the engines are preferred. Air is chosen as the cooling fluid instead of commonly used water to avoid small temperature rise and evaporation in the cooling process. Design parameters of Stirling engines are the same as shown in Table 3.2. Other parameters of Stirling engines and heating/cooling fluids in SEAs are shown in Table 4.1. Rotation speed of the engines and mean effective pressure are chosen to be 25 Hz and 5 MPa respectively to get the best Stirling engine model for performance prediction, as pointed in Section 3.1.3.3.

In an SEA, there are 2 flows as shown in Figure 4-1. In a serial flow, each engine's mass flow rate is \dot{m} , and from the flow's direction, for $2 \leq x \leq n_{se}$,

$$T_{i,x} = T_{o,x-1} \quad (4.1)$$

In a parallel flow, each engine's mass flow is \dot{m}/n_{se} , for $2 \leq x \leq n_{se}$,

$$T_{i,x} = T_{i,h} \quad (4.2)$$

According to the equations (Equation (3.57)-(4.2)) , there are $6n_{se} - 2$ equations for $6n_{se}$ parameters for n_{se} engines. Other parameters of an SEA can be calculated by the given inlet temperature of the heating and cooling fluids. The efficiency and power of each engine can be obtained from Equation (3.53) and (3.52). The total efficiency and power of SEA can be obtained from powers of engines and outlet properties of the fluids.

表 4.1 Parameters of SEA models

Parameter	Value	Parameter	Value
Heating fluid	Air	\dot{m}_h	0.4 kg/s
Cooling fluid	Air	$T_{i,h}$	1000 K
n_{se}	6	$p_{i,h}$	5×10^5 Pa
s_{se}	25 Hz	\dot{m}_c	0.4 kg/s
p_{se}	5 MPa	$T_{i,c}$	300 K
$U_h A_h$	180 W/K	$p_{i,c}$	5×10^5 Pa
$U_c A_c$	180 W/K		

MATLAB is used as the programming tool to build the models of SEAs, and CoolProp is used to provide fluid properties for MATLAB program. Five basic SEA models composed of the aforementioned Stirling engines and fluids are built. To compare SEA connection types under various conditions, several parameters are investigated to find out their effects on SEA performance.

Figure 4-3 shows the solution algorithm of the SEA model. Flowchart (a) shows the algorithm to solve a Stirling engine known inlet parameters of the fluids. Flowchart (b) shows the algorithm to solve a Stirling engine known inlet parameters of heating fluid and outlet parameters of cooling fluid. Flowchart (c) shows the algorithm to solve the SEA model iteratively depending on different connection types. The levenberg-marquardt algorithm is applied to numerically solve the non-linear equations in the flowcharts.

4.3 Result analysis

SEA models with specified parameters in Table 4.1 are built and calculated. Results of the performances of the SEAs are shown in Table 4.2, it can be found that under specified parameters Type 3 has the highest efficiency and output power, while Type 1 has the lowest efficiency and output power.

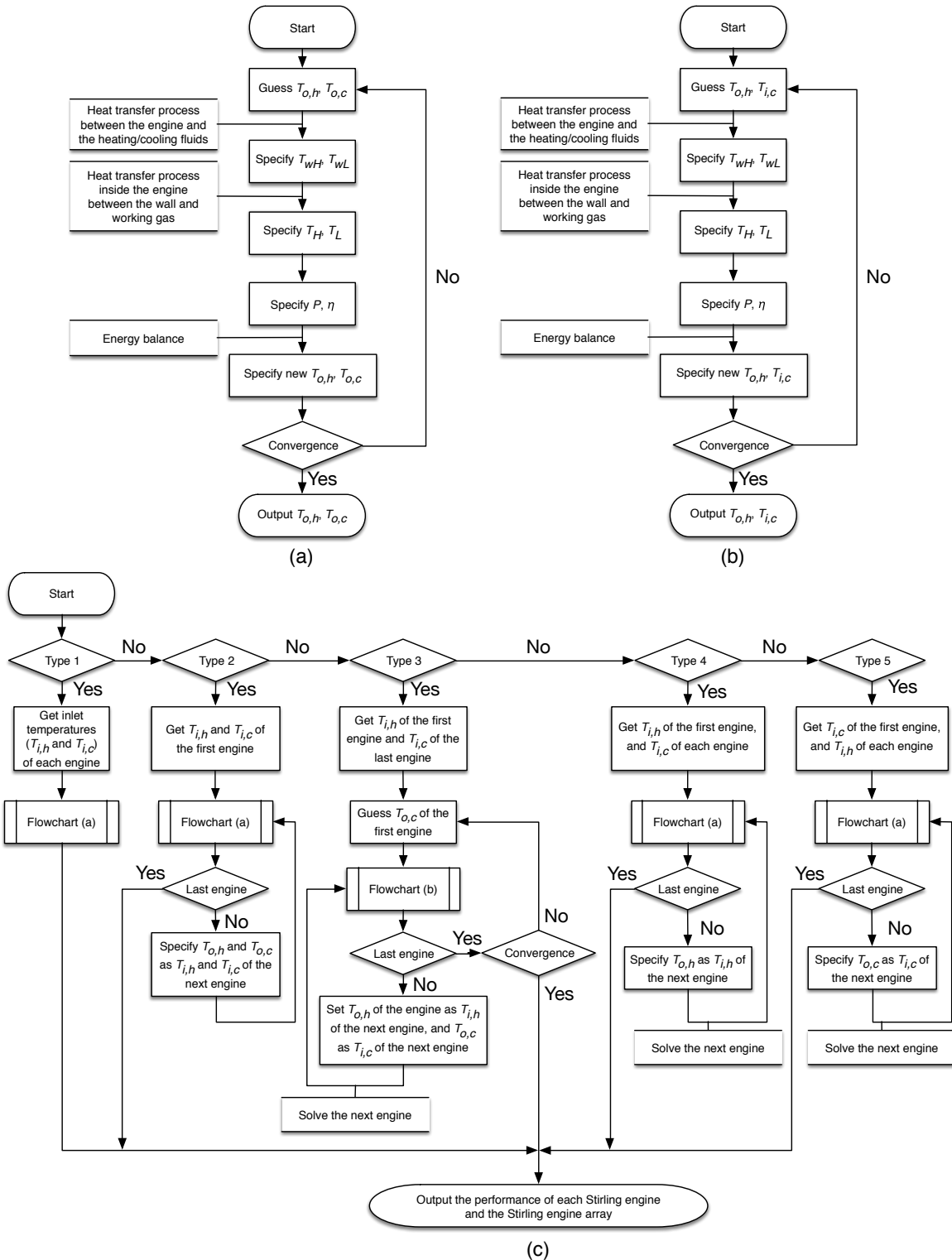


图 4-3 Flowcharts of the SEA model for performance analysis of the SEAs

表 4.2 Results of SEA models under specified parameters

Parameter	Value	Parameter	Value
η_1	0.2215	P_1	8022 W
η_2	0.2273	P_2	8483 W
η_3	0.2277	P_3	8512 W
η_4	0.2227	P_4	8116 W
η_5	0.2263	P_5	8399 W

4.3.1 Effects of $T_{i,h}$

According to Carnot cycle efficiency formula, the temperature of heating fluid determines the efficiency of Stirling engine array. For a Stirling engine, lower temperature heating fluid leads to a lower efficiency. The efficiency and output power may drop to 0 due to its insufficient heating fluid temperature to drive the engine.

Curves of performance of SEAs and $T_{i,h}$ are shown in Figure 4-4. As it is shown, with the increase of $T_{i,h}$, both η and P increase for all SEAs. For some types of SEA, when $T_{i,h}$ is lower than a critical temperature, some of the engines in the SEA will not work. In such situations, reduce the number of operating engines is a way to increase the total output power of the SEA. This strategy is used in the situation in Figure 4-4 when $T_{i,h}$ is low. Turning points on the $\eta-T_{i,h}$, $P-T_{i,h}$ curves shows the use of this strategy. The data points in the figure record the performance of the SEA with maximum output power under given conditions. For example, in SEA of Type 1, when $T_{i,h}$ is 820 K, if no engines is removed from the SEA, all the engines will stop due to the low inlet fluid temperature. Remove one engine out of the system will reduce the operating number of the engines from 6 to 5, and it will increase the inlet flow rate for each engine. This will make the remaining 5 engines work again and achieve the maximum output power under the condition of $T_{i,h} = 820$ K. 820 K is a critical temperature for Type 1, and a turning point at 820 K can be found on the $\eta-T_{i,h}$, $P-T_{i,h}$ curves of Type 1 in Figure 4-4.

From the curves in Figure 4-4, it can be concluded that Type 2 and Type 3 have the best performance, and Type 2 has the best adaptability for lower $T_{i,h}$. All engines in Type 2 work

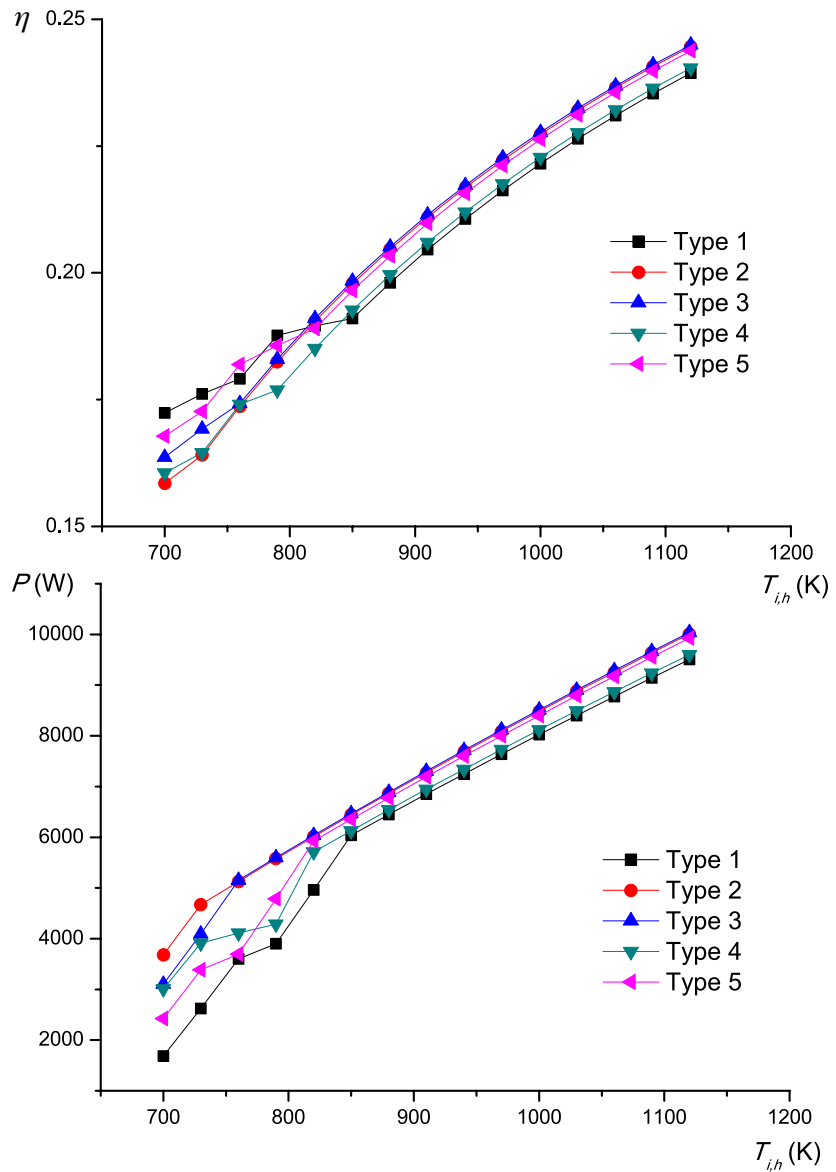


图 4-4 Influence of $T_{i,h}$ on efficiency and power of SEA

from 730 K.

4.3.2 Effects of $\dot{m}c_p$

According to Equation (3.59), (3.60), $\dot{m}c_p$ (both $\dot{m}_h c_{p,h}$ and $\dot{m}_c c_{p,c}$) will affect the heat transfer process, which is one of the vital factor for the performance of SEA.

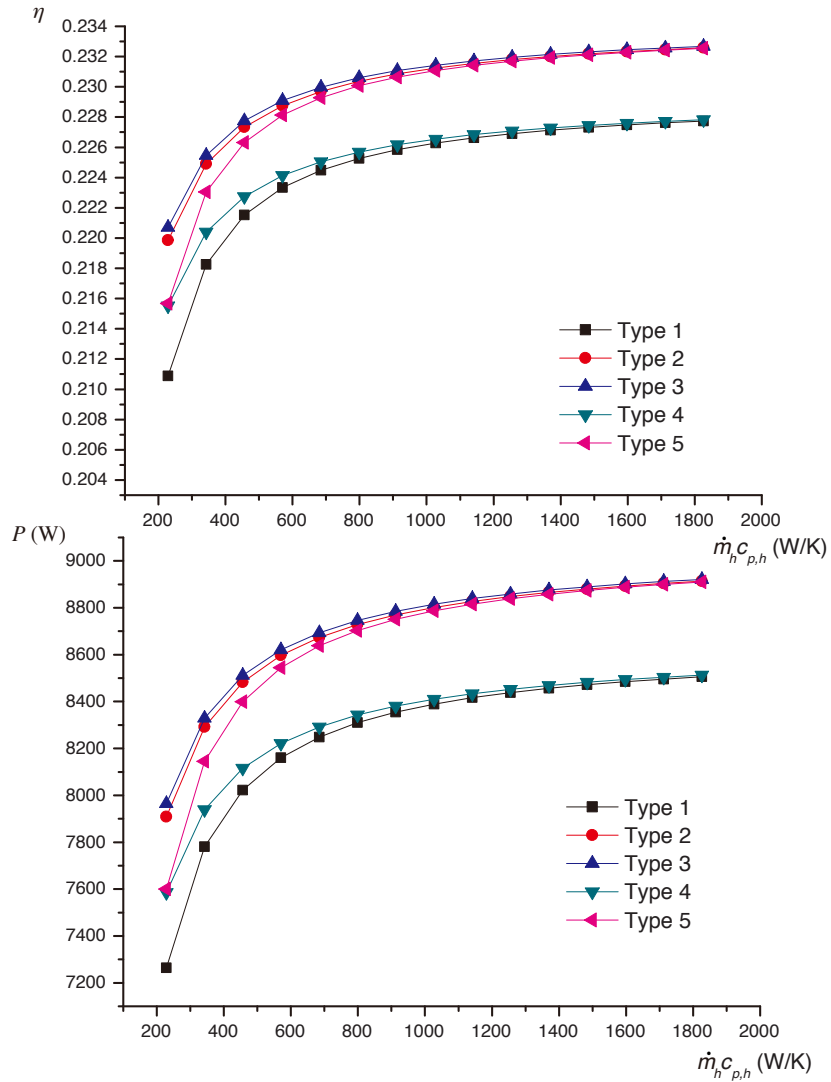


图 4-5 影响 $\dot{m}_h c_{p,h}$ 对 SEA 效率和功率的影响

Curves of performance of SEAs of different $\dot{m}_h c_{p,h}$ are shown in Figure 4-5. For a large

$\dot{m}_h c_{p,h} (> 800 \text{ W/K})$, Type 2 , Type 3 and Type 5 have similar performance, which can be interpreted as the cooling fluid has the same properties for the two types of SEAs, and for a large $\dot{m}_h c_{p,h}$, the heating fluid has similar effect after diverged. Similar performance of Type 1 and Type 4 can be also interpreted for the same reason.

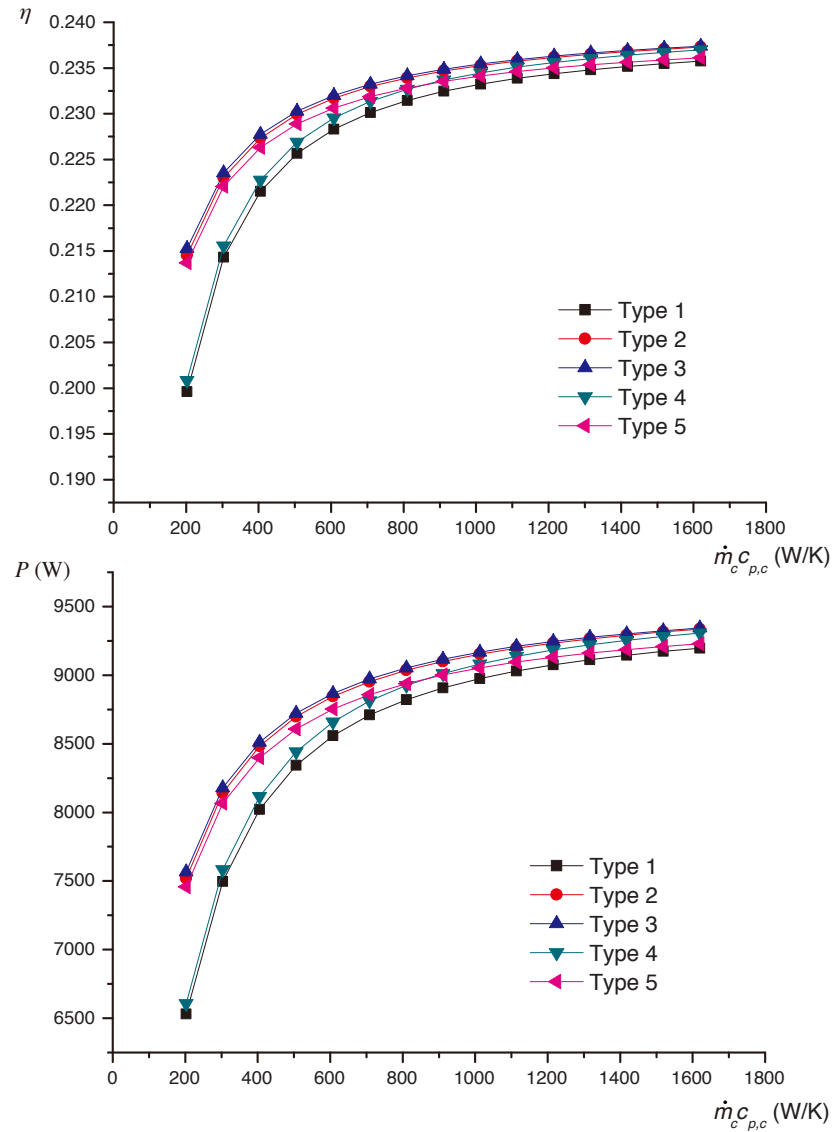


图 4-6 Influence of $\dot{m}_c c_{p,c}$ on efficiency and power of SEA

Curves of performance of SEAs of different $\dot{m}_c c_{p,c}$ are shown in Figure 4-6. For a

connection type of SEA, the performance improves with the increase of $\dot{m}_c c_{p,c}$. For a large $\dot{m}_c c_{p,c}$ (> 800 W/K), Type 2 and Type 3 have similar performance, which means the flow order doesn't affect the performance of SEA with a large $\dot{m}_c c_{p,c}$. There exists an intersection point (at 830 W/K) of curves of Type 4 and Type 5. For a larger $\dot{m}_c c_{p,c}$, Type 4 has a better performance, and vice versa. This can be interpreted that larger $\dot{m}_c c_{p,c}$ weaken the drawback of larger temperature rise of parallel flow, while for the heating fluid, temperature drop of serial flow is smaller than parallel flow.

4.3.3 Effects of n_{se}

By varying the number of engines in SEA, the performance levels changed accordingly. n_{se} may affect both the flow rates and temperatures of fluids of each engine. Figure 4-7 shows curves of performance of SEAs with different n_{se} . As it is shown, with an increase of n_{se} leads to a reduction of η for all SEAs due to smaller heating and cooling average temperature difference for more engines. For some types of SEA, when n_{se} is larger than a critical value, some of the engines in the SEA will not work and the curves will dive. E.g. for SEA of Type 1, when n_{se} is larger than 9, all the engines stop working, turning points at 9 can be found on the η - n_{se} , P - n_{se} curves in Figure 4-7.

For a certain connection type, increase n_{se} will reduce the efficiency of SEA. For some connection types, increase n_{se} will reduce the output power P due to inoperative engines and smaller output power engines. It is important to choose the number of engines for some connection types of SEA.

For Type 1, when $n_{se} \geq 10$, all engines stop working for given heating and cooling fluids due to small $\dot{m}c_p$. For Type 2 and Type 3, every engine in the SEAs works. η reduces with increasing n_{se} due to smaller temperature difference of the fluids, and P increases due to more operating engines. For Type 4, by checking results, it can be found that when $n_{se} = 13$, the last engine doesn't work; when $n_{se} = 14$, only the first 10 engines will work; when $n_{se} = 15$, the working engine number drops to 9. For Type 5, by checking results, it can be found that when $n_{se} = 12$, the last 2 engines stop working; when $n_{se} = 13$, only the first 8 engines will work; when $n_{se} = 14$, the working engine number drops to 6; when $n_{se} = 15$, the working engine number drops to 4. The aforementioned strategy is applied to achieve maximum total output power. For Type 4, when $n_{se} \geq 13$, the number of the operating engines is changed

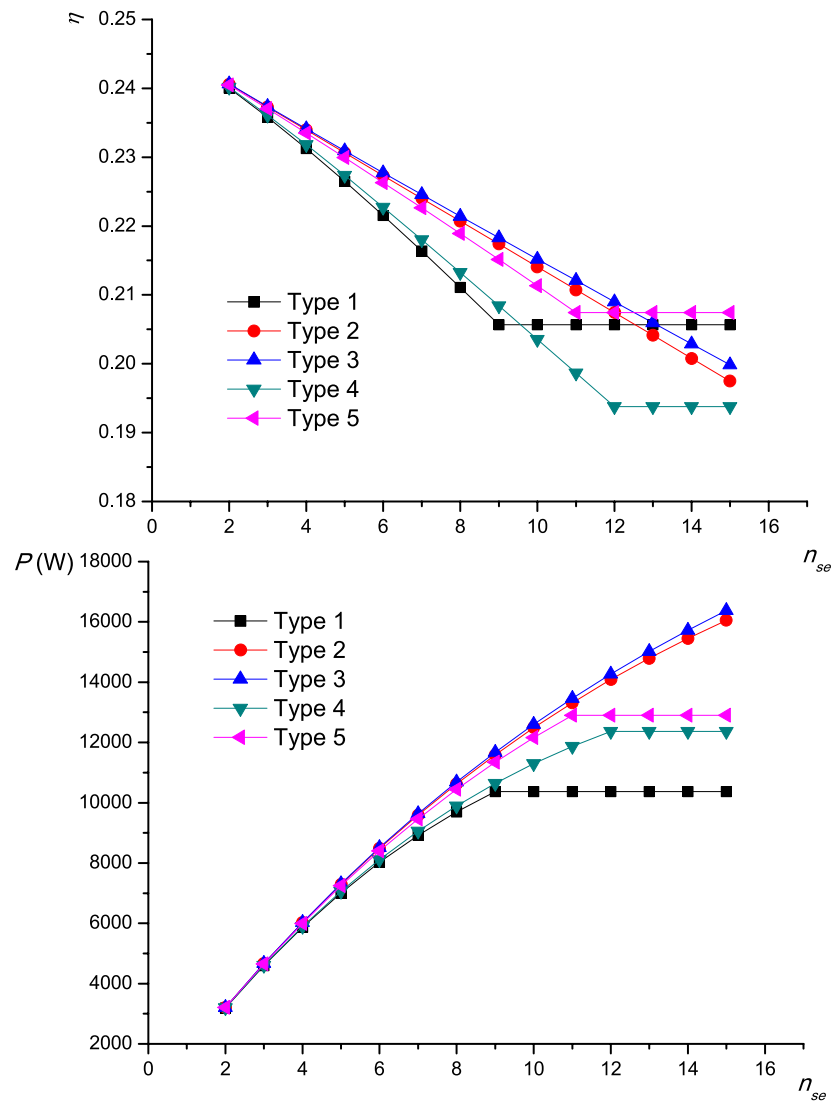


图 4-7 Influence of n_{se} on efficiency and power of SEA

to be 12 to achieve maximum output power. For Type 5, when $n_{se} \geq 12$, the number of the operating engines is changed to be 11 to achieve maximum output power. Horizontal lines in Figure 4-7 shows the application results of the strategy.

4.4 Conclusion

Connection type of the engines changes the flow rates and temperatures of the fluids, as a result the performance of the SEA will be different depending on the connection schemes. In order to compare performance of SEAs with different arrangements, five basic connection types of SEA are classified according to flow type and flow order.

Models of different connections of SEAs are developed to investigate the performance under different parameters and the impacts of $T_{i,h}$, $\dot{m}_h c_{p,h}$, $\dot{m}_c c_{p,c}$ and n_{se} with different connection types. It is found that

- (1) Reduce $T_{i,h}$ or $\dot{m}c_p$ will weaken the performance of SEA of all connection types. This is obvious since lower $T_{i,h}$ or $\dot{m}c_p$ leads to lower temperature distribution of the hot chamber of the Stirling engines. Lower temperature difference of the hot chamber and cold chamber leads to lower efficiency.
- (2) When inlet temperature of hot fluid ($T_{i,h}$) is lower than a critical value, some engines in the SEAs will stop working. Reduce the number of operating engines may help for the total output power.
- (3) Different connection types of SEAs show different adaptability for low $T_{i,h}$. Type 2 shows the best adaptability for low $T_{i,h}$. when $T_{i,h} \geq 730$ K, all the 6 engines are running.
- (4) SEA of serial flows (Type 3) has the best performance and adaptability under different parameters. Given heating and cooling fluids, using serial flow is the best choice for the connection type of an SEA.

五 Optimization of steam generating system

5.1 Steam generating subsystem

In a solar parabolic trough power plant in which intermediate heat-transfer fluid (take oil for instance) is used, heat addition to the working fluid (take water for instance) takes place in three counterflow heat exchangers (steam generator subsystem, SGSS) as shown in Figure 5-1. The SGSS consists of preheater, evaporator and superheater. The flow rates of both oil and water remain the same in the three heat exchangers. The water has phase change in the three heat exchangers, from liquid to vapor in the evaporator, however, oil remains liquid. The heat capacity of water in each heat exchanger differs significantly. The heat capacity of oil has no significant difference since no phase change. The heat transfer process is illustrated on Figure 5-2. Large temperature differences exist at the inlets and outlets of the heat exchangers, which leads to large entropy production during the entire heat exchange process.

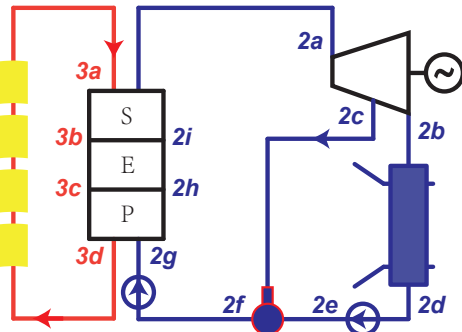


图 5-1 A typical solar parabolic trough system

The HTF at $3a$ represents the solar field outlet temperature and at $3d$, the field inlet temperature. The difference between the two can be reduced by increasing the flow rate of HTF through the field.

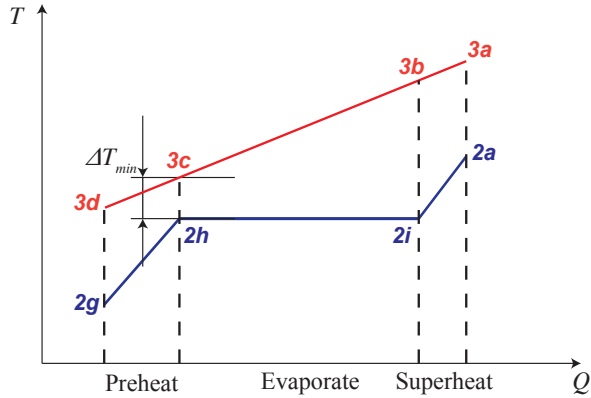


图 5-2 The steam generating process in counterflow heat exchangers

Since the heat exchangers must always stay a positive temperature difference for heat transfer, the temperature of oil must always be higher than the temperature of water. On the other hand, the temperature of oil should not be much higher than that of the water. Higher oil temperature leads to more heat losses in the solar field hence lower efficiency, more entropy production generated in the heat exchange process. Besides, higher oil temperature brings greater operational risks for the solar system. Setting the appropriate temperature difference between the oil and water is particularly important. The oil temperature must always higher (but not too much higher) than that of the water.

To find out the inlet and outlet temperatures of oil at the solar field, the lowest temperature difference of oil and water is defined as the pinch temperature ΔT_{min} . The temperatures of state points $2h$ and $2i$ are determined by the main pressure of the steam turbine in Figure 5-1, and T_{3b} is larger than T_{3c} . So state points $3c$ and $2h$, called the pinch points, are set to satisfy the pinch temperature, $T_{3c} - T_{2h} = \Delta T_{min}$. The pinch temperature ΔT_{min} is usually set to be $10\sim20$ K. It has to be mentioned that the temperature differences $T_{3d} - T_{2g}$ and $T_{3a} - T_{2j}$ worth attention to be not larger than ΔT_{min} .

However, even with the chosen pinch temperature ΔT_{min} , the temperature difference during the heat exchange process in SGSS is still large due to the phase change of water. Large temperature differences always exist at the inlet/outlet of the exchangers. As shown in Figure 5-3, it is a tradeoff to choose a mass flow rate of oil (\dot{m}_3). \dot{m}_3 affects the slope of curve $3a-3b-3c-3d$. A smaller \dot{m}_3 leads to a steeper curve, hence a larger $T_{3a} - T_{2j}$. A larger \dot{m}_3 leads to a more gentle curve, hence a larger $T_{3d} - T_{2g}$. The heat transfer processes in

SGSS always produce large entropy and exergy losses. In this regard, a new steam generating system to reduce exergy loss is put forward.

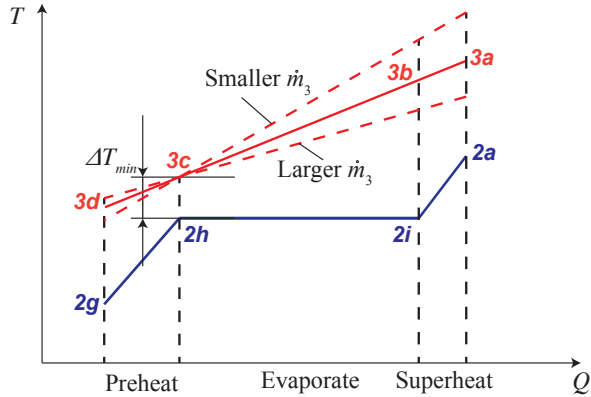


图 5-3 The tradeoff to choose \dot{m}_3

5.2 Multistage exergy loss reduction system

The reason of large temperature differences of the two curves in Figure 5-2 is that, the slope of oil curve changes slightly in different heat exchangers (preheater, evaporator and superheater), while the water curve changes dramatically due to large heat capacity c_p differences.

$$\Delta Q = c_p \dot{m} \Delta T \quad (5.1)$$

The slope of the curves are determined by $c_p \dot{m}$, \dot{m} can be altered to adjust the slope of the curves despite c_p is unalterable. All the water needs to be heated from supercooled water to superheated steam, which means \dot{m}_2 remains the same in the three heat exchangers. The last way is to change \dot{m}_3 in the heat exchangers.

As shown in Figure 5-4, the oil curve can be changed to the dashed curve. The temperature difference between the water curve and oil curve reduces significantly. Water is heated in three stages and the exergy loss reduces. The corresponding steam generating system is so called Multistage Exergy Loss Reduction System (MELRS). Figure 5-5 shows the schematic

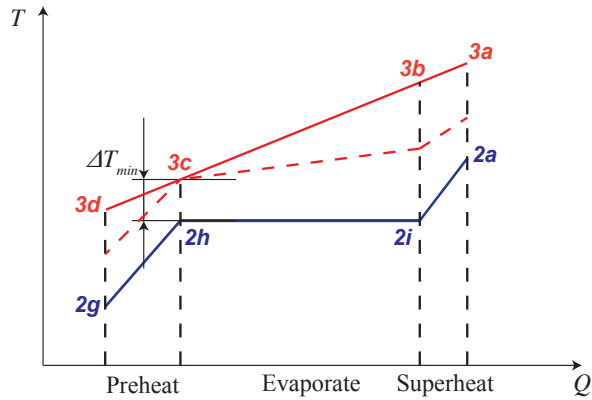


图 5-4 Change m_3 in the heat exchangers to reduce the temperature difference

diagram of the MELRS for comparison with typical solar parabolic trough system in Figure 5-1. The solar field in Figure 5-1 has been divided into three independent sectors. Each sector becomes the heat source of a range for the steam heating process: the first corresponds to overheating, the second to evaporation, and the third to preheating. It has to be mentioned that the collectors in the schematic diagram are only used for explanation. The arrangement of these collectors can be in series, in parallel or combination of both.

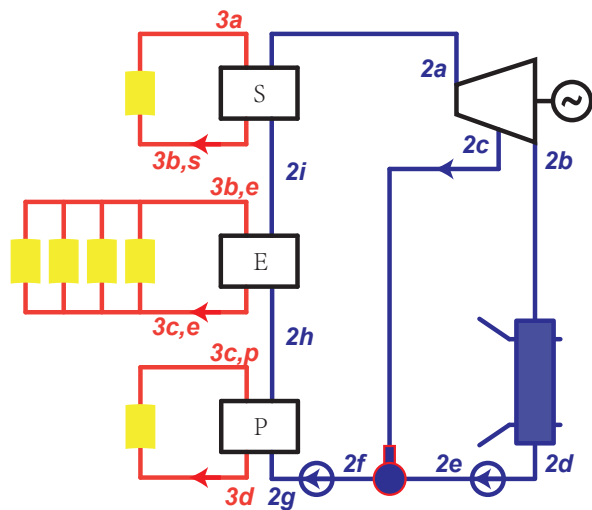


图 5-5 The schematic diagram of the MELRS

To optimize the MELRS, considering the limitation of pinch temperature, temperatures

of the oil at the inlet/outlet of the heat exchangers can be set according to following rules:

$$T_{3d} - T_{2g} = \Delta T_{min}$$

$$T_{3c,p} = T_{3c,e} = T_{3c}$$

$$T_{3c} - T_{2h} = \Delta T_{min}$$

$$T_{3b,e} = T_{3b,s} = T_{3b}$$

$$T_{3a} - T_{2a} = \Delta T_{min}$$

A large flow rate of oil in the evaporator $\dot{m}_{3,e}$ can be applied to reduce the temperature T_{3b} hence the temperature differences of the oil and water. However, a large $\dot{m}_{3,e}$ requires more pump power consumption for the oil circuits. Besides, $\dot{m}_{3,e}$ is limited for the limitation of oil velocity in the pipes.

The enthalpy of each state point can be determined by its temperature and pressure.

The optimum oil average temperature in the solar field corresponds to the preheater is

$$T_{3,p} = (T_{2g} + T_{2h})/2 + \Delta T_{min} \quad (5.2)$$

The optimum oil flow rate in the solar field corresponds to the preheater is

$$\dot{m}_{3,p} = \dot{m}_2(h_{2h} - h_{2g})/(h_{3c} - h_{3d}) \quad (5.3)$$

The optimum oil average temperature in the solar field corresponds to the evaporator is

$$T_{3,e} = (T_{3b} + T_{3c})/2 \quad (5.4)$$

The optimum oil flow rate in the solar field corresponds to the evaporator is

$$\dot{m}_{3,e} = \dot{m}_2(h_{2i} - h_{2h})/(h_{3b} - h_{3c}) \quad (5.5)$$

The optimum oil average temperature in the solar field corresponds to the superheater is

$$T_{3,s} = (T_{3b} + T_{2a} + \Delta T_{min})/2 \quad (5.6)$$

The optimum oil flow rate in the solar field corresponds to the superheater is

$$\dot{m}_{3,s} = \dot{m}_2(h_{2a} - h_{2i})/(h_{3a} - h_{3b}) \quad (5.7)$$

5.3 Comparison

To find out the effect of MELRS, models of traditional SGSS and proposed MELRS are developed based on the models of the components created in Chapter 3. To clearly find out the influence of oil temperature on the performance of the trough collectors, Equation (3.7) in Section 3.1.1 is used.

The exergy loss caused by a heat exchange process per unit time

$$\dot{I} = T_{amb}(\sum \dot{m}_o s_o - \sum \dot{m}_i s_i) \quad (5.8)$$

表 5.1 Main parameters used for SGSS and MELRS

Parameter	Value	Parameter	Value
I_r	700 W/m ²	T_s	613.15 K
P_{ge}	6×10^6 W	p_s	2.35×10^6 Pa
$\eta_{i,tb}$	0.711	p_c	1.5×10^4 Pa
η_{ge}	0.975	p_{de}	1×10^6 Pa
ΔT_{min}	15 K		

The turbine and deaerator are the same for the two systems (SGSS and MELRS), so that the corresponding state points of water are the same. The main parameters are listed in Table 5.1.

As discussed in Section 5.2, T_{3b} is an undetermined value. Figure 5-6 shows the minimum and maximum value of it. $T_{3b,min}$ means the limit situation of unlimited flow rate of oil in the evaporator, $T_{3b,min} = T_{3c}$. T_{max} has the traditional effect of temperature differences in the evaporator and superheater, $\dot{m}_{3,e} = \dot{m}_{3,s}$. In our research, T_{3b} is set to be the average value of the two limitations, $T_{3b} = (T_{3b,min} + T_{3b,max})/2$.

$$\frac{T_{3b,max} - T_{3c}}{T_{3a} - T_{3c}} = \frac{T'_{3b} - T_{3c}}{T'_{3a} - T_{3c}} \quad (5.9)$$

where T'_{3a} and T'_{3b} are the inlet oil temperature of superheater and evaporator in SGSS respectively.

表 5.2 Simulation results of SGSS and MELRS

SGSS	MELRS		
	$T_{3b,max}$	T_{3b}	$T_{3b,min}$
T_{2a}	613.15 K		
T_{2i}	493.83 K		
T_{2h}	493.83 K		
T_{2g}	453.28 K		
T_{3c}	508.83 K		
T_{3a}	653.15 K	628.15 K	628.15 K
T_{3b}	634.11 K	612.41 K	560.62 K
T_{3d}	495.43 K	468.28 K	468.28 K
\dot{m}_{3p}	47.8 kg/s	16.1 kg/s	16.1 kg/s
\dot{m}_{3e}	47.8 kg/s	58.6 kg/s	120.8 kg/s
\dot{m}_{3s}	47.8 kg/s	59.4 kg/s	14.3 kg/s
\dot{I}_p	4.80×10^4 W	2.58×10^4 W	2.58×10^4 W
\dot{I}_e	1.10×10^6 W	9.68×10^5 W	6.24×10^5 W
\dot{I}_s	1.81×10^5 W	1.42×10^5 W	9.19×10^4 W
\dot{I}_{total}	1.33×10^6 W	1.14×10^6 W	7.44×10^5 W
η_p	0.699	0.703	0.703
η_e	0.673	0.678	0.689
η_s	0.633	0.648	0.662
$\eta_{overall}$	0.670	0.676	0.686
			0.695

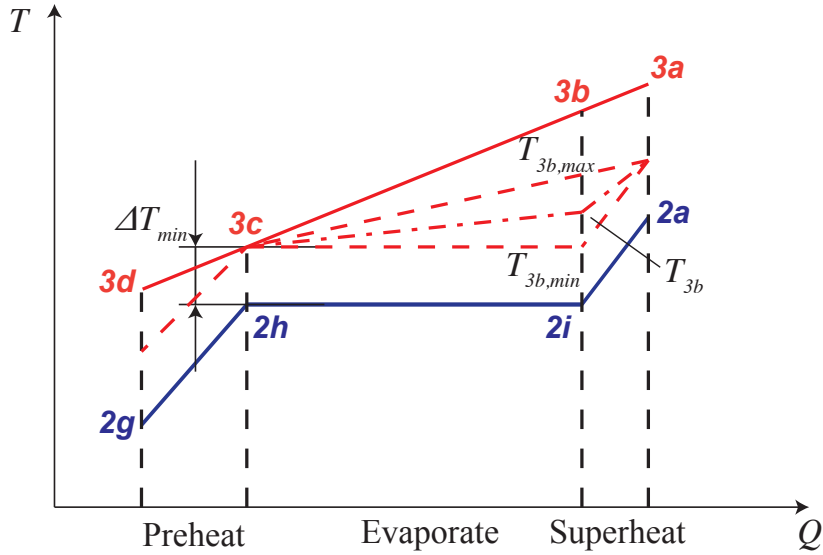


图 5-6 T_{3b} in the T - Q diagram of the heat transfer processes

Simulation results of the four system models are listed in Table 5.2. It can be found that MELRS can effectively reduce the exergy loss of the steam generating process. The exergy loss can be reduced from 14.3% up to 76.7% for the three MELRS. The overall thermal efficiency of the solar fields can be improved from 0.9% up to 3.6%.

It is worthy pointing that, for the situation $T_{3b} = T_{3b,min}$, when $\dot{m}_{3e} = \infty$, the correlation (5.8) is not applicable. The new correlation listed below is applied for the isothermal heat transfer process

$$\dot{I} = T_{amb} \left(\frac{Q}{T_{2h}} - \frac{Q}{T_{3c}} \right) = \frac{QT_{amb}(T_{3c} - T_{2h})}{T_{2h}T_{3c}} \quad (5.10)$$

where, Q is the heat transferred per unit time in the evaporator.

T_{2a} , T_{2i} , T_{2h} , T_{2g} and T_{3c} are the same for SGSS and different MELRSs for the same water side processes. The different mass flow rates of the oil lead to different oil temperatures in the heat exchangers, and hence different exergy loss. It can be found that the exergy losses in preheaters of MELRSs (2.58×10^4 W) are smaller than that of SGSS (4.80×10^4 W). The exergy losses in evaporators of different MELRSs vary greatly, from 9.68×10^5 W to 2.41×10^5 W for oil flow rate from 58.6 kg/s to infinity. Exergy loss in the evaporator takes the largest portion of the steam generating process, which takes about 82.8%, 85.2%, 83.8% and 78.0% for SGSS and MELRSs separately. Increasing flow rate of the heating fluid in

the steam generating process can effectively reduce the exergy loss. The exergy losses in superheaters of MELRSs (1.42×10^5 W, 9.19×10^4 W and 4.24×10^4 W) are much smaller than that of SGSS (1.81×10^5 W) due to large temperature differences in the traditional superheaters.

It can be found that MELRS can effectively reduce exergy loss hence improve the system efficiency compared to traditional SGSS. The thermal efficiency for the corresponding solar field for the preheater (η_p), evaporator (η_e) and superheater (η_s) of MELRSs are higher than that of SGSS (virtual solar fields). The overall thermal efficiency ($\eta_{overall}$) of the solar field can be improved effectively.

5.4 Conclusion

In this chapter, a novel multistage exergy loss reduction system is proposed to reduce the large exergy loss in traditional solar parabolic trough power plants. Traditional solar field is divided into three solar fields to provide heat for the preheater, evaporator, and superheater, respectively. Different flow rates in the three solar fields provide the ability to reduce temperature difference for the heat exchange processes.

Smaller temperature difference leads to lower oil temperature and therefore higher solar field thermal efficiency. Besides, the different temperature ranges of different solar fields provide the convenience of the application of different types of collectors.

The analytical model of the steam generating system is developed. A flow control strategy of HTF depending on the analytical system model is derived. Energy and exergy efficiency of the MELRS is analyzed and compared with the SGSS of traditional solar parabolic trough power plant. Result shows that MELRS can effectively reduce the exergy loss in the heating process, and the performance of the plant can be improved. The exergy loss can be reduced from 14.3% up to 76.7% for the three typical MELRSs. The overall thermal efficiency of the solar fields can be improved from 0.9% up to 3.6%.

六 Cascade system performance evaluation

6.1 System description

In Section 2.3, two typical cascade system topologies (see Figure 2-18) are selected for further investigation. It has to be pointed out that, in Chapter 5, multistage exergy loss reduction system (MELRS) is proposed and analyzed. It is obvious that MELRS has better energy and exergy performance than SGSS. However, the MELRS is not applied in this chapter for investigation. There are several reasons. First, in order to clearly find out the advantages of cascade collection and cascade utilization of the cascade systems, it is not applied in the cascade system in this chapter. Second, compared with traditional SGSS, MELRS only changes the solar field, which has no influence on the cascade utilization of the cascade system. It can be easily applied in the cascade system analyzed in this chapter in the future without influence of existing calculations. Third, the MELRS proposed in Chapter 5 needs further research in the future. Different kinds of solar collector technologies can be applied in different solar fields. For example, linear Fresnel reflectors or flat collectors can be applied for preheating solar field to reduce costs; molten salt can be used as heat transfer fluid in the superheating solar field to increase the main steam temperature of the Rankine cycle.

Two typical cascade system topologies are selected in Chapter 2. Both systems take advantage of the different types of heat collectors and different thermal cycles to achieve cascade collection of energy and cascade utilization. However, this chapter focuses on the first model because it is more widely used and more suitable for large-scale applications. Figure 6-1 shows the scheme sketch of the cascade system. In this system, dish collectors are used to provide heat for Stirling engines and air-to-water heat exchanger. Trough collectors are used to provide heat for steam generating processes (preheating, evaporating and superheating) in the Rankine cycle. Hot air is produced by the dish collectors. High temperature (1073 K) air is used to provide heat to Stirling cycle to get higher conversion efficiency, then the air is used to provide heat for air-to-water heat exchanger to use the lower temperature energy in Rankine cycle effectively. Besides, feed water of Rankine cycle is used to cool the Stirling engines to recycle the heat wasted conventionally. The Stirling engines are connected in series for better performance.

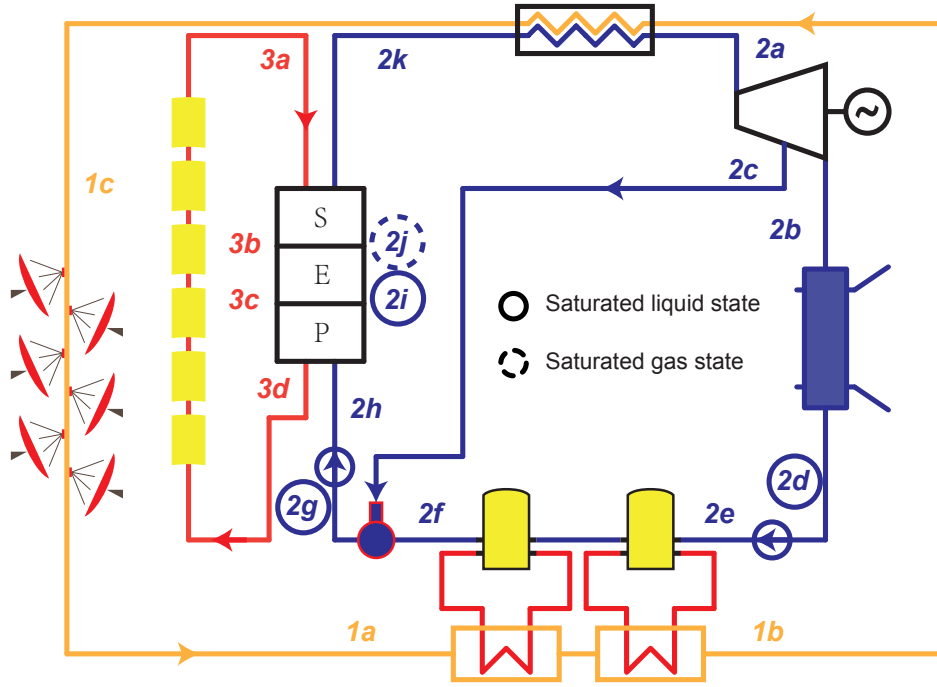
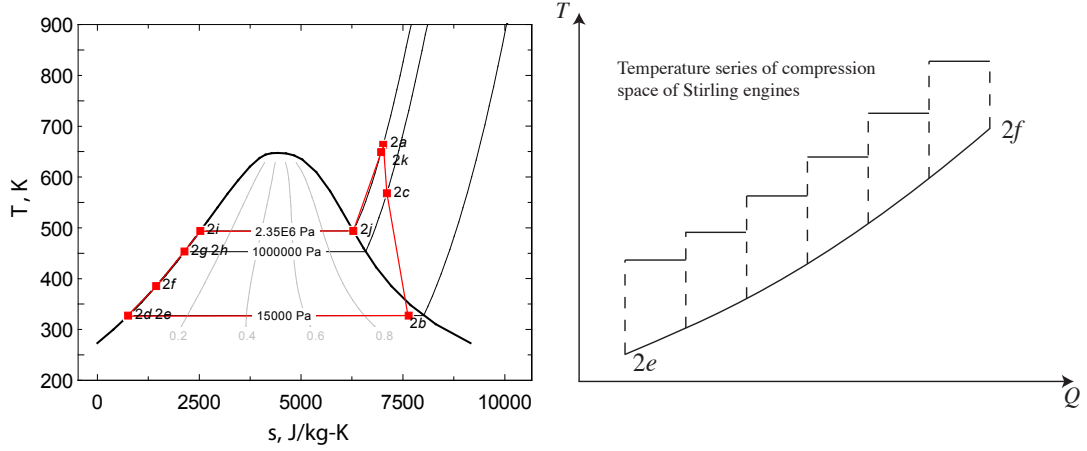


图 6-1 Sketch of the cascade system

Figure 6-2a shows the $T-s$ diagram of the water circuit in the cascade system. In this Rankine cycle, the heat provided in process $2e-2f$ comes from the Stirling engines, which increases the power of Rankine cycle. Figure 6-2b shows the heat transfer diagram of this process.

To build the cascade system model, several simplifying assumptions are made:

- Steady state at nominal load of the system is analyzed.
- Pressure drop due to flow is negligible.
- The leak of working fluid in the pipes is neglected.
- Same isentropic efficiency of steam turbine with different loads and in different stages.
- Heat loss that occurs from the tube to the atmosphere is not considered.
- There is no heat loss to the environment for Stirling engines.
- Simple models are used of some processes and equipment.
- A symmetrical regenerator behavior is assumed so that a single effectiveness can be



(a) T - s diagram of the water circuit

(b) Diagram of process $2e-2f$

图 6-2 Diagrams of water circuit and $2e-2f$ process

defined as $e = (T_R - T_L)/(T_H - T_L)$.^[114,115]

- A linear temperature profile across the regenerator exists, the mean effective temperature $T_R = (T_H - T_L)/\ln(T_H/T_L)$.^[122,123]

6.2 System evaluation method

6.2.1 System performance

The cascade system uses different types of collectors and different kinds of thermodynamic cycles. They are closely linked together. It is unable to indicate the output power of one specific kind of collector. A common approach is to define the overall efficiency of the system. The overall solar-to-electric efficiency equals to the total output power divided by the total input solar energy.

$$\eta_{cs} = \frac{P_{cs}}{I_r A_{cs}} = \frac{P_{rk} + P_{sea}}{I_r A_{tc} + I_r A_{dc}} \quad (6.1)$$

where P_{rk} is the output power of the Rankine cycle, and P_{sea} is the total output power of the Stirling engines.

$$P_{rk} = P_{tb} - P_{pu}/\eta_{ge} \quad (6.2)$$

$$P_{tb} = (1 - y) \dot{m}_2 (h_{2a} - h_{2b}) + y \dot{m}_2 (h_{2a} - h_{2c}) \quad (6.3)$$

$$P_{pu} = (1 - y) \dot{m}_2 (h_{2e} - h_{2d}) + \dot{m}_2 (h_{2h} - h_{2g}) \quad (6.4)$$

$$P_{sea} = \dot{m}_1 (h_{1,i,1} - h_{1,o,n_1}) - \dot{m}_2 (h_{2,o,n_1} - h_{2,i,1}) \quad (6.5)$$

As mentioned above, $\frac{P_{rk}}{I_r A_{tc}}$ does not indicate the efficiency of solar trough collectors and $\frac{P_{sea}}{I_r A_{dc}}$ does not indicate the efficiency of solar dish collectors.

6.2.2 System comparison

The other one is to compare with existing solar thermal power technologies. This requires more consideration.

- (1) Compare with parabolic trough.

When compared with parabolic trough system, a higher efficiency of the cascade system may be explained as the usage of solar dish collector. It is difficult to tell if the higher efficiency is due to the usage of cascade system or the usage of dish collector.

- (2) Compare with parabolic dish.

When compared with parabolic dish system, a lower cost of the cascade system may be explained as the usage of solar trough collector. It is difficult to tell if the lower cost is due to the usage of cascade system or the usage of trough collector.

- (3) Compare with stand-alone systems.

It is important to choose good stand-alone systems. An intuitive idea is to use both parabolic trough and parabolic dish for comparison. To compare two systems, contrast conditions needs to be set.

If the same output power was selected as the contrast condition, different amount of trough collectors and dish collectors will be used in the cascade system and stand-alone systems. It is complicated for cost comparison due to different prices of trough collectors and dish collectors.

A better way is to select the same collectors as the contrast condition. Since the output is electricity, it is much more convenient for both efficiency comparison and cost comparison.

6.3 System parameters

In order to study the efficiency of the system and its influencing factors, a model of the cascade system is required. Chapter 3 introduces the system modeling process in detail. After the system modeling process, another important task is to determine the system parameters.

The system mainly consists of the following components:

6.3.1 Environment

Typical environmental parameter values of Wuhan are used for the cascade system design.

$$I_r = 700 \text{ W/m}^2, T_{amb} = 293 \text{ K}, p_{amb} = 1 \times 10^5 \text{ Pa}, v_{amb} = 1 \text{ m/s}.$$

6.3.2 Steam Turbine

A steam turbine product, N-6 2.35, of Qingdao Jieneng Power Station Engineering Co., Ltd is used for calculation. Its nominal parameters are: $P = 6 \text{ MW}$, $p_s = 2.35 \text{ MPa}$, $T_s = 390^\circ\text{C}$, $\dot{m} = 32.09 \text{ t/h}$, $p_c = 0.015 \text{ MPa}$, $s_{tb} = 3000 \text{ rpm}$.

Known the main steam parameters, its enthalpy and entropy can be obtained by using CoolProp, $h_s = 3.2203 \times 10^6 \text{ J/kg}$, $s_s = 7.0149 \times 10^3 \text{ J/(kg} \cdot \text{K)}$.

$$\text{Exhaust enthalpy of the turbine } h_c = h_s - \frac{P}{\dot{m}} = 2.5472 \times 10^6 \text{ J/kg}.$$

Known exhaust pressure and $s_{i,c} = s_s$, isentropic exhaust enthalpy of the turbine can be obtained by using CoolProp, $h_{i,c} = 2.2737 \times 10^6 \text{ J/kg}$.

$$\text{So the isentropic efficiency of the turbine can be obtained from } \eta_{i,tb} = \frac{h_s - h_c}{h_s - h_{i,c}} = 0.71.$$

Taking into account of the application in solar trough system, the designed parameters of the steam turbine are shown in Table 6.2.

6.3.3 Trough collector

LUZ solar collector LS-3 is used as the trough collector for its known test data. Its main characters are listed in Table 6.1.^[101]

6.3.4 Dish collector

A dish reflector product of SES (Stirling Energy System) is used as the reflector, the receiver is self-designed. The key parameters of the dish collector are listed in Table 3.1.

表 6.1 Main parameters of LS-3

Parameter	Value	Parameter	Value	Parameter	Value
A_{pc}	570.2 m ²	w_{dc}	5.76 m	L_{dc}	99 m
f	1.71 m	d_i	0.066 m	d_o	0.07 m
$d_{abs,i}$	0.113 m	$d_{abs,o}$	0.115 m	Rim angle	80°
ϵ	0.15	η_{peak}	0.77	ρ	0.94
τ	0.95	α	0.96	Fe	0.97

6.3.5 Stirling engines

The Stirling engines used in the cascade system are the same with the one analyzed in Section 3.1.3. It is a GPU-3 type Stirling engine, Table 3.2 shows its parameters.

6.3.6 Preheater

Water is heated to saturated water in the preheater by the oil. For outlet stream of water, $x = 0$. Besides, considering the minimum temperature difference required between oil and water, $T_{3c} - T_{2i} = \Delta T_{3,2,min}$. $\Delta T_{3,2,min}$ is set to be 15 K.

6.3.7 Evaporator

Water is heated from saturated liquid water to saturated steam in the evaporator. For outlet stream of water, $x = 1$.

6.3.8 Superheater

The inlet temperature of oil is limited by the oil properties. In the cascade system, Therminol VP-1 Synthetic oil is used as the heat transfer fluid. Its properties can be obtained from both EES and CoolProp. The inlet temperature of the oil of superheater is set as $T_{3a} = 623$ K.

6.3.9 Deaerator

The deaerator has two inlet streams and one outlet stream. They have the same pressure, $p_{se} = 1 \times 10^6 \text{ Pa}$. The outlet stream of the deaerator is saturated water.

6.3.10 Air-water heat exchanger

The inlet temperature is set as $T_{1b} = 673 \text{ K}$.

6.3.11 Main design parameters summary

The main design parameters of the cascade system can be concluded in Table 6.2.

表 6.2 Basic design parameters of the cascade system

Parameter	Value	Parameter	Value	Parameter	Value
I_r	700 W/m^2	$T_{dc,o}$	1073 K	n_{se}	100
T_{amb}	293 K	p_{dc}	$5 \times 10^5 \text{ Pa}$	T_s	613 K
p_{amb}	$1 \times 10^5 \text{ Pa}$	$\Delta T_{3,2,min}$	15 K	p_s	$2.35 \times 10^6 \text{ Pa}$
v_{amb}	1 m/s	$T_{tc,o}$	623 K	p_c	$1.5 \times 10^4 \text{ Pa}$
P_{ge}	$6 \times 10^6 \text{ W}$	p_{tc}	$2 \times 10^6 \text{ Pa}$	$T_{s,d}$	663 K
$T_{dc,i}$	623 K	T_{1b}	673 K	p_{de}	$1 \times 10^6 \text{ Pa}$

6.4 Stand-alone system selection

Figure 6-3 shows the sketch of the stand-alone systems. These two stand-alone systems are developed for comparison. They use the same dish collectors and trough collectors with the same thermal efficiencies of the cascade system.

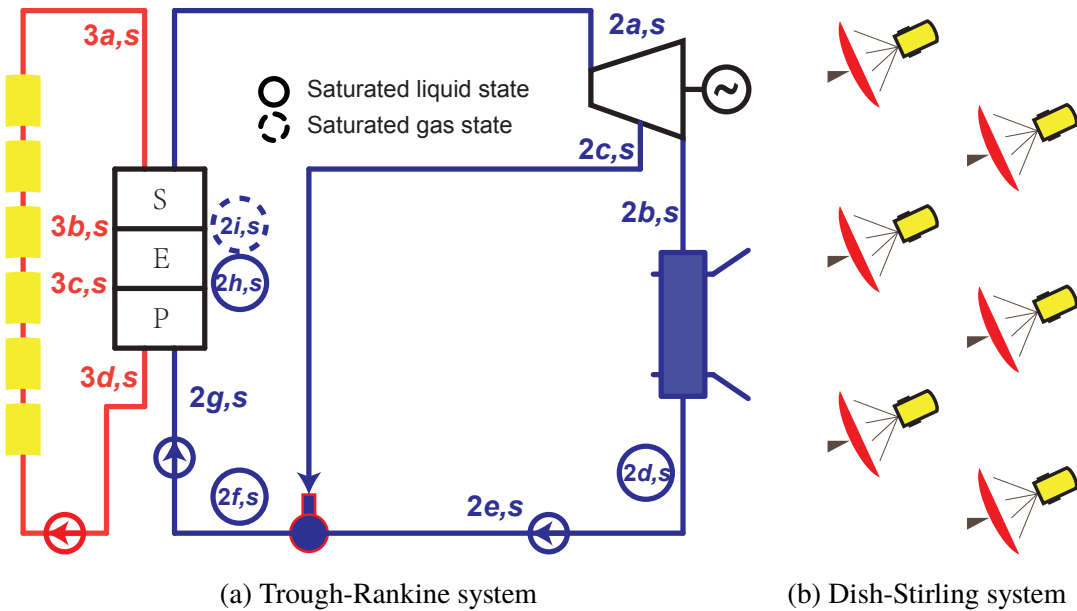


图 6-3 Sketch of the stand-alone systems

6.4.1 Stand-alone trough-Rankine system

Steam turbine has the same main parameters and isentropic efficiency with that of the cascade system. Working pressure of deaerator is the same of the cascade system. So parameters of state $2b, s$ and $2c, s$ in Figure 6-3 of the steam turbine can be expressed by

$$\eta_{i,tb} = (h_{2a,s} - h_{2b,s}) / (h_{2a,s} - h_{i,2b,s}) = (h_{2a,s} - h_{2c,s}) / (h_{2a,s} - h_{i,2c,s}) \quad (6.6)$$

The output power of steam turbine

$$P_{tb,s} = (1 - y_s) \dot{m}_{2,s} (h_{2a,s} - h_{2b,s}) + y_s \dot{m}_{2,s} (h_{2a,s} - h_{2c,s}) \quad (6.7)$$

The output power of generator

$$P_{ae,s} = P_{tb,s} \eta_{ae} \quad (6.8)$$

The total power of pumps

$$P_{pu,s} = (1 - y_s) \dot{m}_{2,s} (h_{2e,s} - h_{2d,s}) + \dot{m}_{2,s} (h_{2g,s} - h_{2f,s}) \quad (6.9)$$

Heat injected in the water circuit

$$Q_{2,s} = \dot{m}_{2,s} (h_{2a,s} - h_{2g,s}) \quad (6.10)$$

The generator efficiency is the same of that in the cascade system, and the efficiency of Rankine cycle can be expressed as

$$\eta_{rk,s} = (P_{tb,s} - P_{pu,s}/\eta_{ge})/Q_{2,s} \quad (6.11)$$

6.4.2 Stand-alone dish-Stirling system

In the stand-alone dish-Stirling system, Stirling engines with the same number of dish collectors are directly put on the focuses of the dish collectors. Water is used for cooling the Stirling engines. $T_{H,s}$ is chosen to be equal to outlet temperature of air in dish receiver. $T_{L,s}$ is chosen to be 310 K, the default expansion temperature in Fraser's dissertation^[125] for the calculation of 4-95 NKII engine. k and γ are chosen the same value as that of the Stirling engines in the cascade system.

$$\eta_{sea,s} = \frac{T_{H,s} - T_{L,s}}{T_{H,s} + \frac{1 - e_s}{k - 1} \cdot \frac{T_{H,s} - T_{L,s}}{\ln \gamma}} \quad (6.12)$$

where, $T_{R,s} = \frac{T_{H,s} - T_{L,s}}{\ln(T_{H,s}/T_{L,s})}$ and $e_s = \frac{T_{R,s} - T_{L,s}}{T_{H,s} - T_{L,s}}$.

The total power of Stirling engines

$$P_{sea,s} = n_{dc} A_{dc} I_r \eta_{dc} \eta_{sea,s} \quad (6.13)$$

6.5 Comparison with stand-alone system

The results presented in Table 6.3 are issued using design parameters with counterflow of two fluids in Stirling engine array as the default flow type. It is shown that the cascade system with design parameters can achieve higher efficiency compared to corresponding stand-alone systems. Although the efficiency of the Stirling engine array is lower, the efficiency of the Rankine cycle is higher. The overall output power of the cascade system is 3.83×10^4 W higher.

表 6.3 Some important results using design parameters

Parameter	Value	Parameter	Value	Parameter	Value
η_{cs}	0.1974	$\eta_{sea,s}$	0.3786	$P_{ge,s}$	5.826×10^6 W
η_s	0.1962	η_{rk}	0.2660	P_{sea}	3.552×10^5 W
η_{diff}	0.0062	$\eta_{rk,s}$	0.2678	$P_{sea,s}$	4.909×10^5 W
η_{sea}	0.3407	P_{ge}	6×10^6 W	P_{diff}	3.830×10^4 W

6.5.1 Effects of I_r

It is found that I_r can affect the efficiency difference of cascade system and stand-alone systems η_{diff} . Figure 6-4 shows curve fits of efficiency differences η_{diff} versus I_r with a series of different Stirling engine array power ratios. As it can be seen, for a high I_r ($I_r > 550$ W/m²), $\eta_{diff} > 0$, the cascade system can achieve a higher efficiency than corresponding stand-alone systems. For a low I_r ($I_r < 550$ W/m²), η_{diff} may be negative. At this situation, the cascade system achieves a lower efficiency than corresponding stand-alone systems. This may be explained that instead of cooling water in the stand-alone dish-Stirling system, condensed water of Rankine cycle is used to cool the Stirling engines, which jeopardizes the heat dissipation and leads to a lower power of the Stirling engines. For a low I_r , the increased power of steam turbine due to absorbed heat by the condensed water is lower than the power loss of the Stirling engines. It can also be found that higher I_r can achieve higher η_{diff} , which can be interpreted as the heat absorbed by the condensed water increases with I_r . So a higher I_r location is always more suitable for cascade system. This means I_r is a key factor to determine whether cascade system should be applied in a certain location.

6.5.2 Effects of β

As it can be seen in Table 6.3, the η_{diff} is very small with the design parameters given above. A reason η_{diff} to be so small is that β , the ratio of power of Stirling engines to the total power, is very small, the heat released by the Stirling engine array is a small portion of the heat absorbed in the Rankine cycle. So increase β may achieve higher η_{diff} . The relationship

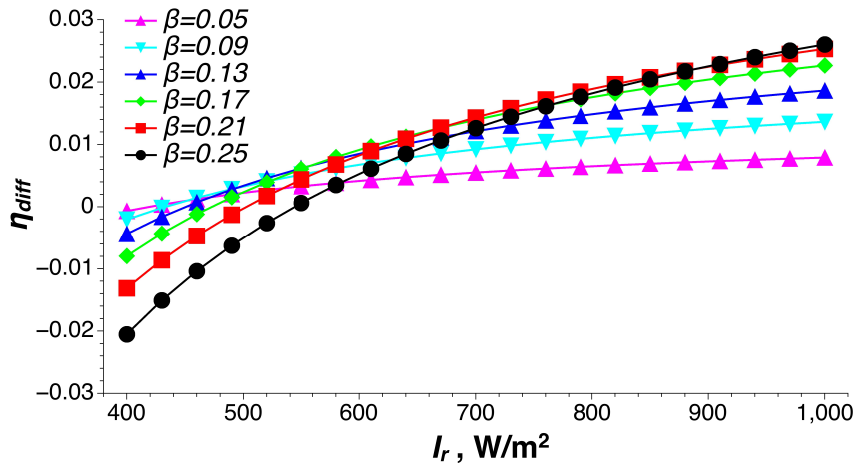


图 6-4 Curve fits of efficiency difference η_{diff} versus I_r

between η_{diff} and β under a series of I_r is shown in Figure 6-5. It can be found that, for a high I_r , increase β may achieve a higher η_{diff} , but there is a limit. For $I_r = 900\text{W/m}^2$, the maximum $\eta_{diff} = 0.0228$ appears at $\beta = 0.23$. For a low I_r , η_{diff} is negative, increase β will reduce η_{diff} . This can be explained as the same reason in Section 6.5.1.

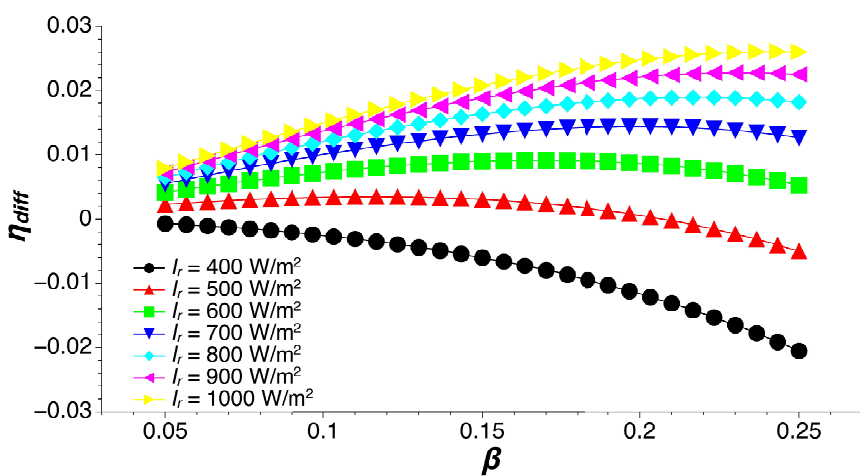


图 6-5 Curve fits of efficiency difference η_{diff} versus β

6.5.3 Effects of flow type

Flow type between heating and cooling streams can affect the efficiency of Stirling engine array. Parallel flow, compared to counterflow, leads to higher Stirling engine efficiency in the first columns of the array for lower cooling temperature, while lower Stirling engine efficiency in the last columns for higher cooling temperature.

表 6.4 Results of Stirling engine array with two different flow types

x	Parallel flow				Counterflow			
	$T_{1,i}$	$T_{2,i}$	P_{sea}	η_{sea}	$T_{1,i}$	$T_{2,i}$	P_{sea}	η_{sea}
	K	K	W	-	K	K	W	-
1	1073.15	327.17	5000	0.3648	1073.15	348.09	4867	0.3601
2	1022.38	329.80	4630	0.3599	1023.25	345.48	4541	0.3562
3	974.35	332.29	4280	0.3544	975.82	343.00	4230	0.3520
4	928.90	334.65	3949	0.3485	930.75	340.65	3934	0.3474
5	885.91	336.88	3635	0.3419	887.94	338.42	3654	0.3424
6	845.26	339.00	3338	0.3347	847.28	336.29	3387	0.3370
7	806.82	341.00	3057	0.3269	808.69	334.28	3134	0.3312
8	770.49	342.91	2792	0.3184	772.06	332.37	2894	0.3248
9	736.16	344.71	2541	0.3090	737.31	330.55	2666	0.3180
10	703.75	346.43	2304	0.2989	704.37	328.82	2450	0.3106

Table 6.4 shows the different results of the two flow types. The fit curves of temperature series of the heating and cooling fluids and the efficiency of Stirling engines in different columns are shown in Figure 6-6 and 6-7.

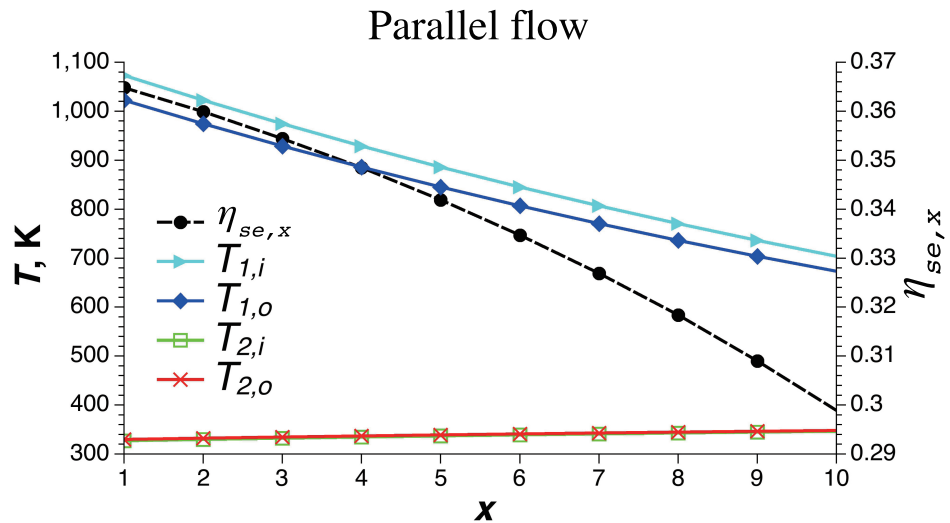


图 6-6 Parallel flow: Temperature series of two fluids and efficiency of Stirling engines in column x

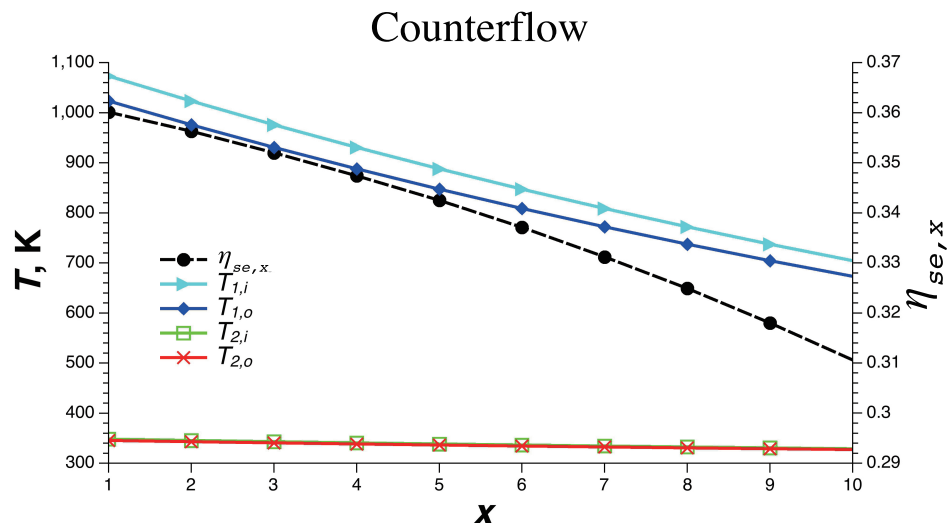


图 6-7 Counterflow: Temperature series of two fluids and efficiency of Stirling engines in column x

It can be concluded that the temperature increment of cooling fluid is much smaller than the temperature decrement of heating fluid due to their large difference of $c_p \dot{m}$, which leads to a small difference of overall efficiency of Stirling engine array between the two flow types.

To find out a clear difference of the two flow types, a simple model of Stirling engine array is developed with air as the heating fluid and water as the cooling fluid. $T_{1,i}, T_{1,o}, T_{2,i}, q_{1,m}$ are fixed and chosen the same values as in the cascade system. Change the value of $q_{2,m}$, and the corresponding Stirling engine array efficiency of the two flow types (η_p and η_c) can be obtained. Figure 6-8 shows the efficiency of Stirling engine array with different $q_{2,m}$ in two flow types. It can be found that counterflow has a higher efficiency than parallel flow, and with lower $q_{2,m}$ comes with higher efficiency difference.

For a system with large difference of $c_p \dot{m}$ of two fluids, that means one fluid can only achieve a small temperature rise (drop) compared to the other fluid, will lead to a small difference of two flow types. For a system with similar difference of $c_p \dot{m}$, use the counterflow can achieve a higher efficiency.

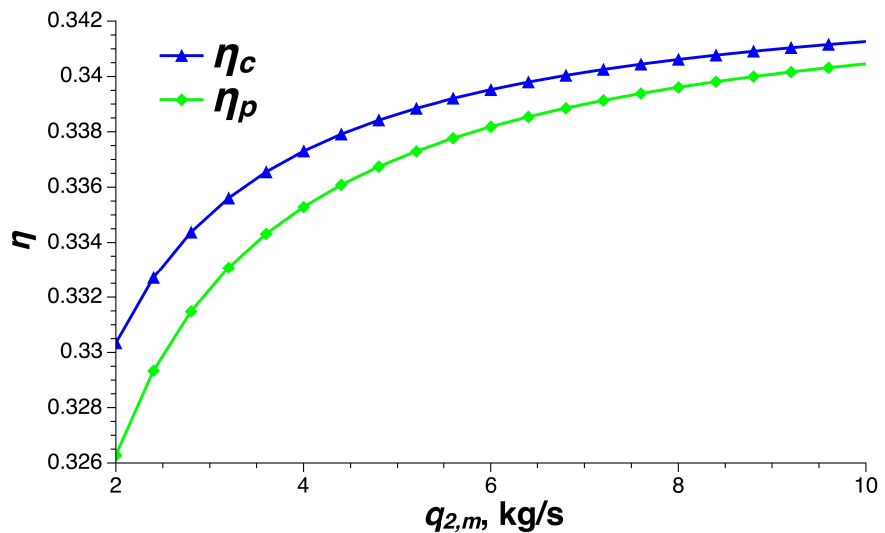


图 6-8 效率与不同 $q_{2,m}$ 的关系

6.6 Conclusion

In this chapter, an effective typical cascade system proposed in Chapter 2 is chosen for evaluation. This cascade system uses two different types of collectors and two different power generation methods. Steam Rankine cycle is applied for this system for its widely applied applications. Reasonable parameters are selected and the system model is developed. Two stand-alone systems are chosen as the comparison systems for system evaluation. They use

the same dish collectors and trough collectors of the cascade system. Simulations of the cascade system are carried out and results are compared with corresponding stand-alone systems.

Results show that I_r is the key factor to determine whether cascade system should be applied in a certain location. Compared to corresponding stand-alone systems, the cascade system can achieve a higher efficiency with high solar irradiance ($I_r > 550 \text{ W/m}^2$). The directions to increase the efficiency difference between cascade system and corresponding stand-alone systems are also considered. To design a cascade system including Stirling engine array, flow type of fluids for heating and cooling Stirling engine array is also required to be considered.

七 Experiment research on solar thermal power platform

In Chapter 3, MATLAB is used as the simulation tool to develop the models of the key components of solar thermal systems. Based on these component models, the cascade system model is developed. The mechanism of trough collector is studied. Under the condition of assumption of uniform overall heat transfer coefficient, the correlations between temperature rise, mass flow of the HTF, solar direct normal irradiance, ambient temperature and other factors were derived. The theoretical formula of the efficiency of trough collector is obtained. The heat losses of dish collector were analyzed in detail. A thermal network model of the dish receiver is established. Using classical heat transfer correlations, each temperature node of the heat network is solved and the thermal efficiency of the dish collector is obtained.

To understand the solar thermal power generation system more deeply and to validate the applicable range and error of the proposed component models, a platform includes trough concentrating collector, dish concentrating collector and ORC system was built in Wuhan. The construction of this solar thermal platform provides a good foundation for future cascade solar power generation system.

7.1 Platform introduction

Figure 7-1 shows the schematic structure of the solar thermal power platform. Three circuits, the air circuit, oil circuit and organic fluid circuit, are created by different fluids. In the air circuit, air in the environment is first compressed in the compressor, and warmed by a heater, then heated in dish receiver, then flows into the air-oil heat exchanger to provide heat for Rankine cycle and finally through the water cooling system back to the environment. In the oil circuit, the oil is first heated in the trough collector and then flows into the air-oil heat exchanger to obtain the heat provided by the air. The heated oil flows into the evaporator of the ORC system to provide heat for the ORC system, then through the pump back to the trough collector. In the organic fluid circuit, the organic fluid first absorbs the heat provided by the oil in the evaporator, then flows into the ORC turbine for expansion. After expansion,

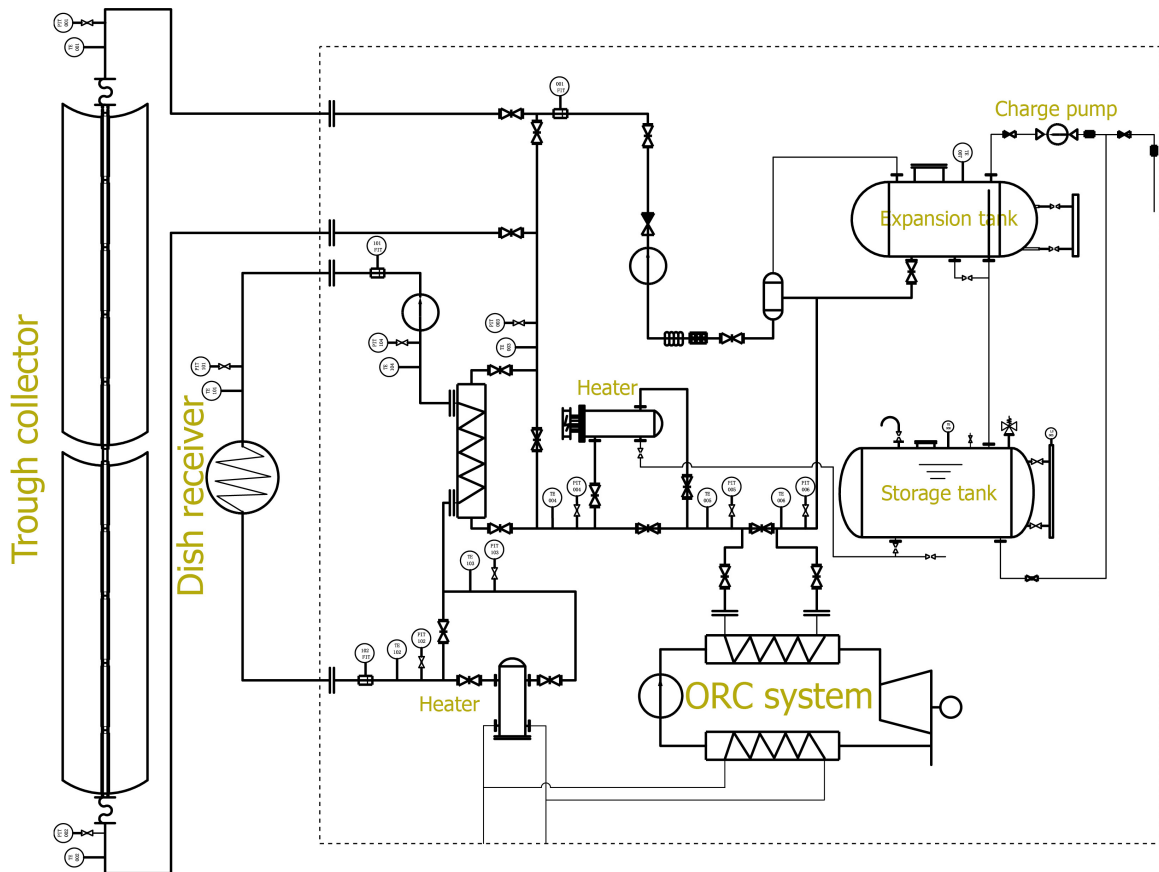


图 7-1 Schematic structure of the platform

the organic fluid flows into the regenerator to recover part of the overheating heat, then into the condenser, and back to the regenerator to reuse the rejected heat, then through the pump back to the evaporator.

The following describes key components of the platform.

7.1.1 Trough collector

The trough collector is east-west oriented due to land constrains. It is made of parabolic reflector, receiver and bracket. Figure 7-2 shows the photo of the trough collector. The reflector is 20 m long, and 2.55 m wide. The receiver is an SEIDO-I type product of Sunda-Solar Company. It consists of a glass tube and a metal black pipe, vacuum is maintained between the two to reduce heat loss. The external diameter of the glass tube is 0.11 m, and the internal diameter is 0.106 m. The external diameter of the metal tube is 0.038 m, and

the internal diameter is 0.035 m. The bracket is applied to support the reflector and receiver. Its structure is safe enough to resist common windy, stormy and snowy weather conditions. The mechanical structures for rotation, positioning and connection are simple and reliable, easy for mounting, dismounting and transportation, and convenient for operation and maintenance. Single-axis tracking system is applied for the trough collector system. The program algorithm is used for real-time automatic tracking with small tracking error. Manual mode is also an optional choice. The buttons in the control cabinet make it convenient to adjust the collector to a desired direction. In addition, it provides automatic protection and manual operation protection in case of emergency.

SINOPEC L-QD350 synthetic thermal oil is applied as the HTF of the trough collector system. Its typical physical parameters are provided from the seller.

7.1.2 Dish collector

Figure 7-3 shows the photo of the dish collector. The reflector is made of multiple curved mirrors. When the aperture is facing to the sun, each of the mirrors reflects the sunlight to the focal point. A self-designed receiver is mounted at the focal point of the dish reflector, as shown at top of the photo in Figure 7-3. The key parameters of the dish collector are listed in Table 7.1.

表 7.1 Key parameters of the designed dish collector

Parameter	Value	Parameter	Value	Parameter	Value
d_{cav}	0.45 m	ϵ_{insu}	0.6	θ_{dc}	20°
δ_{insu}	0.11 m	α_{cav}	0.87	γ	0.97
dep_{cav}	0.45 m	δ_a	0.002 m	$\eta_{shading}$	1
d_{ap}	0.25 m	$d_{i,1}$	0.07 m	ρ	0.91
λ_{insu}	0.06 W/(m · K)	A_{dc}	23.3 m ²		

The YYGN-GR-1A automatic two-axis tracking control system is used for the dish collector system. Both algorithm tracking method and sensor tracking method are applied for the tracking system. Usually, at the beginning of the focusing process, manual mode is ap-

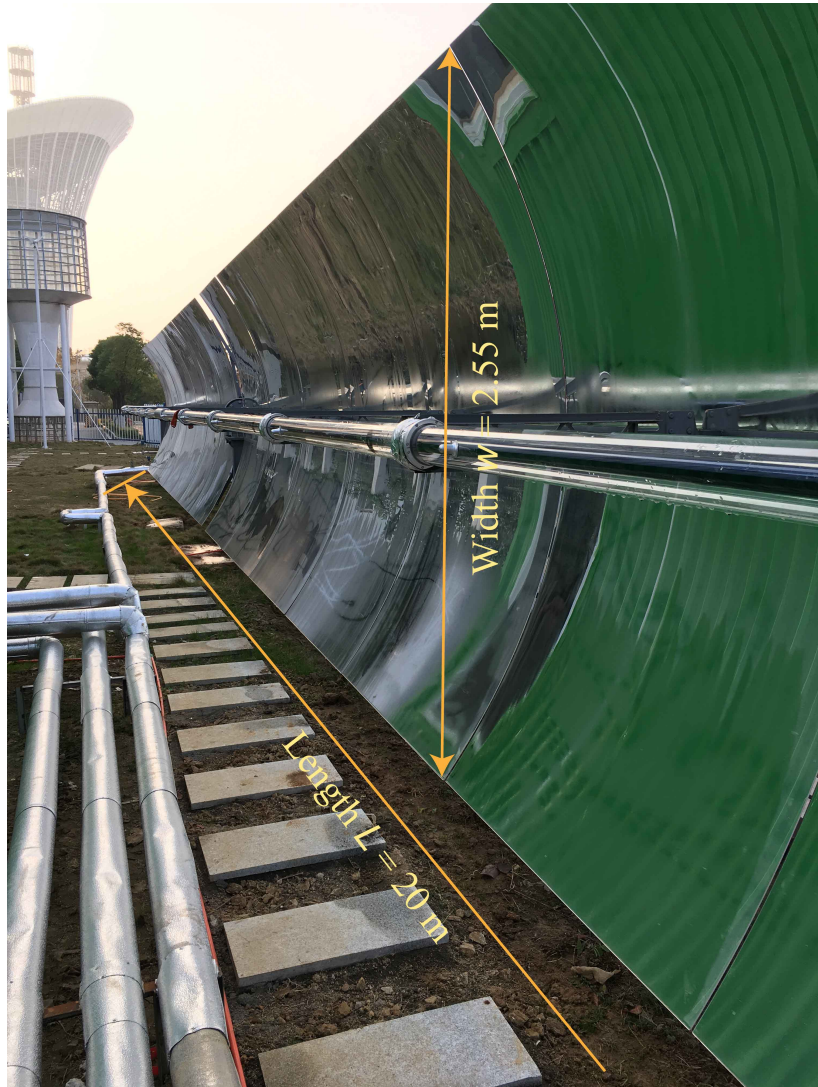


图 7-2 Trough collector of the platform

plied to roughly rotate the collector towards the sun. Then switch to the automatic mode to precisely face to the sun. And the algorithm tracking method will take over and keep tracking the sun. This provides a more reliable tracking system with tracking error of less than 0.2° without cumulative error. The control cabinet of the dish collector provides mechanical, electrical and other optional controls. It also monitors the wind speed and provides the function of set maximum wind speed for safety. When the wind is too strong, it will rotate the collector to a safe angle (facing the zenith).



图 7-3 Dish collector of the platform

7.1.3 ORC system

Hot oil (heated by the trough collector and/or the heater) is supplied to the ORC system. In the hot loop, input temperature of the supplied oil is 180°C, and output temperature is 160°C. Flow rate of 0.44 kg/s is required to reach the nominal output gross power 1.5 kW. In the cold loop, input temperature of tap water is 30°C, and output temperature is 37°C. The water flow rate is about 0.83 kg/s.

Figure 7-4 shows photos of the ORC system. It is made of evaporator, high speed ORC turbine, generator, regenerator, condenser, organic working medium pump, electrical control

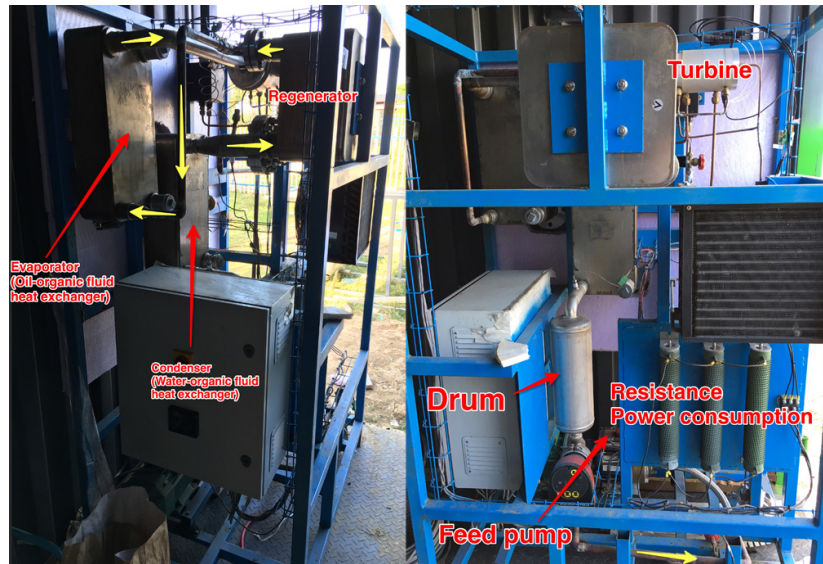


图 7-4 ORC system of the platform

cabinet and the connection pipes.

The control cabinet provide a touch screen to control the ORC system. Both automatic mode and manual mode are provided. In automatic mode, all the start up work and shut down work will be completed by procedure automatically. In manual mode, you can manually set the parameters such as the speed of the organic fluid pump to provide precise control of the system.



图 7-5 Control screen of the ORC system

7.1.4 Piping system

Piping system provides the basis for fluid flow and heat exchange. Plus, it provides thermal insulation for hot fluids. Meters, pumps, valves, tanks and heaters are arranged in the piping system to maintain the normal and orderly operation.

Two heaters are used in the platform to increase the temperatures of the fluids (air and oil) to reach the experiment requirements when the solar irradiance is not enough. Both heaters have temperature sensors to maintain the temperatures of the outlet fluids by changing the power.

7.2 Experiments

In order to test the performance of the platform and validate the proposed models, relevant experiments were carried out.

7.2.1 Trough collector experiment

7.2.1.1 Experiment purpose

The purpose of the experiment is to study the effects of solar irradiance, flow rate, inlet temperature of the working fluid on the thermal performance of the collector, and to validate the trough collector model established in Section 3.1.1.

7.2.1.2 Experiment steps

The operation steps are as follows,

- (1) Complete the preparation work. Ensure that the devices and components are all properly connected and can work normally.
- (2) Initialize the solar radiometer. Adjust the direction of the solar radiometer to get the normal irradiation value, make sure the light spot passing through the tube falls in the designed position.
- (3) Open the valves in the oil circuit, then turn on the oil pump.
- (4) Turn on the motor of the trough collector tracking system. Synchronize the time of the tracking system, and turn on the automatic mode to make the trough system tracking the sun automatically.

- (5) Adjust the parameters to meet the designed conditions. When the data is stable, record and save the data collected by the data acquisition system.
- (6) Finish the experiment when all the design conditions have been tested.
- (7) Rotate the trough collector to face towards the horizontal position on the control panel.
Turn off the motor when the trough collector is ready in place.
- (8) Turn off the oil pump.

7.2.1.3 Experiment cases

Considering the uncontrollability and continuity of the direct normal irradiance (DNI) in a clear day, when DNI is a control variable, solar irradiance values can not be controlled as design values and should be measured values. When DNI is required to be a constant, total experiment time should be limited to reduce the impact of DNI variation.

表 7.2 Designed cases of the solar trough system

Case	DNI (W/m ²)	Flow rate (kg/s)	Inlet temperature (K)
1-10	Live values	0.2	433.2
11	Live value	0.1	433.2
12	Live value	0.2	433.2
13	Live value	0.3	433.2
14	Live value	0.4	433.2
15	Live value	0.5	433.2
16	Live value	0.2	413.2
17	Live value	0.2	423.2
18	Live value	0.2	433.2
19	Live value	0.2	443.2
20	Live value	0.2	453.2

In table 7.2, Case 1 to Case 10 are completed at different times of a day or in different days. Case 11 to Case 15 are required to be completed within half an hour. It is worth noting

that, only 5 cases (Case 16 to Case 20) are designed with small temperature increment for the inlet temperature investigation due to the slow heating process of the oil heater. And the 5 cases are required to be completed within an hour.

7.2.1.4 Data processing method

The specific heat of the oil is given as: when $T = 373.15^\circ\text{C}$, $c_p = 2.44 \times 10^3 \text{ J}/(\text{kg} \cdot \text{K})$; when $T = 473.15^\circ\text{C}$, $c_p = 2.88 \times 10^3 \text{ J}/(\text{kg} \cdot \text{K})$. Linear interpolation method is applied, $c_p = aT + b$, where $a = 4.4 \text{ J}/(\text{kg} \cdot \text{K}^2)$, $b = 798.14 \text{ J}/(\text{kg} \cdot \text{K})$.

$$\text{The absorbed heat of the oil } Q_{abs} = \int_{T=T_i}^{T=T_o} c_p \dot{m} dT = \frac{1}{2} a(T_o^2 - T_i^2) \dot{m} + b(T_o - T_i) \dot{m}.$$

The thermal efficiency of the trough collector

$$\eta_{tc} = \frac{Q_{abs}}{I_r w_{tc} L_{tc}} \quad (7.1)$$

To validate the simulation model, Equation (3.4) is required to be checked. In the simulation model,

$$\tilde{T}_o = T_{amb} + \frac{q''}{U(T_{abs})} + \exp\left(-\frac{U(T_{abs})\pi d_o L}{\dot{m} \tilde{c}_p}\right) (T_i - T_{amb} - \frac{q''}{U(T_{abs})}) \quad (7.2)$$

where T_{abs} is replaced by $(T_i + T_o)/2$ (T_i and T_o are the measured values of inlet temperature and outlet temperature), \tilde{c}_p is the average specific heat obtained from $(T_i + T_o)/2$, $U(T_{abs})$ is obtained from^[104]

$$U(T_{abs}) = 0.687257 + 0.001941(T_{abs} - T_{amb}) + 0.000026(T_{abs} - T_{amb})^2 \quad (7.3)$$

$$q'' = \frac{I_r w_{tc} \rho \gamma \tau F_e K(\theta)}{\pi d_o} \quad (7.4)$$

$$K(\theta) = \cos \theta + 0.000884\theta - 0.00005369\theta^2 \quad (7.5)$$

So $\widetilde{\eta_{tc}}$ from the simulation results can be obtained for comparison with the one in Equation (7.1) obtained from experiment.

$$\widetilde{\eta_{tc}} = \frac{\dot{m} \tilde{c}_p (\tilde{T}_o - T_i)}{I_r w_{tc} L_{tc}} \quad (7.6)$$

7.2.2 Dish collector experiment

7.2.2.1 Experiment purpose

The purpose of the experiment is to study the effects of solar irradiance, flow rate, inlet temperature of the working fluid on the thermal performance of the collector, and to validate the dish receiver model established in Section 3.1.2.

7.2.2.2 Experiment steps

The operation steps are as follows,

- (1) Complete the preparation work. Ensure that the devices and components are all properly connected and can work normally.
- (2) Initialize the solar radiometer. Adjust the direction of the solar radiometer to get the normal irradiation value, make sure the light spot passing through the tube falls in the designed position.
- (3) Turn on the water cooling system.
- (4) Open the valves of the inlet and outlet of the air circuit, then turn on the air compressor.
- (5) Use manual mode to rotate the collector toward the sun. Then switch to the automotive mode.
- (6) Adjust the parameters to meet the designed conditions. When the data is stable, record and save the data collected by the data acquisition system.
- (7) Finish the experiment when all the designed conditions have been tested.
- (8) Rotate the collector to the up most position (facing the zenith). Turn off the compressor, turn off the outlet and inlet valves, turn off the water cooling system.

7.2.2.3 Experiment cases

In Table 7.3, Case 1 to Case 10 are completed at different times of a day or in different days. Case 11 to Case 15 are required to be completed within half an hour. Case 16 to Case 20 are required to be completed within an hour.

7.2.2.4 Data processing method

Known the pressure ($p = 4 \times 10^5$ Pa) and the measured temperature, the inlet enthalpy (h_i) and outlet enthalpy (h_o) of the air can be obtained.

表 7.3 Designed cases of the solar dish system

Case	DNI (W/m ²)	Flow rate (kg/s)	Inlet temperature (K)
1-10	Live values	0.03	423.2
11	Live value	0.01	423.2
12	Live value	0.02	423.2
13	Live value	0.03	423.2
14	Live value	0.04	423.2
15	Live value	0.05	423.2
16	Live value	0.03	383.2
17	Live value	0.03	403.2
18	Live value	0.03	423.2
19	Live value	0.03	443.2
20	Live value	0.03	463.2

The absorbed heat of the air $Q_{abs} = \dot{m}(h_o - h_i)$.

The thermal efficiency of the dish collector $\eta_{dc} = \frac{Q_{abs}}{I_r A_{dc}}$.

To validate the simulation model in Section 3.1.2, the thermal network of dish receiver (see Figure 3-4) are solved from the equations in Section 3.1.2.

The simulation efficiency of the dish collector $\widetilde{\eta_{dc}} = \frac{Q_{dr,1}}{I_r A_{dc}}$.

7.3 Result analysis

7.3.1 Trough collector experiment result analysis

Influences of solar irradiance, flow rate and inlet temperature of the working fluid on the collector thermal performance are concerned.

表 7.4 Experiment results of Case 1 to Case 10 of the trough collector

Case	DNI (W/m ²)	\dot{m} (kg/s)	T_i (K)	T_o (K)	T_{amb} (K)
1	353	0.2	433.2	452.9	277.8
2	408	0.2	433.2	456.2	278.0
3	464	0.2	433.2	459.4	278.2
4	476	0.2	433.2	460.2	278.4
5	497	0.2	433.2	461.3	278.4
6	508	0.2	433.2	462.0	278.6
7	553	0.2	433.2	464.6	278.6
8	610	0.2	433.2	467.9	278.8
9	637	0.2	433.2	469.3	278.8
10	652	0.2	433.2	470.2	278.9

7.3.1.1 Influence of I_r

Tested results of Case 1 to Case 10 are listed in Table 7.4. It is noteworthy that due to the uncontrollability and variability of solar radiation intensity, the measured values of solar irradiance are not evenly distributed. Figure 7-6 shows the influence of solar irradiance on the thermal efficiency of the trough collector. Simulation results are also included. The simulation parameters are set to be the same as the experiment.

It can be found that both the experimental data and simulation results show the same trend of thermal efficiency and solar irradiance. The thermal efficiency increases with DNI. There exists small deviations between the experimental data and simulation results, between 0% to 1%.

7.3.1.2 Influence of \dot{m}

Tested results of Case 11 to Case 15 are listed in Table 7.5. Figure 7-7 shows the influence of inlet flow rate on the thermal efficiency of the trough collector. The data points on the figure are collected within a short time, so the irradiance can be regarded as unchanged.

It can be found that higher flow rate leads to higher efficiency. This is obvious for

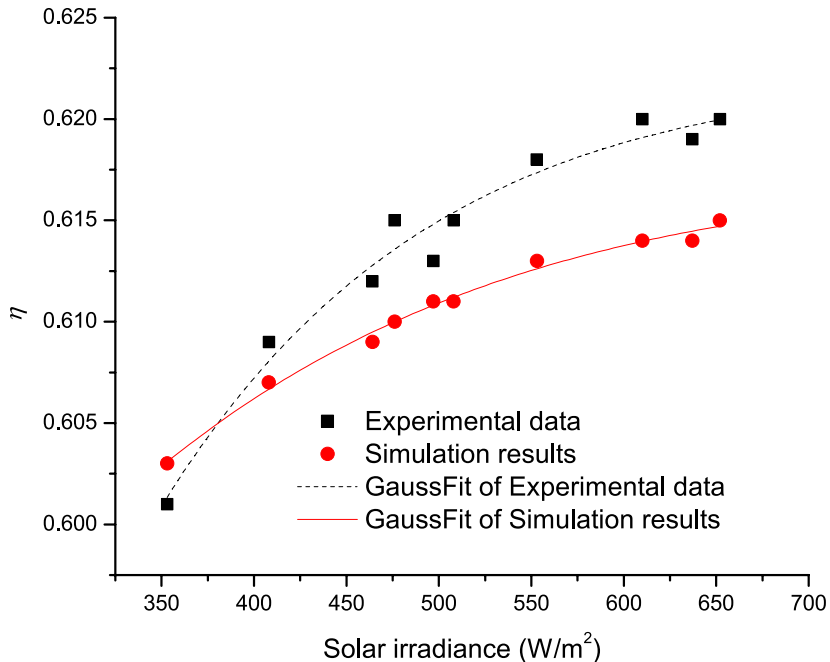


图 7-6 影响太阳辐照度对热效率的影响

表 7.5 Case 11 to Case 15 的实验结果

Case	DNI (W/m ²)	\dot{m} (kg/s)	T_i (K)	T_o (K)	T_{amb} (K)
11	612	0.1	433.2	501.0	286.3
12	615	0.2	433.2	468.2	286.4
13	615	0.3	433.2	456.7	286.6
14	614	0.4	433.2	451.2	286.7
15	612	0.5	433.2	447.6	286.7

更高的流速带走更多的热量，导致接收器温度分布降低，从而减少热损失。实验数据和模拟结果在很大程度上是一致的。存在一些偏差，介于 0.4% 到 0.9% 之间。模拟效率低于对应的实验效率。这可能意味着，热损失系数 U 和 T_{abs} （见方程 7.3）是为 LS-3 型集热器设计的，而不是理想的。

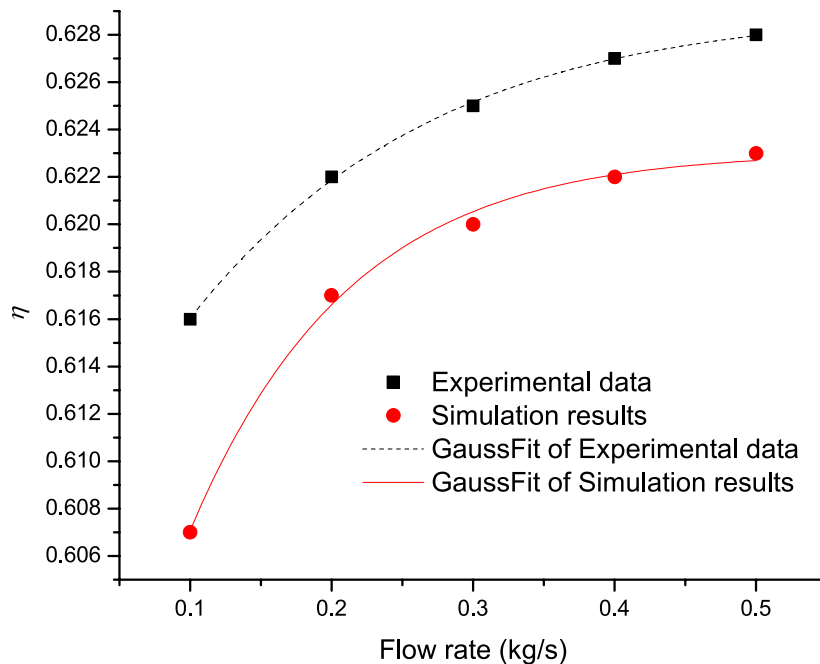


图 7-7 影响进水流量对热效率的影响

trough collector product used in the platform. Future tests will provide more data for a more accurate correlation for the SEIDO6-I product.

7.3.1.3 影响 T_i

表 7.6 实验结果 Case 16 到 Case 20 的槽型集热器

Case	DNI (W/m ²)	\dot{m} (kg/s)	T_i (K)	T_o (K)	T_{amb} (K)
16	616	0.2	413.2	449.7	289.5
17	614	0.2	423.2	458.8	288.3
18	610	0.2	433.2	467.9	288.7
19	618	0.2	443.2	477.7	288.9
20	615	0.2	453.2	486.8	286.3

Tested results of Case 16 to Case 20 are listed in Table 7.9. Figure 7-8 shows the influ-

ence of inlet flow rate on the thermal efficiency of the trough collector.

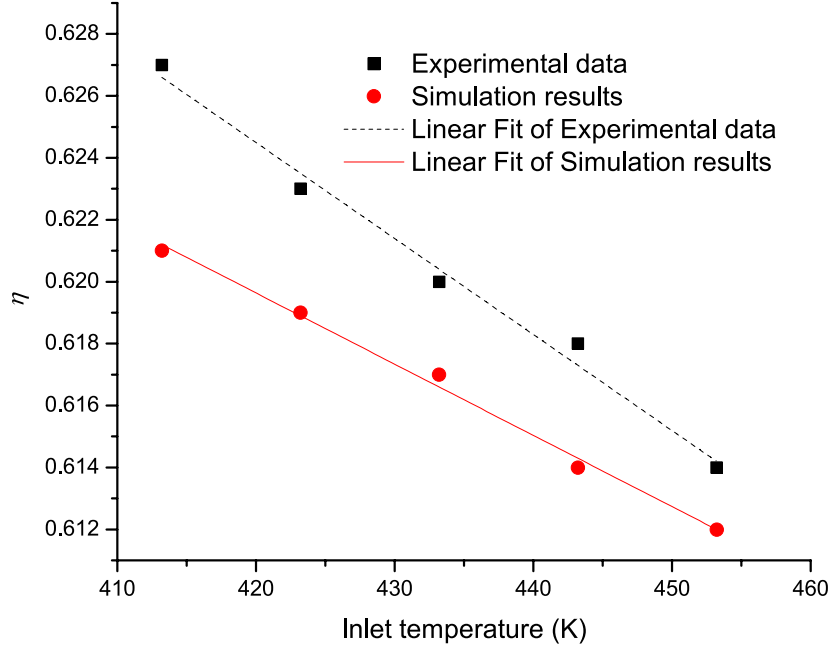


图 7-8 Influence of inlet temperature on the thermal efficiency

Both the experimental data and simulation results show that, higher inlet temperature leads to lower efficiency. This is obvious for higher inlet temperature leads to higher receiver temperature distribution and hence more thermal losses. Small deviations also exist between the experimental data and simulation results, between 0.7% to 1.5%. The simulation efficiency is lower than corresponding experimental efficiency. This can be interpreted as the same reason of inaccurate thermal loss coefficient U .

7.3.2 Dish collector experiment result analysis

Influences of solar irradiance, flow rate and inlet temperature of the working fluid on the collector thermal performance are concerned.

7.3.2.1 Influence of I_r

Tested results of Case 1 to Case 10 are listed in Table 7.7. It is noteworthy that the measured values of solar irradiance are not evenly distributed due to the uncontrollability and variability of solar radiation intensity. Figure 7-9 shows the influence of solar irradiance

表 7.7 Experiment results of Case 1 to Case 10 of the dish collector

Case	DNI (W/m ²)	\dot{m} (kg/s)	T_i (K)	T_o (K)	T_{amb} (K)
1	303	0.03	423.2	552.1	282.1
2	358	0.03	423.2	576.4	282.5
3	414	0.03	423.2	602.3	283.2
4	426	0.03	423.2	607.5	283.4
5	512	0.03	423.2	646.0	285.0
6	596	0.03	423.2	682.7	287.4
7	620	0.03	423.2	692.4	289.2
8	641	0.03	423.2	701.5	289.5
9	658	0.03	423.2	708.7	289.4
10	683	0.03	423.2	719.4	289.5

on the thermal efficiency of the dish collector. Simulation results are also included. The simulation parameters are set to be the same as the experiment.

It can be found that the thermal efficiency increases with solar irradiance when DNI is less than 600 W/m². When DNI is larger than 600 W/m², higher irradiance leads to higher wall temperature and hence more radiation loss, which jeopardizes the thermal efficiency when solar irradiance increases. The discrepancy of the experimental data and simulation data may be interpreted for the insulation condition. The out wall temperature of the insulation layer is higher than expected, which proves that the isolation condition is not good enough.

To clearly show the influence of higher DNI, a simulation of the dish collector model was carried out. The inlet air temperature is set to be 423.2 K, and the flow rate is set to be 0.03 kg/s. The environment temperature was set to be 283.2 K and the wind speed is set to be 0.4 m/s. The simulation results are shown in Figure 7-10. It can be found that there exists an optimum DNI for a specific receiver to achieve the highest thermal efficiency. For the receiver used in the platform, the optimum DNI is about 600 W/m².

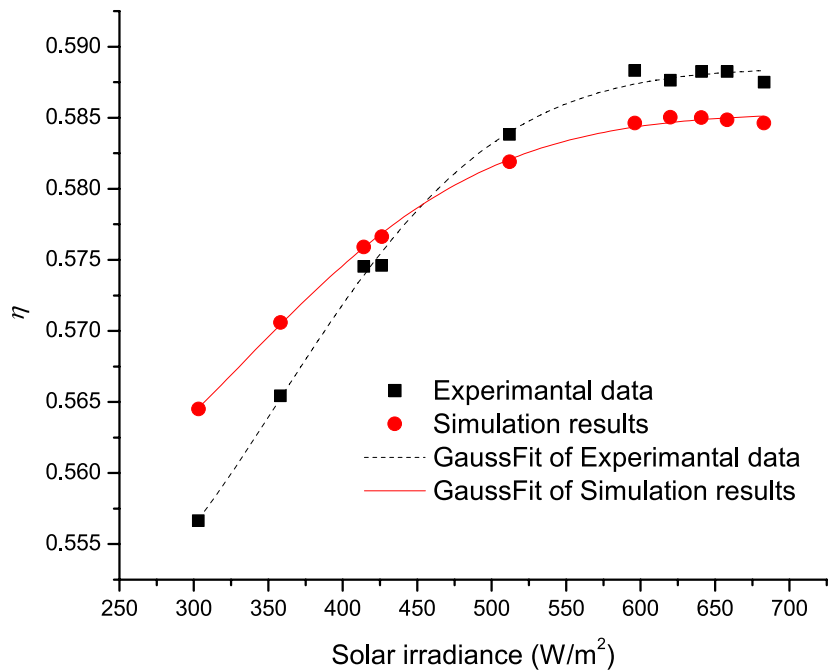


图 7-9 影响太阳辐照度对热效率的影响

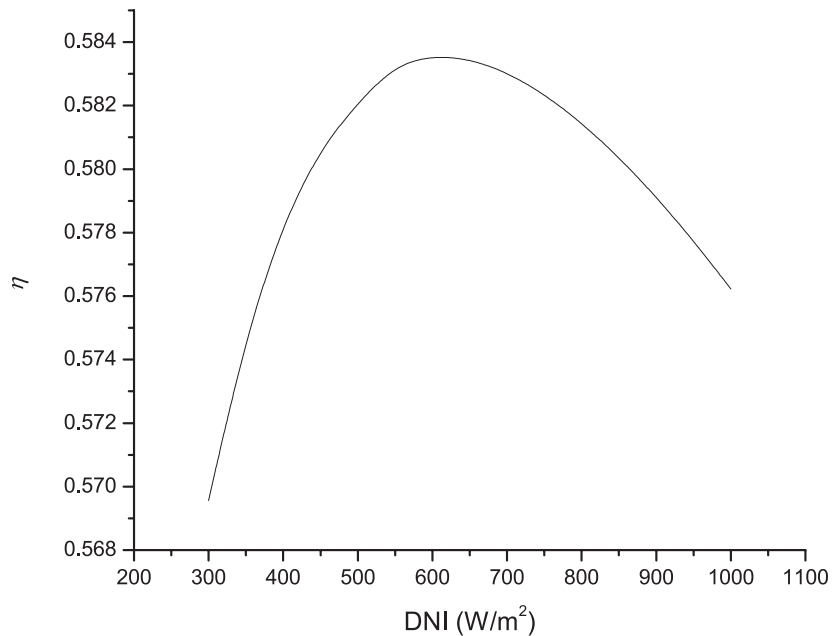


图 7-10 模拟结果影响太阳辐照度对热效率的影响

7.3.2.2 Influence of \dot{m}

Tested results of Case 11 to Case 15 are listed in Table 7.8. Figure 7-11 shows the influence of inlet flow rate on the thermal efficiency of the dish collector. The data points on

表 7.8 Experiment results of Case 11 to Case 15 of the dish collector

Case	DNI (W/m^2)	\dot{m} (kg/s)	T_i (K)	T_o (K)	T_{amb} (K)
11	613	0.01	423.2	950.7	286.3
12	615	0.02	423.2	783.9	286.4
13	616	0.03	423.2	691.8	286.6
14	614	0.04	423.2	634.9	286.7
15	613	0.05	423.2	597.8	286.7

the figure are collected within a short time, so the irradiance can be regarded as unchanged.

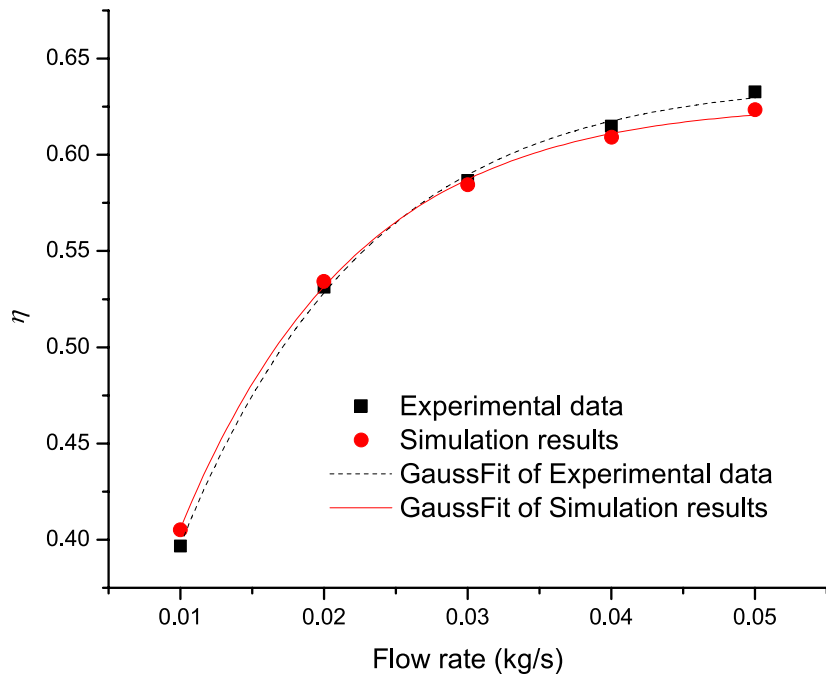


图 7-11 Influence of inlet flow rate on the thermal efficiency

It can be found that higher flow rate leads to higher efficiency. This is obvious for higher flow rate takes more heat away from the receiver, leads to lower temperature distribution and hence less thermal losses. The experimental data and simulation result are in good agreement.

7.3.2.3 Influence of T_i

表 7.9 Experiment results of Case 16 to Case 20 of the dish collector

Case	DNI (W/m ²)	\dot{m} (kg/s)	T_i (K)	T_o (K)	T_{amb} (K)
16	616	0.03	383.2	661.9	289.0
17	615	0.03	403.2	676.4	288.8
18	612	0.03	423.2	690.6	288.8
19	617	0.03	443.2	707.8	288.9
20	615	0.03	463.2	722.2	288.9

Tested results of Case 16 to Case 20 are listed in Table 7.9. Figure 7-12 shows the influence of inlet flow rate on the thermal efficiency of the dish collector.

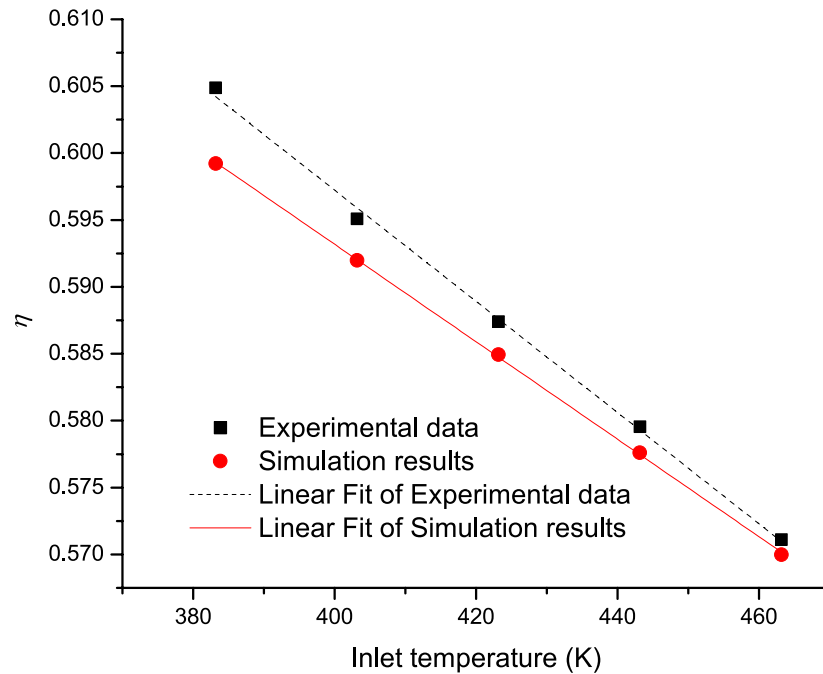


图 7-12 Influence of inlet temperature on the thermal efficiency

It can be found that higher inlet temperature leads to lower efficiency. This is obvious

for higher inlet temperature leads to higher temperature distribution and hence more thermal losses. The experimental data and simulation result are in good agreement.

7.4 Conclusion

The solar thermal power platform is a good start for the cascade solar thermal system. This chapter introduces the components and the circuits of the platform. According to the features of solar irradiance, special experiment cases are designed to investigate the impact of different factors on the system performance. Experiment steps are carefully arranged. Tests of the trough collector and the dish collector are carried out and the experimental results are collected for analysis.

The influence of solar irradiance, flow rate and inlet temperature of the working fluid on the performance of the collector model is investigated. The established trough collector model and dish collector model are validated by the experimental data.

The analysis of experimental data and simulation results shows that

- (1) The thermal efficiency of trough collectors is between 60.1% and 62.8% and the thermal efficiency of dish collectors is between 39.7% and 63.3% under the experimental conditions.
- (2) With regard to the effect of the considered factors on the performance of the collectors, the experimental data and the simulation results have the same trend. Higher working fluid flow rate leads to higher thermal efficiency, while higher working fluid inlet temperature leads to lower thermal efficiency.
- (3) For a specific dish receiver, there exists an optimum DNI to obtain the highest thermal efficiency.
- (4) The discrepancy of the experimental data and simulation results of the trough collector indicates that the thermal loss coefficient used in the modeling process is not ideal for the trough product used in the platform. It needs to be revised in the future.
- (5) The discrepancy of the experimental data and simulation results of the dish collector indicates that the thermal insulation of the dish collector needs to be inspected and strengthened.

八 Summaries and outlooks

8.1 Summaries

This chapter is needed to conclude the overall goals of our research. Considering the advantages and disadvantages of the existing solar thermal power generation technologies, a novel idea of energy cascade collection and energy cascade utilization for solar thermal power generation was put forward. Different types of collectors and thermodynamic cycles were used in the cascade system. The research of the cascade system was carried out with the selection of the system topology, the construction of the system model, the optimization of the system model and parameters, and the comparison with the independent system. The main works are concluded as follow:

- (1) Topological structures of cascade solar thermal power generation systems were proposed. According to the analysis of thermodynamic characteristics and the operating behavior of each component in the system, reasonable arranged topological structures of cascade systems were proposed. These systems use different thermodynamic cycles to harness the energy of different temperature zones. A reasonable cascade generation system can make full use of the mechanism models of power generation system to provide a basis for a more efficient cascade solar thermal generation system. In this thesis, several schemes of feasible topological structures of solar thermal cascade system were set up according to the mechanism model of each component. After system evaluation, parameter selection, preliminary calculation and scheme comparison, two representative typical schemes were determined. In one scheme, both steam Rankine cycle and Stirling cycle are used for power generation. Condensation water of the Rankine cycle is used to cool the hot end of the Stirling engines to recover the released heat. In the other scheme, multiple organic Rankine cycles are used for power generation. Condensation heat of upper cycle is absorbed by lower cycle for energy cascade utilization.
- (2) Mechanism models were established for the components of solar thermal power generation system. The mechanism mathematical models were developed according to the physical equations and operation features of the target object. The key components

in the system, such as collectors, steam generating system, steam turbine and Stirling engine, have been analyzed for detailed modeling. The mathematical model of each component is a model verified by classical theory or a large number of experimental data, which is the basic of a cascade solar thermal power generation system model. Heat loss models were established for the receivers of trough collector and dish collector. For Stirling engine, based on reasonable simplification and hypothesis, a model of the Stirling machine considered various losses and irreversibilities was developed. The component models using object-oriented method were developed in MATLAB. It makes full use of inheritance and polymorphism to ensure both independence and relevance of the components.

- (3) A solar thermal power generation system design software was designed and the cascade solar thermal generation system models were developed. System models of the selected cascade solar thermal thermal generation systems were established based on the model of each component in the systems. The object-oriented features of inheritance, combination and polymorphism were used for the model development. The variation rules and performance indexes of main parameters under the coupling of external and internal factors were studied. The change mechanism was studied and the calculation method of its performance characteristics was established. After component layout, parameter setting and environment selection, the thesis completed the system development of each system scheme, and finally developed the simulation system of cascade solar thermal generation based on MATLAB with the copyright of independent computer software. The system components are relatively independent, easy to replace or improve the component model; calculation results of the system model exist in all objects of the system, so that the key parameters of each component can be clearly and conveniently viewed.
- (4) Simulation and optimization of cascade solar thermal power generation system model were carried out. Based on the research of performance characteristics of cascade solar thermal power generation system, the system was optimized and the structure was rebuilt. In particular, by analyzing the steam generating system of the system, a staged heating method was proposed, which can reduce the temperature difference in the steam generating system during steam generation by changing the mass flow rate of the heat transfer oil and effectively reduce exergy loss during the process. It helps

to improve the efficiency of the whole system. Considering the features of the Stirling engines in the cascade system, five basic arrangements of Stirling engine array were summarized, and the differences of Stirling engine array efficiency and output power under various layouts were analyzed. The best arrangement of Stirling units was given under the condition of given fluid of cold and heat sources.

- (5) Operating parameters of cascade solar thermal power generation system were optimized. According to the specific structure of the program and operation mode, the appropriate stand-alone systems for comparative analysis was selected for performance comparison. Analysis of the influence of various parameters on the efficiency difference between cascade system and its corresponding stand-alone systems was conducted. The results show that cascade solar thermal power generation system has higher overall solar-to-electric conversion efficiency under certain parameter conditions than its corresponding independent system. Under the condition of direct normal irradiance of 700 W/m^2 and dish collector outlet air temperature of 800°C , the proposed cascade solar thermal power generation system is 5.2% more efficient than its corresponding stand-alone system.
- (6) A solar thermal power generation test platform was built, and the relevant experimental work was carried out. Special experiment cases considering the features of solar irradiance were designed to investigate the impact of different factors on the system performance. The influences of solar irradiance, flow rate and inlet temperature of the working fluid on the performance of the collectors were investigated. The analysis of experimental data and simulation results shows that, under the relevant test conditions, the thermal efficiency of trough collectors is between 58% and 64%, and that of trough collectors is between 63% and 68%. The experiment also validated the established trough collector and dish collector models.

8.2 Innovations

- Usage of different types of collectors and different thermodynamic cycles in one cascade system is proposed in this research. In this way, the working characteristics of different types of solar collectors and thermal cycles can be effectively utilized to overcome the drawbacks of traditional solar thermal power systems. This may provide a new feasible technology for lower cost, higher efficiency, large-scale solar thermal power generation.
- An air-water heat exchanger is applied in the cascade system to increase the temperature of the main steam temperature of the Rankine cycle. This provides a new way to overcome the shortcoming of the upper temperature limit of heat transfer oil in traditional solar trough systems, which helps to achieve higher Rankine cycle efficiency.
- Condensate of Rankine cycle is used to cool the Stirling engine. Rejected heat of the Stirling cycle can be reused by Rankine cycle, which helps to improve the overall system efficiency.
- Multistage exergy loss reduction system is applied to reduce the temperature difference between oil and water in the steam generating system. The solar field can be divided into three independent sectors according to different states (vapor, vapor-liquid two phase, liquid) of water in the steam generating system. This also provides a new space for different types of solar collector technologies applied in different solar fields. For example, linear Fresnel reflectors or flat collectors can be applied for the preheating solar field to reduce costs; molten salt can be used as heat transfer fluid in the superheating solar field to increase the main steam temperature of the Rankine cycle.
- Influence of the arrangement of Stirling engine array in the cascade system is analyzed. In order to investigate the influence of connection types on SEA performance, five basic connection types of SEA were summarized according to the direction-irrelevant feature of Stirling engine. After analyzing different factors on the performance of SEA, it is found that given heating and cooling fluids, using serial flow is the best choice for the connection type of an SEA.

8.3 Outlooks

In this research, effective topologies of the proposed cascade system were designed, models of the systems developed based on the detailed component models, simulation of the cascade system and corresponding stand alone systems were carried out and the results were analyzed. However, there are many points valuable for further research.

- Multi-stage exergy loss reduction system deserves more attention for its application of different kinds of collectors.
- Series connection of different collectors, such as flat plate and parabolic trough collectors, needs to be further studied to reduce the cost of solar power system.
- Economical analysis of the cascade system is required for the implement of the technology.
- Stirling engines are required for the platform to investigate the cascade utilization of solar energy.

致 谢

In 2004, I came to Huazhong University of Science and Technology as an undergraduate student. Now, I am over 30. The completion of the doctoral dissertation indicates that my student life here is coming to an end. Although I had discouraged days in the unforgivable life, when I staggering to leave the land that accomplished my grown up years, I am grateful for all the hardships and joys I have experienced. The full harvest of both academic and life will change my life journey.

You miss a place because you miss the people there. Special thanks for professor Huang Shuhong, I learned a lot during those years being with you. I have been deeply infected by your academic attitude, working spirit and personal charisma. Your unique academic insight and acute academic ideas always inspired me.

After he past away, I dreamed about my tutor several times, especially when I was depressed. Recalling your teachings and encouragements, I always re-establish my confidence to overcome the difficulties. Face to face learning is a collection of my memory. Professor's firm academic enthusiasm will continue to guide me.

Many thanks to the teachers who provide guidances and helps in these years. I offer my thanks to Professor Gao Wei, his elegant temperament and broad mind set up a good example for personal relationship and learning approaches. I would like to thank Associate Professor Zhang Yanping for urging me to study and write from time to time, paying close attention to the progress of the papers, and giving many timely wit directions. Special thanks for professor Inmaculada Arauzo, I am lucky enough to follow you to University of Zaragoza to open a new academic perspective. Your easy-going temper, warm attitude make my life in Spain warm and fulfilling. Your rigorous spirit and deep insight influenced me a lot. I also show my thanks to Teacher He and Yang, they concerned about me and helped me. The completion of my study comes with the generous guidance and encouragement of the teachers.

In the academic team, I was fortunate to meet Lv Fangming, Wang Jizhou. We learned a lot from each other and created precious memories. In the days with Rahul and Daniel, I improved my English communication ability and writing skills.

Finally, I thank my family for their understanding and support. I am grateful to my parents for their hard work and strong support. Thank you, my wife, after our daughter

Tongtong was born, you carried the burden of taking care of this little life. Thank you, Tongtong, your cleverness and cuteness are the flavors of my life and they always make me full of power.

Time to say goodbye. This will be a new starting point for my life. I will stay true to my mission, follow my heart, and manage a new life with gratitude and expectations.

Zhang Cheng

December 14, 2017

参考文献

- [1] Babaelahi M, Sayyaadi H. A new thermal model based on polytropic numerical simulation of Stirling engines. *Applied Energy*, 2015, 141:143 – 159.
- [2] MARTINI W R. Stirling engine design manual, 2nd edition. Technical report, Martini Engineering, Richland, WA (USA), 1983.
- [3] International Energy Agency (2014). http://www.iea.org/publications/freepublications/publication/TechnologyRoadmapSolarPhotovoltaicEnergy_2014edition.pdf. Accessed: 2017-05-04.
- [4] Price H, Lupfert E, Kearney D, et al. Advances in Parabolic Trough Solar Power Technology. *Journal of Solar Energy Engineering*, 2002, 124(2):109–125.
- [5] Dudley V E, Kolb G J, Mahoney A R, et al. Test results: SEGS LS-2 solar collector. Nasa Sti/recon Technical Report N, 1994, 96(4):2506–2514.
- [6] Burkholder F, Kutscher C. Heat Loss Testing of Schott's 2008 PTR70 Parabolic Trough Receiver. May, 2009.
- [7] Reddy K, Kumar K R, Ajay C. Experimental investigation of porous disc enhanced receiver for solar parabolic trough collector. *Renewable Energy*, 2015, 77(Supplement C):308 – 319.
- [8] Li M, Xu C, Ji X, et al. A new study on the end loss effect for parabolic trough solar collectors. *Energy*, 2015, 82(Supplement C):382 – 394.
- [9] Wang J, Wang J, Bi X, et al. Performance Simulation Comparison for Parabolic Trough Solar Collectors in China. *International Journal of Photoenergy*, 2016, 2016(18):1–16.
- [10] Zou B, Yang H, Yao Y, et al. A detailed study on the effects of sunshape and incident angle on the optical performance of parabolic trough solar collectors. *Applied Thermal Engineering*, 2017, 126(Supplement C):81 – 91.
- [11] Lüpfert E, Pottler K, Ulmer S, et al. Parabolic Trough Optical Performance Analysis Techniques. *Journal of Solar Energy Engineering*, 2006, 129(2):147–152.
- [12] Xu C, Chen Z, Li M, et al. Research on the compensation of the end loss effect for parabolic trough solar collectors. *Applied Energy*, 2014, 115:128 – 139.
- [13] Huang W, Hu P, Chen Z. Performance simulation of a parabolic trough solar collector. *Solar Energy*, 2012, 86(2):746 – 755.
- [14] Padilla R V, Fontalvo A, Demirkaya G, et al. Exergy analysis of parabolic trough solar receiver. *Applied Thermal Engineering*, 2014, 67(1-2):579 – 586.
- [15] Padilla R V, Demirkaya G, Goswami D Y, et al. Heat transfer analysis of parabolic trough solar receiver. *Applied Energy*, 2011, 88(12):5097 – 5110.
- [16] Guo J, Huai X, Liu Z. Performance investigation of parabolic trough solar receiver. *Applied Thermal Engineering*, 2016, 95:357 – 364.
- [17] Behar O, Khellaf A, Mohammedi K. A novel parabolic trough solar collector model – Vali-

- dation with experimental data and comparison to Engineering Equation Solver (EES). *Energy Conversion and Management*, 2015, 106(Supplement C):268 – 281.
- [18] Hachicha A, Rodriguez I, Capdevila R, et al. Heat transfer analysis and numerical simulation of a parabolic trough solar collector. *Applied Energy*, 2013, 111:581 – 592.
 - [19] Guo J, Huai X. Multi-parameter optimization design of parabolic trough solar receiver. *Applied Thermal Engineering*, 2016, 98:73 – 79.
 - [20] Boukelia T, Arslan O, Mecibah M. ANN-based optimization of a parabolic trough solar thermal power plant. *Applied Thermal Engineering*, 2016, 107:1210 – 1218.
 - [21] Liu Q, Yang M, Lei J, et al. Modeling and optimizing parabolic trough solar collector systems using the least squares support vector machine method. *Solar Energy*, 2012, 86(7):1973 – 1980.
 - [22] Lobon D H, Valenzuela L, Baglietto E. Modeling the dynamics of the multiphase fluid in the parabolic-trough solar steam generating systems. *Energy Conversion and Management*, 2014, 78:393 – 404.
 - [23] Mohamad A, Orfi J, Alansary H. Heat losses from parabolic trough solar collectors. *International Journal of Energy Research*, 2014, 38(1):20–28.
 - [24] Guo S, Liu D, Chu Y, et al. Real-time dynamic analysis for complete loop of direct steam generation solar trough collector. *Energy Conversion and Management*, 2016, 126:573 – 580.
 - [25] Ashouri M, Vandani A M K, Mehrpooya M, et al. Techno-economic assessment of a Kalina cycle driven by a parabolic Trough solar collector. *Energy Conversion and Management*, 2015, 105:1328 – 1339.
 - [26] Bader R, Pedretti A, Barbato M, et al. An air-based corrugated cavity-receiver for solar parabolic trough concentrators. *Applied Energy*, 2015, 138:337 – 345.
 - [27] Good P, Ambrosetti G, Pedretti A, et al. An array of coiled absorber tubes for solar trough concentrators operating with air at 600°C and above. *Solar Energy*, 2015, 111:378 – 395.
 - [28] Kaloudis E, Papanicolaou E, Belessiotis V. Numerical simulations of a parabolic trough solar collector with nanofluid using a two-phase model. *Renewable Energy*, 2016, 97:218 – 229.
 - [29] Al-Sulaiman F A, Hamdullahpur F, Dincer I. Performance assessment of a novel system using parabolic trough solar collectors for combined cooling, heating, and power production. *Renewable Energy*, 2012, 48:161 – 172.
 - [30] Tan Y, Zhao L, Bao J, et al. Experimental investigation on heat loss of semi-spherical cavity receiver. *Energy Conversion and Management*, 2014, 87(Supplement C):576 – 583.
 - [31] Chaudhary A, Kumar A, Yadav A. Experimental investigation of a solar cooker based on parabolic dish collector with phase change thermal storage unit in Indian climatic conditions. *Journal of Renewable and Sustainable Energy*, 2013, 5(2):023107.
 - [32] Mawire A, Taole S H. Experimental energy and exergy performance of a solar receiver for a domestic parabolic dish concentrator for teaching purposes. *Energy for Sustainable Development*, 2014, 19:162 – 169.
 - [33] Zhu J, Wang K, Wu H, et al. Experimental investigation on the energy and exergy performance of a coiled tube solar receiver. *Applied Energy*, 2015, 156:519 – 527.

- [34] Skouri S, Bouadila S, Salah M B, et al. Comparative study of different means of concentrated solar flux measurement of solar parabolic dish. *Energy Conversion and Management*, 2013, 76:1043 – 1052.
- [35] Thirunavukkarasu V, Sornanathan M, Cheralathan M. An experimental study on energy and exergy performance of a cavity receiver for solar parabolic dish concentrator. *International Journal of Exergy*, 2017, 23(2):129.
- [36] Pavlovic S, Bellos E, Roux W G L, et al. Experimental investigation and parametric analysis of a solar thermal dish collector with spiral absorber. *Applied Thermal Engineering*, 2017, 121(Supplement C):126 – 135.
- [37] Lovegrove K, Burgess G, Pye J. A new 500m² paraboloidal dish solar concentrator. *Solar Energy*, 2011, 85(4):620 – 626. SolarPACES 2009.
- [38] Berumen C R, Benítez R R, Mendoza J L, et al. Design and Construction of a Parabolic Dish in Mexico. in: *Proceedings of ASME 2004 International Solar Energy Conference*, 2004, 653-657.
- [39] PAVLOVIĆ S R, STEFANOVIĆ V P, SULJKOVIĆ S H. OPTICAL MODELING OF A SOLAR DISH THERMAL CONCENTRATOR BASED ON SQUARE FLAT FACETS. *Thermal Science*, 2014, 18(3):989 – 998.
- [40] Hijazi H, Mokhiamar O, Elsamni O. Mechanical design of a low cost parabolic solar dish concentrator. *Alexandria Engineering Journal*, 2016, 55(1):1 – 11.
- [41] Ma H, Jin G, Xing Z, et al. Optical Design of a Solar Dish Concentrator Based on Triangular Membrane Facets. *International Journal of Photoenergy*, 2012, 2012(2012):3109–3109.
- [42] Schertz P T, Brown D C, Konnerth I. Facet development for a faceted stretched-membrane dish by Solar Kinetics, Inc. *Parabolic Dish Collectors*, 1991, 91.
- [43] Shuai Y, Xia X, Tan H. Numerical simulation and experiment research of radiation performance in a dish solar collector system. *Frontiers of Energy & Power Engineering in China*, 2010, 4(4):488–495.
- [44] Qianjun M, Ming X, Yong S, et al. Study on solar photo-thermal conversion efficiency of a solar parabolic dish system. *Environmental Progress & Sustainable Energy*, 2014, 33(4):1438–1444.
- [45] Li Z, Tang D, Du J, et al. Study on the radiation flux and temperature distributions of the concentrator–receiver system in a solar dish/Stirling power facility. *Applied Thermal Engineering*, 2011, 31(10):1780 – 1789.
- [46] Wang W, Laumert B. Effect of cavity surface material on the concentrated solar flux distribution for an impinging receiver. *Solar Energy Materials and Solar Cells*, 2017, 161(Supplement C):177 – 182.
- [47] Blázquez R, Carballo J, Silva M. Optical design and optimization of parabolic dish solar concentrator with a cavity hybrid receiver. *AIP Conference Proceedings*, 2016, 1734(1).
- [48] Reddy K, Vikram T S, Veershetty G. Combined heat loss analysis of solar parabolic dish – modified cavity receiver for superheated steam generation. *Solar Energy*, 2015, 121:78 – 93. {ISES} Solar World Congress 2013 (SWC2013) Special Issue.

- [49] Vikram T S, Reddy K. Investigation of convective and radiative heat losses from modified cavity based solar dish steam generator using {ANN}. *International Journal of Thermal Sciences*, 2015, 87:19 – 30.
- [50] Patil P N, Khandekar M A, Patil S N. Automatic dual-axis solar tracking system for parabolic dish. in: Proceedings of 2016 2nd International Conference on Advances in Electrical, Electronics, Information, Communication and Bio-Informatics (AEEICB), Feb, 2016, 699-703.
- [51] Raturi M P, Deolal M H, Grover J, et al. Parabolic Dish Type Solar Cooking System with Gravity Based Solar Tracking System. 2014, 11(3):34–36.
- [52] Kuang J, Zhang W. Design and Implementation of Tracking System for Dish Solar Thermal Energy Based on Embedded System. Berlin, Heidelberg: Springer Berlin Heidelberg, 2012, pages 31–38.
- [53] Jin X, Xu G, Zhou R, et al. A Sun Tracking System Design for a Large Dish Solar Concentrator. *International Journal of Clean Coal & Energy*, 2013, 02(2):16–20.
- [54] Shanmugam S, Chrstraj W. The Tracking of the Sun for Solar Paraboloidal Dish Concentrators. *Journal of Solar Energy Engineering*, 2005, 127(1):156–160.
- [55] Alexopoulos S, Hoffschmidt B. Advances in solar tower technology. *Wiley Interdisciplinary Reviews: Energy and Environment*, 2017, 6(1):e217–n/a. E217.
- [56] Montes M, Abánades A, Martínez-Val J. Performance of a direct steam generation solar thermal power plant for electricity production as a function of the solar multiple. *Solar Energy*, 2009, 83(5):679 – 689.
- [57] Feldhoff J F, Schmitz K, Eck M, et al. Comparative system analysis of direct steam generation and synthetic oil parabolic trough power plants with integrated thermal storage. *Solar Energy*, 2012, 86(1):520 – 530.
- [58] Steinmann W D, Eck M. Buffer storage for direct steam generation. *Solar Energy*, 2006, 80(10):1277 – 1282. Solar Power and Chemical Energy Systems (SolarPACES'04).
- [59] Yu Q, Wang Z, Zhu L. Analysis and improvement of the cavity structure of steam receiver of 1MWe solar tower power plant. in: Proceedings of Solarpaces: International Conference on Concentrating Solar Power & Chemical Energy Systems, 2017, 164-174.
- [60] González-Roubaud E, Pérez-Osorio D, Prieto C. Review of commercial thermal energy storage in concentrated solar power plants: Steam vs. molten salts. *Renewable and Sustainable Energy Reviews*, 2017, 80(Supplement C):133 – 148.
- [61] Toro C, Rocco M V, Colombo E. Exergy and Thermoeconomic Analyses of Central Receiver Concentrated Solar Plants Using Air as Heat Transfer Fluid. *Energies*, 2016, 9(11).
- [62] Roldán M I, Fernándezreche J. CFD analysis of supercritical CO₂ used as HTF in a solar tower receiver. in: Proceedings of Solarpaces: International Conference on Concentrating Solar Power & Chemical Energy Systems, 2016, 2293-2305.
- [63] Joshi A, Wang C, Akinjiola O, et al. Transient analysis of a molten salt central receiver (MSCR) in a solar power plant. 2016, 1734(1):578–592.
- [64] Thalange V C, Dalvi V H, Mahajani S M, et al. Design, optimization and optical performance study of tripod heliostat for solar power tower plant. *Energy*, 2017, 135(Supplement C):610 –

624.

- [65] Besarati S M, Yogi Goswami D. A computationally efficient method for the design of the heliostat field for solar power tower plant. *Renewable Energy*, 2014, 69:226–232.
- [66] Sassi G. Some notes on shadow and blockage effects. *Solar Energy*, 1983, 31(3):331 – 333.
- [67] Wei X, Lu Z, Wang Z, et al. A new method for the design of the heliostat field layout for solar tower power plant. *Renewable Energy*, 2010, 35(9):1970–1975.
- [68] Kim J, Kim J S, Stein W. Simplified heat loss model for central tower solar receiver. *Solar Energy*, 2015, 116:314 – 322.
- [69] Lara-Cerecedo L O, Moreno-Cruz I, Pitalúa-Díaz N, et al. Modeling of Drift Effects on Solar Tower Concentrated Flux Distributions. *International Journal of Photoenergy*, 2016, 2016:1–9.
- [70] Franchini G, Perdichizzi A, Ravelli S, et al. A comparative study between parabolic trough and solar tower technologies in Solar Rankine Cycle and Integrated Solar Combined Cycle plants. *Solar Energy*, 2013, 98, Part C:302 – 314.
- [71] Xu E, Yu Q, Wang Z, et al. Modeling and simulation of 1 MW DAHAN solar thermal power tower plant. *Renewable Energy*, 2011, 36(2):848–857.
- [72] Xu E, Wang Z, Wei G, et al. Dynamic simulation of thermal energy storage system of Badaling 1 MW solar power tower plant. *Renewable Energy*, 2012, 39(1):455–462.
- [73] Benammar S, Khellaf A, Mohammedi K. Contribution to the modeling and simulation of solar power tower plants using energy analysis. *Energy Conversion and Management*, 2014, 78(Supplement C):923 – 930.
- [74] Suzuki A. Cascade connection of solar collectors for effective energy gain. *Journal of Solar Energy Engineering Transactions of the Asme*, 1986, 108(3):172–177.
- [75] Kribus A, Doron P, Rubin R, et al. A Multistage Solar Receiver:: The Route To High Temperature. *Solar Energy*, 1999, 67(1–3):3 – 11.
- [76] Gordon J M, Saltiel C. Analysis and Optimization of a Multi-Stage Solar Collector System. *Journal of Solar Energy Engineering*, 1986, 108(3):192–198.
- [77] Oshida I, Suzuki A. Optical Cascade Heat-Collection for Effective Solar Energy Gain. *Journal of Solar Energy Engineering*, 1987, 109(4):298–302.
- [78] Desai N B, Bandyopadhyay S. Integration of parabolic trough and linear Fresnel collectors for optimum design of concentrating solar thermal power plant. *Clean Technologies and Environmental Policy*, 2015, 17(7):1945–1961.
- [79] Coco-Enríquez L, Muñoz-Antón J, Martínez-Val J. Integration between direct steam generation in linear solar collectors and supercritical carbon dioxide Brayton power cycles. *International Journal of Hydrogen Energy*, 2015, 40(44):15284 – 15300. The 4th International Conference on Nuclear and Renewable Energy Resources (NURER2014), 26-29 October 2014, Antalya, Turkey.
- [80] Li Y, Yang Y. Thermodynamic analysis of a novel integrated solar combined cycle. *Applied Energy*, 2014, 122:133 – 142.
- [81] Gülen S C. Second Law Analysis of Integrated Solar Combined Cycle Power Plants. *Journal*

of Engineering for Gas Turbines and Power, 2015, 137(5):51701.

- [82] Shaaban S. Analysis of an integrated solar combined cycle with steam and organic Rankine cycles as bottoming cycles. *Energy Conversion and Management*, 2016, 126:1003–1012.
- [83] Alqahtani B J, Patiño-Echeverri D. Integrated Solar Combined Cycle Power Plants: Paving the way for thermal solar. *Applied Energy*, 2016, 169:927 – 936.
- [84] Manente G. High performance integrated solar combined cycles with minimum modifications to the combined cycle power plant design. *Energy Conversion and Management*, 2016, 111:186 – 197.
- [85] Turchi C S, Ma Z. Co-located gas turbine/solar thermal hybrid designs for power production. *Renewable Energy*, 2014, 64:172 – 179.
- [86] Mukhopadhyay S, Ghosh S. Solar tower combined cycle plant with thermal storage: energy and exergy analyses. *Advances in Energy Research*, 2016, 4(1):29–45.
- [87] Li J, Li P, Pei G, et al. Analysis of a novel solar electricity generation system using cascade Rankine cycle and steam screw expander. *Applied Energy*, 2016, 165:627–638.
- [88] Al-Sulaiman F A. Exergy analysis of parabolic trough solar collectors integrated with combined steam and organic Rankine cycles. *Energy Conversion and Management*, 2014, 77:441 – 449.
- [89] Dunham M T, Lipiński W. Thermodynamic Analyses of Single Brayton and Combined Brayton–Rankine Cycles for Distributed Solar Thermal Power Generation. *Journal of Solar Energy Engineering*, 2013, 135(3):031008–031008–8.
- [90] Bahrami M, Hamidi A A, Porkhial S. Investigation of the effect of organic working fluids on thermodynamic performance of combined cycle Stirling-ORC. *International Journal of Energy and Environmental Engineering*, 2013, 4(1):12.
- [91] Thierry D M, Flores-Tlacuahuac A, Grossmann I E. Simultaneous optimal design of multi-stage organic Rankine cycles and working fluid mixtures for low-temperature heat sources. *Computers & Chemical Engineering*, 2016, 89:106 – 126.
- [92] Bahari S S, Sameti M, Ahmadi M H, et al. Optimisation of a combined Stirling cycle–organic Rankine cycle using a genetic algorithm. *International Journal of Ambient Energy*, 2016, 37(4):398–402.
- [93] Abbin J, Leuenberger W. Program CYCLE: a Rankine cycle analysis routine. [For solar–thermal electricity production for Sandia’s Solar Community study]. Oct, 1977.
- [94] Montes M, Rovira A, Muñoz M, et al. Performance analysis of an Integrated Solar Combined Cycle using Direct Steam Generation in parabolic trough collectors. *Applied Energy*, 2011, 88(9):3228 – 3238.
- [95] Elsafi A M. Exergy and exergoeconomic analysis of sustainable direct steam generation solar power plants. *Energy Conversion and Management*, 2015, 103(Supplement C):338 – 347.
- [96] Fraidenraich N, Oliveira C, Cunha A F V, et al. Analytical modeling of direct steam generation solar power plants. *Solar Energy*, 2013, 98(Part C):511 – 522.
- [97] Roschke E J, Wen L, Steele H, et al. A preliminary assessment of small steam Rankine and Brayton point-focusing solar modules. *Nasa Sti/recon Technical Report N*, 1979, 79.

- [98] Bao J, Zhao L. A review of working fluid and expander selections for organic Rankine cycle. *Renewable and Sustainable Energy Reviews*, 2013, 24:325 – 342.
- [99] Bilgen E, Rheault J. Solar chimney power plants for high latitudes. *Solar Energy*, 2005, 79(5):449 – 458.
- [100] Good P, Ambrosetti G, Pedretti A, et al. A 1.2MWth solar parabolic trough system based on air as heat transfer fluid at 500 °C — Engineering design, modelling, construction, and testing. *Solar Energy*, 2016, 139(Supplement C):398 – 411.
- [101] Fernández-García A, Zarza E, Valenzuela L, et al. Parabolic-trough solar collectors and their applications. *Renewable and Sustainable Energy Reviews*, 2010, 14(7):1695 – 1721.
- [102] Giglio A, Lanzini A, Leone P, et al. Direct steam generation in parabolic-trough collectors: A review about the technology and a thermo-economic analysis of a hybrid system. *Renewable and Sustainable Energy Reviews*, 2017, 74:453–473.
- [103] Khenissi A, Krüger D, Hirsch T, et al. Return of Experience on Transient Behavior at the DSG Solar Thermal Power Plant in Kanchanaburi, Thailand. *Energy Procedia*, 2015, 69:1603 – 1612. International Conference on Concentrating Solar Power and Chemical Energy Systems, SolarPACES 2014.
- [104] Romero-Alvarez M, Zarza E. Concentrating solar thermal power. *Efficiency and Renewable Energy*, 2007.
- [105] Adkins D R. Control strategies and hardware used in solar thermal applications. Nasa Sti/recon Technical Report N, 1987, 88.
- [106] Coronel P, Sandeep K. Heat transfer coefficient in helical heat exchangers under turbulent flow conditions. *International Journal of Food Engineering*, 2008, 4(1).
- [107] Serth R W. *Process heat transfer principles and applications*. Amsterdam; London: Elsevier Academic Press, 2007.
- [108] Churchill S W, Bernstein M. A Correlating Equation for Forced Convection From Gases and Liquids to a Circular Cylinder in Crossflow. *Journal of Heat Transfer*, 1977, 99(2):300–306.
- [109] Ma R Y. Wind Effects on Convective Heat Loss From a Cavity Receiver for a Parabolic Concentrating Solar Collector. Sandia National Laboratory, 1993, SAND92-7293(September).
- [110] Wu S Y, Xiao L, Cao Y, et al. Convection heat loss from cavity receiver in parabolic dish solar thermal power system: A review. *Solar Energy*, 2010, 84(8):1342 – 1355.
- [111] Leibfried U, Ortjohann J. Convective Heat Loss from Upward and Downward-Facing Cavity Solar Receivers: Measurements and Calculations. *Journal of Solar Energy Engineering*, 1995, 117(2):75–84.
- [112] Koenig A, Marvin M. Convection heat loss sensitivity in open cavity solar receivers. Technical report, Department of Energy, USA, 1981.
- [113] Stine W B, Diver R B. A compendium of solar dish/Stirling technology. Technical report, DTIC Document, 1994.
- [114] Formosa F, Despesse G. Analytical model for Stirling cycle machine design. *Energy Conversion and Management*, 2010, 51(10):1855–1863.

- [115] Juhasz A. A mass computation model for lightweight brayton cycle regenerator heat exchangers. in: Proceedings of 8th Annual International Energy Conversion Engineering Conference, 2010.
- [116] Duan C, Wang X, Shu S, et al. Thermodynamic design of Stirling engine using multi-objective particle swarm optimization algorithm. *Energy Conversion & Management*, 2014, 84:88–96.
- [117] Urieli I, Berchowitz D M. Stirling cycle engine analysis. Bristol: A. Hilger, 1984.
- [118] Heywood, JohnB. Internal combustion engine fundamentals. Amsterdam; London: McGraw-Hill, 1988.
- [119] Strauss J M, Dobson R T. Evaluation of a second order simulation for Sterling engine design and optimisation. *Journal of Energy in Southern Africa*, 2010, 21(2):17–29.
- [120] Timoumi Y, Tlili I, Nasrallah S B. Design and performance optimization of GPU-3 Stirling engines. *Energy*, 2008, 33(7):1100 – 1114.
- [121] Hosseinzade H, Sayyaadi H, Babaelahi M. A new closed-form analytical thermal model for simulating Stirling engines based on polytropic-finite speed thermodynamics. *Energy Conversion and Management*, 2015, 90:395 – 408.
- [122] Der Minassians A. Stirling Engines for Low-temperature Solar-thermal-electric Power Generation: [PhD Dissertation]. Berkeley: EECS Department, University of California, Berkeley, December 20, 2007.
- [123] Cavazzuti M. Optimization Methods: From Theory to Design Scientific and Technological Aspects in Mechanics. Berlin Heidelberg: Springer, 2012.
- [124] Hooshang M, Moghadam R A, AlizadehNia S. Dynamic response simulation and experiment for gamma-type Stirling engine. *Renewable Energy*, 2016, 86:192 – 205.
- [125] Fraser P, Klein P S a. Stirling Dish System Performance Prediction Model. *Mechanical Engineering*, 2008, Master of:203.

附录 A Heat transfer under constant temperature

Assuming U, T_c, \dot{m}, c_p to be constant, for given T_i ,

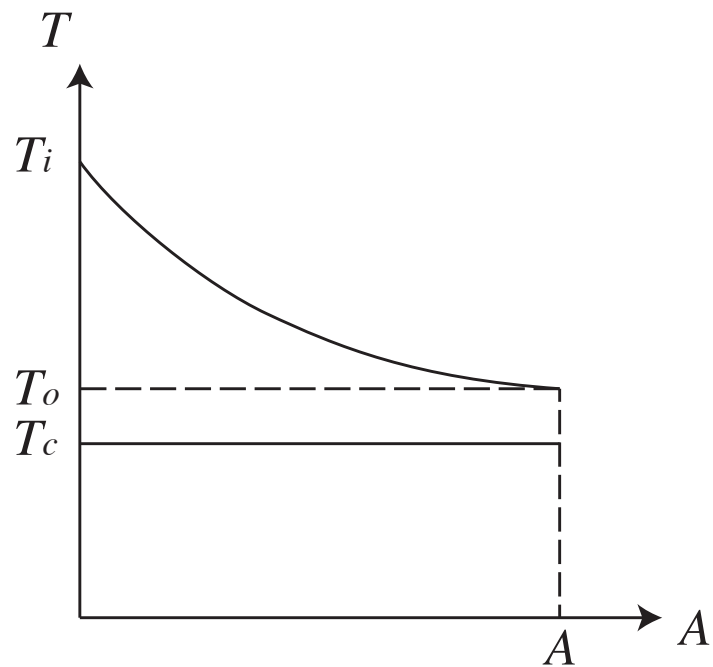


图 1-1 Diagram of heat transfer under constant temperature

For $A(x) = Px$, x from 0 to L , while $T(x)$ from T_i to T_o ,

$$\dot{m}c_p dT(x) = (T_c - T(x))UPdx \quad (\text{A.1})$$

so

$$\frac{dT(x)}{dx} = -\frac{UP}{\dot{m}c_p}(T(x) - T_c) \quad (\text{A.2})$$

$$T_g(x) = T_p(x) + T_h(x) \quad (\text{A.3})$$

where $T_g(x)$ is the general solution, $T_p(x)$ is the particular solution, $T_h(x)$ is the homogeneous solution.

$$-\frac{UP}{\dot{m}c_p}(T_p(x) - T_c) = 0 \quad (\text{A.4})$$

$$T_p(x) = T_c \quad (\text{A.5})$$

$$\frac{dT_h(x)}{dx} = -\frac{UP}{\dot{m}c_p}T_h(x) \quad (\text{A.6})$$

$$\int_{T_h(x)=T_h(0)}^{T_h(x)=T_h(L)} \frac{dT_h(x)}{T_h(x)} = - \int_{x=0}^{x=L} \frac{UP}{\dot{m}c_p} dx \quad (\text{A.7})$$

$$\frac{T_h(L)}{T_h(0)} = \exp\left(-\frac{UPL}{\dot{m}c_p}\right) \quad (\text{A.8})$$

that is

$$\frac{T_g(L) - T_p(L)}{T_g(0) - T_p(0)} = \exp\left(-\frac{UA}{\dot{m}c_p}\right) \quad (\text{A.9})$$

$$\frac{T_o - T_c}{T_i - T_c} = \exp\left(-\frac{UA}{\dot{m}c_p}\right) \quad (\text{A.10})$$

附录 B Thermal gradient under constant heat flux

Assuming $U, T_c, \dot{m}, c_p, q''$ to be constant, for given T_i ,

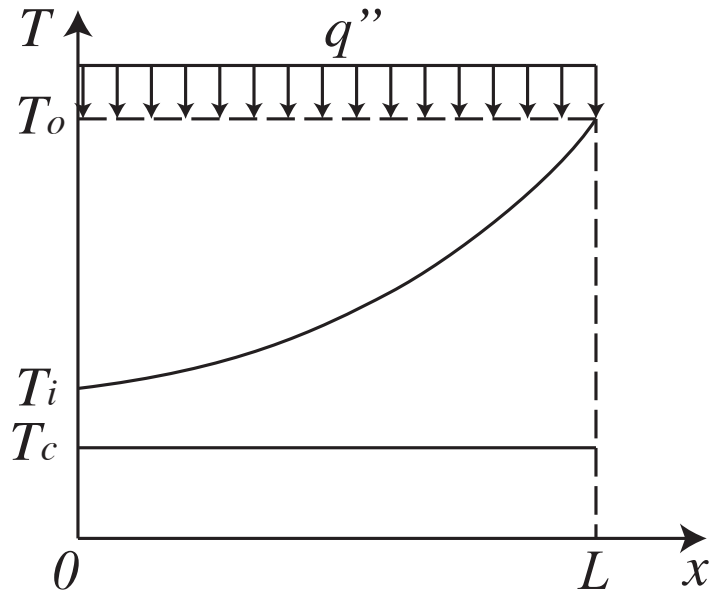


图 2-1 Diagram of heat transfer with one constant temperature heat source and constant heat flux

For $A(x) = Px$, x from 0 to L , while $T(x)$ from T_i to T_o ,

$$\dot{m}c_p dT(x) = (T_c - T(x))UPdx + q''Pdx \quad (\text{B.1})$$

so

$$\frac{dT(x)}{dx} = -\frac{UP}{\dot{m}c_p}T(x) + \frac{q''P + UPT_c}{\dot{m}c_p} \quad (\text{B.2})$$

$$T_g(x) = T_p(x) + T_h(x) \quad (\text{B.3})$$

where $T_g(x)$ is the general solution, $T_p(x)$ is the particular solution, $T_h(x)$ is the homogeneous solution.

$$-\frac{UP}{\dot{m}c_p}T_p(x) + \frac{q''P + UPT_c}{\dot{m}c_p} = 0 \quad (\text{B.4})$$

$$T_p(x) = T_c + \frac{q''}{U} \quad (\text{B.5})$$

$$\frac{dT_h(x)}{dx} = -\frac{UP}{\dot{m}c_p}T_h(x) \quad (\text{B.6})$$

the same as Equation (A.6), so we have

$$\frac{T_g(L) - T_p(L)}{T_g(0) - T_p(0)} = \exp\left(-\frac{UA}{\dot{m}c_p}\right) \quad (\text{B.7})$$

$$\frac{\frac{T_o - T_c - \frac{q''}{U}}{T_i - T_c - \frac{q''}{U}}}{\frac{q''}{U}} = \exp\left(-\frac{UA}{\dot{m}c_p}\right) \quad (\text{B.8})$$

附录C MATLAB code of class Stream

```
1 classdef Stream < handle
2     %Stream This class describes a fluid stream that has inherent
3     %properties and dependent properties
4
5     properties
6         fluid;    % Fluid type
7         dot_m;   % Mass flow rate, kg/s
8         T;       % Temperature, K
9         p;       % Pressure, Pa
10        x;       % Quality, [0, 1] for two phase stream; NaN for single
11        % phase stream
12    end
13    properties(Dependent)
14        h;        % Mass specific enthalpy, J.kg
15        s;        % Mass specific entropy, J/kg-K
16        cp;      % Specific heat under constant pressure, J/kg-K
17    end
18
19    methods
20        function obj = Stream
21            obj.T = Temperature;
22            obj.dot_m = Massflow;
23            obj.p = Pressure;
24        end
25        function flowTo(obj, st)
26            st.fluid = obj.fluid;
27            st.dot_m = obj.dot_m;
28        end
29        function st2 = mix(obj, st1)
30            % Get the properties of a stream mixed by two streams
31            % The two streams must have the same fluid type and pressure
32            if obj.fluid == st1.fluid
33                if obj.p.v == st1.p.v
34                    obj.p = st1.p;
35                    st2.fluid = obj.fluid;
36                    st2.p = obj.p;
37                    st2.dot_m.v = obj.dot_m.v + st1.dot_m.v;
38                    h = (obj.dot_m.v .* obj.h + st1.dot_m.v .* st1.h)...
39                        ./ (obj.dot_m.v + st1.dot_m.v);
40                    st2.T.v = CoolProp.PropsSI('T', 'H', h, 'P', st2.p.v);
41                else
42                    error('The two streams have different pressures!');
43                end
44            else
```

```

45         error('The two streams have different fluid types!');
46     end
47 end
48 function convergeTo(obj, st, y)
49 % Get another stream converged (or diverged)
50 % from the original stream state.
51 % If y < 1, the original stream is diverged
52 % If y > 1, the original stream is converged
53 st.fluid = obj.fluid;
54 st.T = obj.T;
55 st.p = obj.p;
56 st.x = obj.x;
57 st.dot_m.v = obj.dot_m.v .* y;
58 end
59 end
60 methods
61 % The dependent properties can be obtained from the inherent
62 % properties
63 % If x is NaN, then the dependent properties are determined
64 % by T and P; otherwise, they are determined by P and x
65 function value = get.h(obj)
66 if isempty(obj.x)
67     value = CoolProp.PropsSI('H', 'T', obj.T.v, ...
68                             'P', obj.p.v, obj.fluid);
69 else
70     value = CoolProp.PropsSI('H', 'P', obj.p.v, 'Q', ...
71                             obj.x, obj.fluid);
72 end
73 end
74 function value = get.s(obj)
75 if isempty(obj.x)
76     value = CoolProp.PropsSI('S', 'T', obj.T.v, ...
77                             'P', obj.p.v, obj.fluid);
78 else
79     value = CoolProp.PropsSI('S', 'P', obj.p.v, 'Q', ...
80                             obj.x, obj.fluid);
81 end
82 end
83 function value = get.cp(obj)
84 if isempty(obj.x)
85     value = CoolProp.PropsSI('C', 'T', obj.T.v, ...
86                             'P', obj.p.v, obj.fluid);
87 else
88     value = inf;
89 end
90 end
91 end
92 end

```

附录D 攻读学位期间发表的学术论文

- [1] Cheng Zhang, Yanping Zhang, Inmaculada Arauzo, Wei Gao, Chongzhe Zou. Cascade system using both trough system and dish system for power generation. *Energy Conversion and Management*. 2017.06.15;142:494–503.
- [2] Cheng Zhang, Yanping Zhang, Xiaolin Lei, Wei Gao. Design and Comparison of Solar Thermal Oilfield Steam Production System Plans. *Journal of Solar Energy Engineering*. 2017.01.08;139;004502-4.
- [3] Cheng Zhang, Kun Wang, Jizhou Wang, Shuhong Huang. FEA simulation on the alignment of the shafts of three-fulcrum turbine. *International Conference on Power Engineering*. 2013.
- [4] Chongzhe Zou, Yanping Zhang, Quentin Falcoz, Pierre Neveu, Cheng Zhang, Shuhong Huang, Weicheng Shu. Design and Optimization of a High-temperature Cavity Receiver for a Solar Energy Cascade Utilization System. *Renewable Energy*. 2017.04.01:103; 478-89.
- [5] Chongzhe Zou, Yanping Zhang, Huayi Feng, Quentin Falcoz, Pierre Neveu, Cheng Zhang, Wei Gao. “Effects of Geometrical Parameters on Thermal Performance for a Cylindrical Solar Receiver Using 3D numerical Model.” *Energy Conversion and Management*, 2017.10.1: 126-17.
- [6] Chongzhe Zou, Yanping Zhang, Quentin Falcoz, Pierre Neveu, Cheng Zhang. Thermal modeling of a pressurized air cavity receiver for solar dish Stirling system, *Solarpaces: International Conference on Concentrating Solar Power & Chemical Energy Systems*. AIP Publishing LLC, 2017:1884-1892.
- [7] A solar thermal cascade system, No. 201610806296.5
- [8] A flow control method used in a multistage heating system, No. 201610805604.2